

The AGN contribution to the UV-FIR luminosities of interacting galaxies and its role in identifying the Main Sequence

Andrés F. Ramos P.,^{1,2,3*} M. L. N. Ashby³, Howard A. Smith³, Juan R. Martínez-Galarza³, Aliza G. Beverage^{3,4}, Jeremy Dietrich^{3,5}, Mario-A. Higuera-G.⁶, and Aaron S. Weiner³

¹*Kapteyn Astronomical Institute, University of Groningen, Landleven 12, 9747 AD Groningen, The Netherlands*

²*SRON Netherlands Institute for Space Research, Landleven 12, 9747 AD Groningen, The Netherlands*

³*Center for Astrophysics | Harvard & Smithsonian, 60 Garden Street, Cambridge, MA 02138, USA*

⁴*Astronomy Department, University of California, Berkeley, CA 94720, USA*

⁵*Department of Astronomy and Steward Observatory, University of Arizona, 933 N Cherry Ave, Tucson, AZ 85719, USA*

⁶*Observatorio Astronómico Nacional, Universidad Nacional de Colombia, Carrera 45 No 26-85, Bogotá D.C., Colombia*

Accepted 2020 September 11. Received 2020 September 4; in original form 2020 April 17

ABSTRACT

Emission from active galactic nuclei (AGNs) is known to play an important role in the evolution of many galaxies including luminous and ultraluminous systems (U/LIRGs), as well as merging systems. However, the extent, duration, and exact effects of its influence are still imperfectly understood. To assess the impact of AGNs on interacting systems, we present a Spectral Energy Distribution (SED) analysis of a sample of 189 nearby galaxies. We gather and systematically re-reduce archival broad-band imaging mosaics from the ultraviolet to the far-infrared using data from *GALEX*, SDSS, 2MASS, *IRAS*, *WISE*, *Spitzer* and *Herschel*. We use spectroscopy from *Spitzer*/IRS to obtain fluxes from fine-structure lines that trace star formation and AGN activity. Utilizing the SED modelling and fitting tool CIGALE, we derive the physical conditions of the ISM, both in star-forming regions and in nuclear regions dominated by the AGN in these galaxies. We investigate how the star formation rates (SFRs) and the fractional AGN contributions (f_{AGN}) depend on stellar mass, galaxy type, and merger stage. We find that luminous galaxies more massive than about $10^{10}M_{\odot}$ are likely to deviate significantly from the conventional galaxy main-sequence relation. Interestingly, infrared AGN luminosity and stellar mass in this set of objects are much tighter than SFR and stellar mass. We find that buried AGNs may occupy a locus between bright starbursts and pure AGNs in the $f_{\text{AGN}}\text{--[Ne v]}/\text{[Ne II]}$ plane. We identify a modest correlation between f_{AGN} and mergers in their later stages.

Key words: Galaxies: active, evolution, interactions, starburst; Techniques: photometric, spectroscopic

1 INTRODUCTION

Over the past decade, a significant body of evidence has accumulated that supports the existence of a so-called main sequence (MS) of star-forming galaxies (e.g. Elbaz et al. 2011; Speagle et al. 2014), a tight correlation between galaxy stellar mass and the star formation rate (SFR). This scaling relation is claimed to be independent of redshift and luminosity (Elbaz et al. 2011), but its normalisation does evolve with redshift (Speagle et al. 2014). Outliers above the MS are often interpreted as merger-driven starbursts with enhanced SFRs (Renzini & Peng 2015; Martínez-Galarza et al. 2016; Pearson et al. 2019). The relatively tight correlation suggests that the

bulk of the stars in star-forming galaxies form via secular processes rather than in violent events, such as mergers (Ciesla et al. 2015, and references therein). However, this correlation depends in part on the assumptions used to calculate SFRs, star formation histories (SFHs), halo properties, and the degree to which galaxy interactions enhance star formation (e.g. Hayward et al. 2014; Matthee & Schaye 2019).

Interacting systems are therefore crucial to our understanding of galaxy assembly over cosmic time, and of the mechanisms that shape the observed scaling relations. In the local Universe, the most luminous infrared galaxies are almost exclusively systems undergoing significant mergers (Stierwalt et al. 2013). In these systems, star formation is significantly enhanced by the funnelling of gas and dust into the nuclear region, and the thermal emission from obscured

* ramos@astro.rug.nl (AFRP)

star-forming regions outshines the UV and optical radiation from massive young stars. Systems with luminosities greater than $10^{11} L_{\odot}$ (so-called Luminous InfraRed Galaxies, or LIRGs) are typically found in interacting systems, which results in a strong correlation between enhanced SFR and galaxy interaction (Sanders & Mirabel 1996; Su et al. 2013). However, this simple description does not capture the full range of observed behaviour. For example, Lanz et al. (2013) found no correlation between specific star formation rate (sSFR) and galaxy mergers (see also Silva et al. 2018).

Nuclear starbursts may exist in galaxies that are not undergoing a merger, with about 20% of all spiral galaxies displaying starburst activity in nuclear rings (Brandl et al. 2012). In many of these systems, the active galactic nucleus (AGN) contribution to the luminosity from activity around the supermassive black hole appears to be negligible. These *pure* starbursts are the opposite extreme of systems that are almost entirely dominated by the infrared emission from a dusty torus surrounding an AGN, such as Seyfert galaxies and more distant quasars. To put those two extremes in context, a thorough understanding of the energetics of systems with intermediate AGN contributions is needed. Although star formation dominates the bolometric luminosity of nearby systems during most of the merger, during the later stages an AGN is thought to become active (Sanders & Mirabel 1996; Brassington et al. 2015, and references therein). Presumably, AGNs are fed by the same infalling material that feeds star formation, and the mid-infrared thermal emission from the dusty torus around AGNs can be comparable to that of the dusty star-forming regions (Genzel et al. 1998).

There exists strong theoretical evidence from simulations of mergers (Lanz et al. 2014; Hayward et al. 2014; Dietrich et al. 2018) that AGNs dominate bolometric luminosity during coalescence, and are responsible for quenching star formation in the post-coalescence stages (Dixon & Joseph 2011). This process underlies their transition from the star-forming “blue cloud”, through the so-called “green valley”, and onto the passively evolving “red sequence” (Ciesla et al. 2015). There is widespread support of this evolutionary path moving from star-forming galaxies to AGN-dominated galaxies (see Sturm et al. 2002; Veilleux et al. 2009; Tommasin et al. 2010; Wu et al. 2011, and references therein), and it is also supported by simulations showing that AGN activity is strongly correlated with the merger stage (Hopkins et al. 2006). Merging galaxies at different interaction stages, ranging from first encounter to post-coalescence, are a natural choice to study AGN evolution and star formation of composite galaxies that combine both starburst and AGN processes.

Uncertainties regarding the energy budget in composite starburst-AGN systems, and about how the two energy generation processes impact one another and evolve, are among the most pressing open questions in astrophysics. For example, buried AGN have been discovered in systems previously catalogued as pure starbursts (e.g. Higuera-G et al. 2009; Dixon & Joseph 2011), and physical models have been proposed to describe the interplay between the two (Ishibashi & Fabian 2016). Discriminating between the two processes based on spectral energy distribution (SED) studies is relatively straightforward and reliable when just one dominates the emission, especially at mid-IR wavelengths. Unfortunately, disentangling them becomes much more difficult when their IR luminosities are comparable (Abel & Satyapal 2008). Optical and infrared spectroscopy can potentially separate the two if they cover specific fine-structure lines which are prominent in the vicinity of AGNs and weak or non-existing in star forming regions. The best-known example is the BPT diagram (Genzel et al. 1998; Fritz et al. 2006) which separates AGNs from starbursts according to their $[O III] \lambda 5007/H\beta$ and $[N II] \lambda 6584/H\alpha$ line intensity ratios, among others.

The BPT diagrams are not always reliable, however, because high dust opacities toward AGNs can significantly attenuate emission lines at optical wavelengths. For this reason, the absolute strengths of specific mid-infrared emission lines have also been used to estimate AGN contributions (e.g. Genzel et al. 1998). Others have used the silicate attenuation in the SED, or other SED features (Groves et al. 2008; Ciesla et al. 2015). But these techniques, however useful for signaling the presence of AGNs, aren’t capable of straightforwardly disentangling the relative importance of star formation and AGNs in composite systems.

To understand the physical mechanisms underlying scaling relations such as the MS, it is of crucial importance to account for the AGN contribution to the total luminosity of merging systems and estimate the SFRs and sSFRs at different interaction stages. The picture at present is somewhat confused. For example, Lanz et al. (2013) and Silva et al. (2018) find no significant change in sSFR with interaction stage, but Lanz et al. (2014) do find that sSFR increases during the relatively short times around nuclear coalescence because the SFR increases but the total mass of stars do not change. Furthermore, combining simulations and multi-wavelength observations, Martínez-Galarza et al. (2016) find that the SEDs of interacting galaxies do change with interaction stage, due to changes in stellar mass and SFR, and that these changes affect the location of galaxies within the MS.

Using SED modeling, Ciesla et al. (2015) showed that the AGN emission could modify the MS slope. Overestimations of the SFR due to the presence of a buried AGN are plausible especially at later stages, and the AGN emission can contribute to the observed MS scatter. Ciesla et al. (2015) verified that these effects can be reduced through broadband SED fitting methods such as CIGALE (Burgarella et al. 2005; Noll et al. 2009; Serra et al. 2011) by taking into account the continuum emission from the AGN to obtain a better interpretation of the star-forming galaxies.

In this work, we apply those SED modeling techniques to four galaxy samples, estimate the fractional contributions of AGNs to their output, and elucidate how that depends on interaction stage. Our approach includes photometry from the UV to the far-infrared to account for multiple emission processes that blend with the AGN emission: UV emission from young stars, optical and near-infrared stellar photospheric emission, mid-infrared emission from warm dust heated by star formation and evolved AGB stars, and cold dust emission. We incorporate photometry from dozens of instruments and surveys.

This paper is organized as follows. In Sec. 2, we present the sample selection and in Sec. 3 describe the data reduction. Section 4 describes how we use CIGALE to analyse our photometric data and the MIR emission lines. We present the derived galaxy parameters in Sec. 5 and discuss their implications in Sec. 6. We present our conclusions in Sec. 7. Our photometry and spectroscopy, as well as the derived parameters for all the galaxies, are presented in the Appendix (available online). Throughout this paper we adopt $H_0 = 67.7 \text{ km s}^{-1} \text{ Mpc}^{-1}$ (Planck Collaboration et al. 2016).

2 THE FOUR STUDY SAMPLES

AGN activity ranges from nonexistent to dominant in any particular galaxy. During a galaxy merger, AGN activity can increase over time, so that immediately after coalescence, it is – at least briefly – the dominant contributor to the luminosity (Narayanan et al. 2010; Blecha et al. 2018). Star formation activity is also influenced by mergers, reaching high star-formation intensity in many

well-known cases (Veilleux et al. 2009; Stierwalt et al. 2013, among others). But not all AGNs arise in mergers, and not all starburst galaxies host detectable AGNs. Here our approach is to address this ambiguity in a statistical sense by comparing samples of galaxies selected in different ways. Specifically, we attempt to understand how galaxy interactions influence AGN activity by analyzing systems that span wide ranges of 1) interaction stage, from isolated galaxies to coalescing systems, and 2) activity, from AGN-dominated to star-formation-dominated.

We analyze four galaxy samples in the present work. First, we consider a sample of nearby systems selected to span a wide range of interaction stages from isolated systems to strongly interacting systems, the Spitzer Interacting Galaxies Sample (SIGS, Brassington et al. 2015, hereafter B15). Our work in 100 SIGS galaxies (see Sec. 2.1) builds on Lanz et al. (2013, 2014) and B15, but is based on a more complete sample, and includes spectroscopic diagnostics. The second sample is selected on the basis of *Spitzer*/IRS emission line ratios to be dominated by star formation (the SB sample, 21 galaxies; Sec. 2.2). The third sample is comprised of 29 AGN-dominated galaxies drawn broadly from the literature (Sec. 2.3). Finally, the fourth sample is a set of 49 late-stage merging systems chosen to be in or approaching final coalescence (the Late-Stage Merger or LSM sample; Sec. 2.4). We include the LSM galaxies specifically to address a gap in SIGS, which lacks late-stage mergers.

Thus our work includes not only systems with *a priori* known dominant activity (AGN or star formation) selected without regard to interaction stage, but also systems with *a priori* known interaction stage selected without regard to activity. We add that none of the galaxies in our four samples are radio-loud based on the identification criteria of Yun et al. (2001) that $L_{1.4\text{GHz}} \geq 10^{25} \text{ W Hz}^{-1}$. A summary of the four samples is presented in Table 1 and are described in detail below.

2.1 The Spitzer Interacting Galaxies Sample

Our first sample is drawn from SIGS (B15, see Table A1). The SIGS galaxies are relatively bright, nearby systems compiled by Keel et al. (1985) in a manner designed to construct a sample free from morphological bias. Specifically, Keel et al. (1985) identified systems containing a spiral galaxy with a companion seen in close projection, subject to area and magnitude restrictions. These systems comprise the so-called ‘‘Complete sample’’. To augment the Complete sample with more strongly interacting systems, Keel et al. (1985) also compiled a sample of close pairs with pronounced morphological signs of interaction (i.e., tidal tails and asymmetries). This second sample is known as the ‘‘Arp sample.’’ The basic properties of all SIGS galaxies are given in Table A1, in which the Complete and Arp galaxies are indicated with C and A, respectively. We adopted the distances given in B15 for all SIGS galaxies.

The SIGS galaxies’ merger stages were classified by B15, who assigned a numerical interaction strength to each system following Dopita et al. (2002). The classification is based on the degree of morphological disturbance, as follows.

- Stage 1 galaxies are isolated systems without discernible companions and are therefore, by construction, not present in SIGS.
- Stage 2 galaxies are weakly interacting systems, inferred on the basis of their very mild or absent morphological distortions.
- Stage 3 galaxies are moderately interacting, have apparent tidal features, and display moderate morphological distortions.
- Stage 4 galaxies are strongly interacting, with prominent tidal features, but have two separate nuclei that can still be resolved.

- Stage 5 mergers are at the point of coalescence or are merger remnants, and have only one apparent nucleus (the progenitor nuclei cannot be distinguished).

As described in B15, the stage of each system was put to the vote among the authors of that paper, using Digital Sky Survey (DSS) images, and the stage receiving the most votes for each system was assigned. The merger stages classified by B15 are noted in column ‘‘Interaction Stage’’ of Table A1. Ultimately, the original SIGS sample was found to consist of 35 Stage 2 galaxies, 34 Stage 3 galaxies, 33 Stage 4 galaxies, and just 1 Stage 5 galaxy. The SIGS objects treated here are predominantly early-to-intermediate mergers, with just a few late-stage mergers. Thus SIGS is most useful as a means of quantifying AGN activity in mergers *before coalescence*.

SIGS groups 40 and 41 (galaxy pairs NGC 5544/NGC 5545 and NGC 5614/NGC 5615, respectively) overlap too closely to be reliably photometered separately in the *Herschel*/PACS and SPIRE bands. We therefore photometered and subsequently modeled these systems as if they were single objects. NGC 5846 and NGC 5846A from SIGS group 42 were similarly entangled, and we treated them the same way, although we photometered and modeled the other group 42 galaxy, NGC 5850, separately. Thus the apertures given in Table A1 for NGC 5544, NGC 5614, and NGC 5846 encompass merging pairs instead of individual galaxies. Taking these considerations into account, the SIGS sample is effectively comprised of 100 galaxies.

2.2 The Starburst Sample

Our second study sample consists of galaxies dominated by star formation. This sample, which we refer throughout this work as the SB sample, consists of 21 relatively bright, nearby galaxies known from existing high-quality *Spitzer*/IRS (Houck et al. 2004) spectra taken in Short-High (SH) mode to be dominated by star formation. This requirement for IRS spectra was imposed to facilitate interpretation of the energetics and support the modeling effort, as diagnostic lines of the energetics (e.g. [Ne v] or [Ne II]) fall in the SH bandpass.

The SB sample is a heterogeneous group comprised of two subsamples. First, it includes 16 *Spitzer*-selected ‘‘classical’’ starburst galaxies from Brandl et al. (2006), selected from its enhanced nuclear star-formation. To these objects we added a selection of bright well-known starburst galaxies also having SH IRS spectra, some of them also form Brandl et al. (2006), including NGC 23, NGC 253, NGC 660, NGC 1797, NGC 3256, NGC 4088, and NGC 4945. A few of the galaxies do have weak AGN signatures as, for example, NGC 253 is known to host a weak AGN (Müller-Sánchez et al. 2010; Higuera-G. & Ramos P. 2013). In addition, the following systems are reported to be undergoing interactions: NGC 660, NGC 1222, NGC 1614, NGC 2623 (see Sect. 2.4), NGC 4194, NGC 4676, and NGC 7252. By using this heterogeneous SB sample, we can compare the other samples and check evolutionary connections between them, from the different levels of intensity of star-formation and AGN (Sturm et al. 2002; Veilleux et al. 2009; Tommasin et al. 2010; Wu et al. 2011).

For the SB sample (as well as for the AGN and LSM samples described in detail below), we adopted the redshifts given in NED.

2.3 The AGN Sample

Our third sample consisted of 29 strongly AGN-dominated galaxies. We created our AGN sample by selecting galaxies with both strong

Table 1. Basic data for the four study samples.

Sample	# Galaxies	References	Description
SIGS	100	1,2,3	Nearby interacting galaxies presented by Brassington et al. (2015).
SB	21	4,5	Galaxies dominated by star-formation.
AGN	29	5,6,7,8,9,10,11,12,13,14	Galaxies dominated by AGN.
LSM	49 ^a	15,16,17	Galaxies close to coalescence with a numerical interaction strength of 4 and 5 (Dopita et al. 2002).
Total	199 ^b		All galaxies.

Note: Sample, number of galaxies, references and brief description for the four samples used in work.

^a We present in this work 38 of the galaxies as 11 of the LSM sample galaxies are presented by Dietrich et al. (2018). We re-introduce physical parameters of NGC 2623 as part of the SB sample.

^b We found reliable SEDs in 189 galaxies (see Sect. 5), including the 11 galaxies presented by Dietrich et al. (2018).

References: (1) Keel et al. (1985), (2) Lanz et al. (2013, 2014), (3) Brassington et al. (2015), (4) Brandl et al. (2006), (5) Higuera-G. & Ramos P. (2013), (6) Stierwalt et al. (2013), (7) Keremedjiev et al. (2009), (8) Tommasin et al. (2010), (9) Weaver et al. (2010), (10) Pereira-Santaella et al. (2010), (11) Wu et al. (2011), (12) Dasyra et al. (2011), (13) Wu et al. (2011), (14) Guillard et al. (2012), (15) Wang et al. (2014), (16) Lintott et al. (2008, 2011) and (17) Dietrich et al. (2018).

neon emission lines indicative of high ionising flux (i.e., integrated line intensity ratios $[\text{Ne v}]/[\text{Ne II}] > 0.6$; see Sec. 4.2), and available archival *Herschel*/PACS and/or SPIRE photometry, as described below.

Our AGN sample includes three galaxies from the Great Observatories All-Sky LIRG Survey (GOALS, Stierwalt et al. 2013, a collection of Ultra-Luminous Infrared Galaxies (ULIRGs) with available *Spitzer*/IRS spectra), that meet our selection criteria: NGC 1068, NGC 7674, and MCG-03-34-63. We also include NGC 4151, a composite AGN/starburst galaxy (Higuera-G. & Ramos P. 2013) in which the AGN is the dominant contributor.

To these we added galaxies from a batch SIMBAD query (Wenger et al. 2000) for suitable targets. Specifically, we retrieved the brightest 20000 galaxies classified by SIMBAD as nearby ($cz \leq 29999 \text{ km s}^{-1}$) and as AGNs, which also had available photometry from *Herschel*/PACS and/or SPIRE. Of the 20000 galaxies satisfying the proximity, classification, and data availability constraints, we then searched for suitable neon line ratios. We required detections of both $[\text{Ne v}]$ and $[\text{Ne II}]$, and set a lower limit on the measured ratio $[\text{Ne v}]/[\text{Ne II}] > 0.6$.

Estimates of the neon line ratio $[\text{Ne v}]/[\text{Ne II}]$ for some galaxies appear in different works. In total, we obtained 54 measurements for 26 different galaxies from Keremedjiev et al. (2009), Tommasin et al. (2010), Weaver et al. (2010), Pereira-Santaella et al. (2010), Wu et al. (2011), Dasyra et al. (2011), Wu et al. (2011), and Guillard et al. (2012). The 26 objects satisfying all our selection criteria are classified primarily as Seyferts, including some with hidden broad-line regions. For example, Tommasin et al. (2008) classify MCG-03-34-63 as a non-Seyfert galaxy, but Tommasin et al. (2010) and Weaver et al. (2010) discuss a hidden broad-line region in this galaxy. In some cases the estimated line ratios were discrepant. When multiple measurements were available, we used the most recent, to make use of the best available calibration and pipeline for the data in question.

In summary, our sample of 29 AGN-dominated galaxies consists of one object drawn from Higuera-G. & Ramos P. (2013) (NGC 4151), one object from GOALS (MCG-03-34-064), two objects appearing in both GOALS and Higuera-G. & Ramos P. (2013), and 25 objects drawn from our SIMBAD search. The Fundamental properties of the AGN sample galaxies are given in Table A3.

2.4 The Late-Stage Merger Sample

The LSM sample is an extension of SIGS emphasizing mergers whose morphology is consistent with the system being close to coalescence. Although SIGS was designed to span the full range of galaxy interaction parameters by selecting strictly on the basis of interaction probability rather than morphology, activity, luminosity, or other derivative indicators, SIGS has relatively few systems at stages 4 and 5. In order to more thoroughly explore the full range of galaxy interactions, we assembled the LSM sample by filtering two catalogs. The first of these, the Revised *IRAS*-FSC Redshift Catalog (RIFSCz; Wang et al. 2014), consists of 60 303 galaxies selected from the *IRAS* Faint Source Catalog (FSC) that contains accurate redshifts and positions as well as some photometry for the galaxies therein. The second catalog, the Galaxy Zoo Data Release 1 (GZ1; Lintott et al. 2008, 2011), consists of almost 900,000 galaxies selected from the Sloan Digital Sky Survey (*SDSS*; Gunn et al. 1998, 2006; York et al. 2000; Doi et al. 2010). GZ1 galaxies were classified by the public into different categories including mergers. Our selection required that galaxies be at redshifts below $z = 0.06$, and that the fraction of the public votes that the galaxy was a merger was greater than 0.33. These criteria produced the 453 interacting systems that make up the LSM parent sample.

The authors then inspected composite SDSS images of all 453 LSM systems and estimated the merger stages using the same criteria applied earlier to the SIGS systems, as defined in Sec. 2.1. In the full LSM sample, only a minority of 24.9% of the sources were classified as being in merger stages earlier than 3, i.e., our selection criteria successfully prioritized advanced mergers marked by obvious morphological distortions that signify a merger near coalescence. In the present work, we analyze all LSM galaxies having available *Herschel*/SPIRE imaging available in the archive. We excluded galaxies that were truncated by the edges of the SPIRE mosaics. We identified a total of 49 LSM objects with suitable *Herschel*/SPIRE imaging for the present work. The basic properties of 38 of them are given in Table A4; those for the remaining 12 LSM objects appear in table 1 of Dietrich et al. (2018, hereafter D18). NGC 2623 is a special case of those remaining 12 objects, we re-introduce their physical parameters as part of the SB sample.

In this work we present new SEDs for 188 galaxies. Adding the 11 galaxies from D18 brings the total sample size to 199 galaxies. For reasons fully described in Sec. 5, Ten of those 199 galaxies lack SEDs suitable for reliable inferences about the AGN contributions,

so we subsequently analyse the implications of the SED fitting for only the 189 remaining galaxies.

3 SED ASSEMBLY

In Secs. 3.1–3.4 we describe in detail how the SEDs were constructed. In Sec 3.5 we also describe additional analysis carried out to retrieve mid-infrared emission line strengths for galaxies in the SB sample.

3.1 Image Sources

To ensure well-constructed SEDs, our approach was first, to assemble all available archival imaging spanning the widest possible wavelength range in the thermal regime, and second, to photometer all galaxies in all images within matching apertures. Thus our resulting SEDs fully reflect all the relevant thermal emission mechanisms because they capture the totality of the galaxies’ output at all thermal wavelengths, and they also have reliable colors, allowing us to accurately model the separate galaxy components that together comprise the SEDs.

We drew upon imaging data from the following space- and ground-based missions:

- *GALEX* (Martin et al. 2005, the Galaxy Evolution Explorer) for photometry in two ultraviolet bands, the far-ultraviolet (FUV) band centered at $0.152 \mu\text{m}$, and the near-ultraviolet (NUV) band at $0.227 \mu\text{m}$.
- SDSS DR12 (Gunn et al. 1998, the Sloan Digital Sky Survey) covering the $u, g, r, i,$ and z bands, at $0.354, 0.477, 0.623, 0.762$ and $0.913 \mu\text{m}$, respectively.
- 2MASS (Skrutskie et al. 2006, Two Micron All-Sky Survey) covering the $J, H,$ and K_s bands at $1.25, 1.65$ and $2.17 \mu\text{m}$, respectively.
- *Spitzer*/IRAC (Fazio et al. 2004, the Infrared Array Camera) providing mid-infrared coverage in up to four bands $3.6, 4.5, 5.8,$ and $8 \mu\text{m}$.
- *Spitzer*/MIPS (Rieke et al. 2004, the Multiband Imaging Photometer) covering up to three far-infrared bands at $24, 70,$ and $160 \mu\text{m}$.
- *WISE* (Wright et al. 2010, the Wide-Field Infrared Survey Explorer) which covered the full sky in four IR bands centred at $3.4, 4.6, 12,$ and $22 \mu\text{m}$.
- *IRAS* (Neugebauer et al. 1984, the Infrared Astronomical Satellite), another all-sky survey mission that provides photometry in four broad bands at $12, 24, 60$ and $100 \mu\text{m}$. The *IRAS* photometry used in this work is treated differently in that it was drawn from the Revised *IRAS*-FSC Redshift Catalogue (RIFSCz, Wang et al. 2014), under the assumption that the *IRAS* data therein are mature and well-characterised, and the photometry is reliable for total galaxy measurements. We likewise adopted the photometric uncertainties corresponding to the catalogued quality flags for the *IRAS* bands. We did not use catalogued upper limits.
- *Herschel*/PACS (Poglitsch et al. 2010, Photoconductor Array Camera and Spectrometer) covering up to three far-infrared bands at $70, 100$ and $160 \mu\text{m}$.
- *Herschel*/SPIRE (Griffin et al. 2010, Spectral and Photometric Imaging Receiver) providing far-infrared imaging at $250, 350,$ and $500 \mu\text{m}$.

For *GALEX*, *Spitzer*, *WISE*, and *Herschel* we relied on archived, publicly available mosaics. We verified the suitability of

the available imaging for each galaxy and each band by inspection. Mosaics in which the galaxies were truncated by mosaic edges, and mosaics in which the galaxies were saturated, were not considered valid and were not used. Some archival IRAC mosaics for 20 of our galaxies were not suitable for photometry because of saturation of the galaxy nuclei. Where possible, for these objects we generated our own IRAC mosaics by combining only the short exposures (typically 0.6 sec) from archived IRAC high-dynamic range observations. These short-exposures mosaics were not, generally speaking, saturated, and were in most instances suitable for the photometric analysis described below.

For SDSS and 2MASS, we constructed our own mosaics centered at the positions of the sources listed in Tables A1–A4, ensuring that they were sufficiently large that the source-free celestial backgrounds could be reliably estimated.

3.2 Background Estimation

Accurate background subtraction is crucial for accurate photometry. In the present work, background calculation began with masking of mosaic pixels containing unphysical values, e.g., unexposed pixels not suitable for photometry. We also created a mask for potential contaminating foreground sources (Milky Way stars) by flagging all pixels with a SNR higher than 3.0 for point sources. This step is crucial for accurate background estimation.

We tested two background estimation techniques on our masked science mosaics, both within the Python package *photutils*¹ (Bradley et al. 2018), an affiliated package of Astropy (Astropy Collaboration et al. 2013).² The first technique was *Local Background Subtraction*, where we used an external elliptical annulus of width equal to 10% of the elliptical aperture radius to estimate the background level around the galaxy. The second technique was *Global Background Subtraction*, where the image was analyzed using sigma-clipped statistics, and an overall background estimate of the image was obtained. We compared the global and local background calculations to those from our own custom calculation – also based on masked mosaics – within square regions far from the target galaxies. We found that *Global Background Subtraction* was significantly more accurate than the local technique, so we adopted it subsequently for all our photometry. This choice was validated when we found that our resulting *Herschel*/PACS+SPIRE photometry agreed with published values, within the uncertainties, for sources having published photometry. We speculate that the annuli used for the local background estimation were contaminated by low-level emission from the target galaxies at large radii.

3.3 Apertures, Inclinations, and Flux Densities

We used elliptical apertures to estimate total fluxes for all galaxies considered here. Specifically, for a given galaxy, the same aperture was used in every photometric band, to ensure accurate colors and thus reliable SEDs. Each aperture was sized to encompass the maximum apparent extent of each galaxy, as measured either in the *GALEX*/NUV or $3.6 \mu\text{m}$ IRAC mosaic (or, if the latter was unavailable, the $3.4 \mu\text{m}$ *WISE* mosaic). We inspected all mosaics of all galaxies with the apertures overlaid to ensure that no flux fell outside them. Based on those inspections, in some instances it

¹ <https://github.com/astropy/photutils>

² Further documentation is at <https://photutils.readthedocs.io/en/stable>.

was necessary to enlarge or shift the apertures and re-measure the photometry. Ultimately, all apertures were appropriately sized and located to enclose all of a galaxy’s flux in all available bands.

We applied appropriate *Herschel*/PACS aperture and colour corrections to account for missing flux due to incomplete sampling of the point spread function (PSF) in each of the PACS bands.

The pixel values within apertures were summed and converted to flux densities using the flux calibrations in the instrument handbooks. We accounted for absolute calibration error by adding appropriate instrument-dependent uncertainties in quadrature to the measurement uncertainties calculated in the standard way. These were as follows: 10% for *GALEX* (Morrissey et al. 2007), 2% for SDSS (Doi et al. 2010), 2% for 2MASS (Cohen et al. 2003b), 3% for IRAC (Cohen et al. 2003a), 4% for MIPS (Engelbracht et al. 2007), 6% for *WISE* (Wright et al. 2010), 10% for PACS (Poglitsch et al. 2010), and 7% for SPIRE (Swinyard et al. 2010). Typically, the calibration errors were much larger than the measurement errors for these relatively bright objects. No additional uncertainties were added to those already adopted from the RIFSCz for the flux densities measured in the *IRAS* bands.

We present our *GALEX* and SDSS photometry in Table A6, our 2MASS and *Spitzer*/IRAC photometry in Table A7, our *WISE* and *Spitzer*/MIPS photometry in Table A8, and finally our *Herschel*/PACS+SPIRE photometry in Table A9. When the photometry was consistent with zero flux density (i.e. the estimated uncertainty was greater than the estimated flux density) we chose not to include it in our SED models.

3.4 Photometry Validation

We verified that our approach yields high-quality photometry by comparing our measurements to previously published photometry. Specifically, we compared our *Spitzer*/IRAC+MIPS 24 μm photometry to that published previously by B15. Overall we found good agreement. In the following we describe the comparison in detail.

Figure 1 compares our IRAC and MIPS 24 μm photometry with that of B15 for all systems common to both studies.

Outliers are apparent, however, and some are significant. To understand the causes of the discrepancies, we obtained from B15 their Source Extractor (SE; Bertin & Arnouts (1996)) output files and examined them in light of our own output from *photutils*. Our findings are listed below in order of significance.

NGC 4933: For two galaxies in this system we used significantly smaller apertures than B15 (the B15 aperture diameters were factors of roughly 15 and 4 times those we used for NGC 4933C and B, respectively), which allowed us to avoid the nearby potentially contaminating IR-bright source SSTSL2 J130402.66–112854.1. We also shifted our aperture center for NGC 4933A by 11'' relative to B15 to avoid potential contamination from NGC 4933B.

NGC 1253A: The B15 aperture is roughly 10.4 times the size of ours. It is a faint source compared to its companion NGC 1253; a nearby bright star (TYC 4711-231-1) lies within the B15 aperture.

IC 1801: The B15 aperture is roughly 4.6 times the size of ours, and contains part of the core of NGC 935 and a nearby source (2MASS J02281028+1934207).

NGC 4567: The B15 aperture is roughly 2.7 times the size of ours, and overlaps with the core of NGC 4568. We shifted our aperture center by 23'' to avoid potential contamination from NGC 4568.

NGC 2820A: The B15 aperture is roughly 5.5 times the size of ours, and therefore includes a nearby star (2MASS J09212802+6413442) that likely contaminates their 3.6 and 4.5 μm photometry.

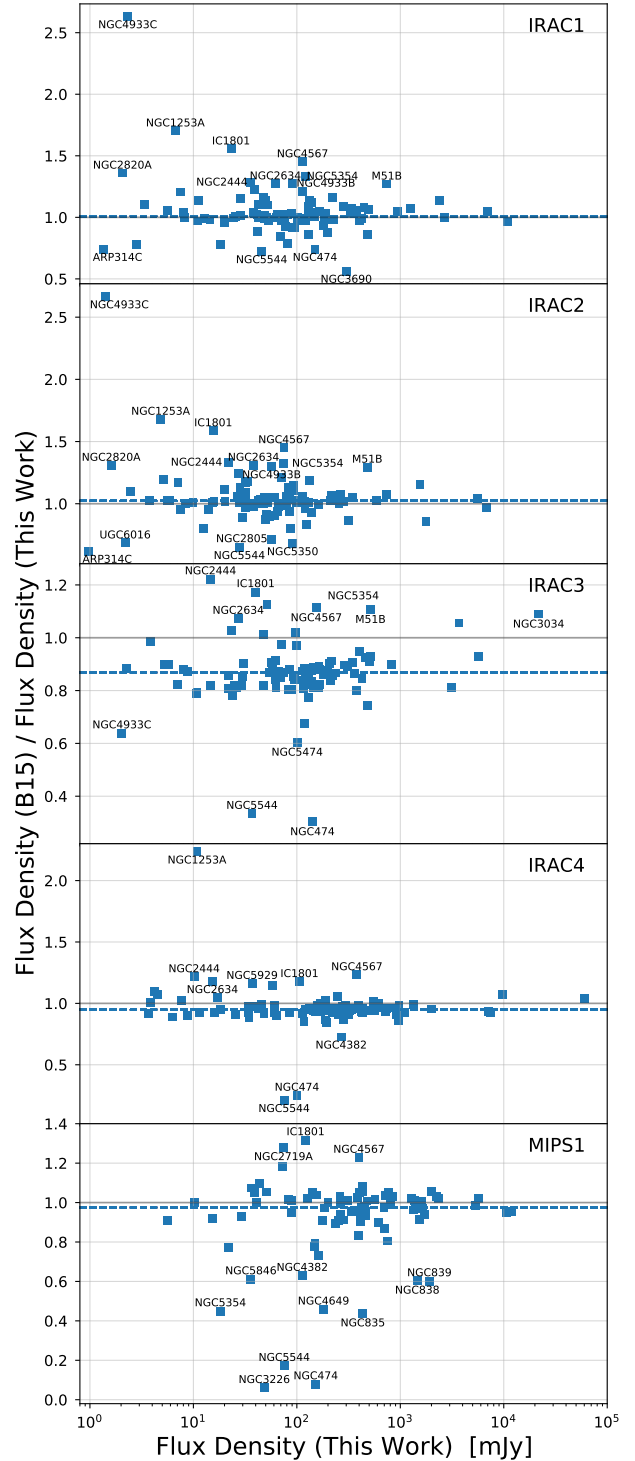


Figure 1. A comparison of our *Spitzer*/IRAC+MIPS global photometry to that of B15 for the SIGS galaxies. The photometry is consistent on average, but differences for individual galaxies are apparent. Most of the discrepancies are traced to different apertures, as described in Sec. 3.4.

NGC 5354: The **B15** aperture is roughly 6 times the size of ours, and covers the core of NGC 5353. The **B15** MIPS 24 μm photometry is only marginally lower (< 2 mJy) than our *WISE* band 4 photometry. Our photometry is however consistent with [Vaddi et al. \(2016\)](#). Due to contamination from the nearby NGC 5353, there appears to be considerable variation in the tabulated photometry of NGC 5354 in the literature ([Zucker et al. 2016](#); [Clark et al. 2018](#)).

NGC 2444: The **B15** aperture is roughly 2.1 times the size of ours. We offset our aperture center by $10''$ relative to the galaxy center to avoid potential contamination from the nearby galaxy NGC 2445. NGC 2445 is faint at 24 μm so the contamination in the MIPS 24 μm band is not significant.

IC 694 and NGC 3690: It appears that the **B15** aperture attributed to IC 694 actually corresponds to a portion of NGC 3690, and that the **B15** aperture for the latter is undersized.

NGC 2634: The **B15** aperture is roughly 4.2 times the size of ours, potentially admitting contaminating flux from several nearby sources.

M51B: The **B15** aperture is roughly 2.7 times the size of ours, and encompasses part of one arm of M51A. This is significant only for the 3.6 and 4.5 μm bands because the relevant portion of that arm of M51A is relatively faint at longer wavelengths.

NGC 5544: In this work we treat NGC 5544 and 5545 as a single system because they are inseparable at *Herschel* spatial resolution, whereas **B15** photometered them separately.

NGC 3034: Our aperture is roughly 2.4 times the size of that in **B15**, explaining the differences in IRAC3.

NGC 474: Our aperture is roughly five times the size of that in **B15**.

NGC 5474: The centroid of our aperture is offset from that of **B15** by $32''$ for this diffuse galaxy. Our 5.8 μm photometry is similar to that in [Dale et al. \(2005\)](#).

Arp 314C: Our aperture is roughly 1.4 times the size of that in **B15**. This is a faint galaxy, and is likely strongly affected by stars lying within the aperture, especially in the IRAC 3.6 and 4.5 μm bands.

UGC 6016: Our aperture is 1.3 times the size of that in **B15**, and is offset by $10''$ to avoid potential contamination of this relatively faint galaxy from nearby bright stars in the 3.6 and 4.5 μm bands.

NGC 5929: The **B15** aperture is roughly 1.5 times the size of ours, and our aperture is shifted relative to the galaxy center by $11''$ to avoid potential contamination from the nearby NGC 5930.

NGC 4382: Our aperture is roughly 0.77 times the size of that in **B15**. Our MIPS 24 μm and *WISE* 22 μm photometry is consistent with [Boselli et al. \(2014\)](#). Our IRAC 8 μm photometry is consistent with [Amblard et al. \(2014\)](#).

NGC 2719A: **B15** aperture is roughly twice the size of ours.

NGC 3226: Our aperture is less than half the size of that in **B15**. Our MIPS 24 μm and *WISE* 22 μm photometry is consistent with the *WISE* photometry reported in [Vaddi et al. \(2016\)](#) and [Ciesla et al. \(2014\)](#).

NGC 4649: Our MIPS 24 μm and *WISE* 22 μm photometry is consistent with the *WISE* photometry reported in [Vaddi et al. \(2016\)](#) and [Ciesla et al. \(2014\)](#).

NGC 835, NGC 838 and NGC 839: We obtain higher mid-infrared flux densities than **B15** for these galaxies. Our MIPS 24 μm photometry is consistent with [Johnson et al. \(2007\)](#) and [Bitsakis et al. \(2011\)](#). Our *WISE* 22 μm photometry is consistent with [Zucker et al. \(2016\)](#).

Having reached down to discrepancies of order 20% (specifically, 23, 23, 13, 19, and 22% in the IRAC 3.6, 4.5, 5.8, and 8.0 μm bands and the MIPS 24 μm band, respectively) relative to **B15** with-

out finding any serious faults with our photometry, we carried the comparison no further.

We also compared the *photutils* photometry for the IRAC 3.6 and 4.5 μm bands to what we measured with the same aperture in the very similar *WISE* bands 1 and 2. In addition, we compared our MIPS 24 μm photometry to that obtained in the similar *WISE* band 4 at 22 μm . The results are shown in Fig. 2. In general, the agreement is excellent. A small systematic flux underestimation is present in *WISE* for low IRAC fluxes showing that the background level is overestimated, but this only affects a few galaxies. We were able to resolve most of the discrepant cases with small shifts in aperture centers or diameters, or (in a few cases) by correcting an erroneous background estimate. When we were unable to understand and resolve a pair of discrepant bands, we chose not to use either of them in the subsequent analysis.

On the basis of these two comparisons – of our photometry measured in similar bands and measured by **B15** – and the fact that we visually inspected every mosaic for every galaxy with our *photutils* aperture overlaid, we are confident that our photometry is sound and that suitable for the SED modeling described in Sec. 4.1.

3.5 Mid-Infrared Spectroscopy of Galaxy Nuclei

Mid-infrared spectroscopy provides useful constraints on galaxy energetics because emission lines in the mid-infrared regime reveal the excitation conditions in the ISM nearly free of the usual complications from dust attenuation. For this reason we made use of *Spitzer*/IRS spectroscopy to help quantify the AGN contributions to our sample galaxies. Specifically, we used IRS short-high (SH) spectra of our SB sample galaxies to better understand their energetics via their neon and PAH features. In this Section we describe how we reduced and analysed those spectra. IRS spectra were taken for all our AGN sample galaxies as well, but we did not reduce them ourselves, we took the published neon line ratios from the literature to consistently fulfil the AGN sample selection criteria.

For each galaxy in the SB sample, we began with the SH basic calibrated data (BCD) produced by the IRS pipeline, covering wavelengths from 10 to 20 μm . We reduced the data in the standard way, first using IRSCLEAN to mask cosmic rays and bad pixels. We set the aggressive keyword to 0.5, so that a pixel which exceeds the sigma threshold could only be flagged as bad if it had no neighbours that also satisfied this criterion. We then used the CUBE Builder for IRS Spectra Maps ([Smith et al. 2007a](#), CUBISM) to combine the spatial and spectral information of the datasets, perform background subtraction, and generate a one-dimensional spectrum for each galaxy. We then used PAHFIT ([Smith et al. 2007b](#)) to estimate the strengths of the emission features in our spectra.

In general, this procedure worked well, although there were some exceptions. As was also found by [Brandl et al. \(2006\)](#), the nuclei of NGC 520 and Mrk 52 were observed slightly off-center. A more severe mis-pointing was revealed for NGC 3310. Thus for these three sources, our spectra do not represent all the emission from their nuclei. Results from these emission lines are bias to nuclear regions, so comparing with other galaxies not observed only in the nuclei can lead to different estimations. We assume that varying the physical scale of the systems will give similar results in terms of line ratios. The results of our IRS spectroscopy are described in Sec. 4.2 and the emission line strengths are tabulated in Table A5.

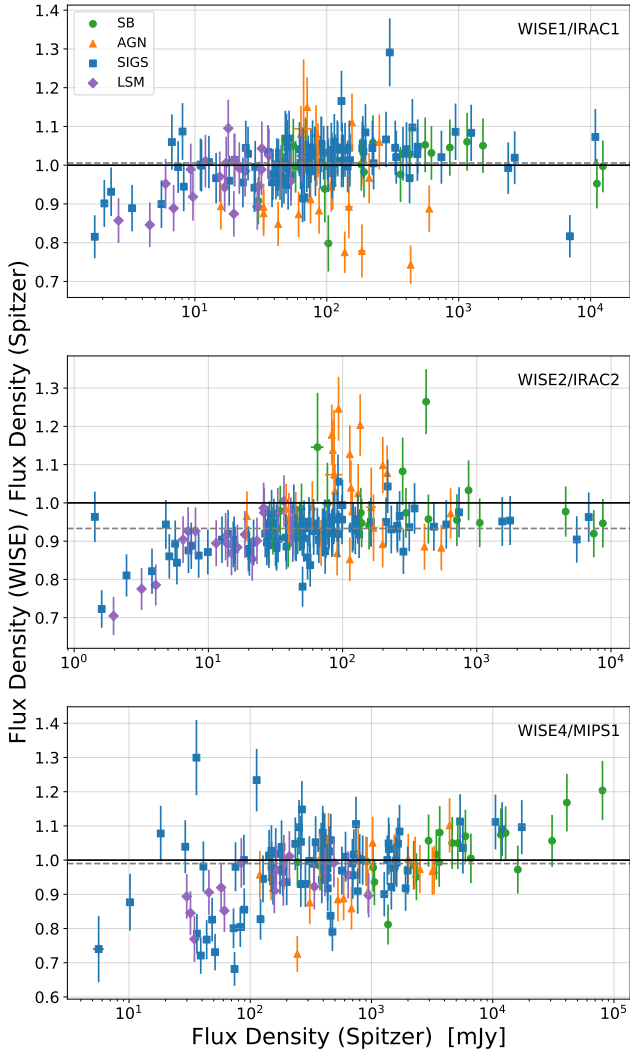


Figure 2. A comparison of our *Spitzer*/IRAC 3.6, 4.5, and MIPS 24 μm global photometry to that measured in the *WISE* 3.4, 4.6, and 22 μm bands for all galaxies in the SIGS, SB, AGN, and LSM samples. The gray dashed line shows the median value of the *WISE*-to-*Spitzer* ratio for all galaxies per panel.

4 ANALYSIS

This Section details how the SEDs compiled in Sec. 3.1 were modeled to estimate the contributions from young and old stellar populations, thermal emission from dust, and AGNs to the overall emission of each galaxy in our four study samples.

4.1 SED Modeling with CIGALE

This work relies primarily on CIGALE³ as the means of interpreting galaxy SEDs. CIGALE is a widely used fitting code, based on an energy balance principle, that attempts to model galaxy SEDs in terms of a combination of a small number of separate components that overlap in wavelength. A detailed description of the mechanics of CIGALE are available from Ciesla et al. (2015) and Boquien

et al. (2019); here we summarize only the main points relevant to our analysis.

CIGALE works by first populating a high-dimensional parameter grid of SED models consisting of all combinations of user-specified components that contribute to the emission, and then computes the goodness of fit for each model. CIGALE identifies the best-fit SED model by minimising the χ^2 statistic, and produces probability distribution functions for the model grid parameters by assuming Gaussian measurement errors (Burgarella et al. 2005; Noll et al. 2009; Serra et al. 2011). Most relevant to the present work is the fact that CIGALE implements convenient templates for emission from an obscured AGN, based on the models described in Fritz et al. (2006).

We used the parameters and values given in Table 2 to define the CIGALE grid of model galaxy SEDs. Except as noted below, the parameter settings were identical to those of D18. For all parameters not shown in Table 2, we adopted the CIGALE default settings. All fits were performed assuming the distances given in Tables A1-A4.

We treated the galaxies' star formation histories (SFH) with a delayed SFH model, taking that as a reasonable approximation for the SF history during the last ~ 10 Myr. This approach assumes a single past starburst event (Ciesla et al. 2015). The parameters that control the delayed SFH model are the age of the oldest stars in the galaxy, and the folding time (τ_{main}) of the exponential decay in star formation after the starburst occurs. Depending in the combination of these two parameters, we can simulate ongoing or recent starburst events.

The stellar emission was modeled with the standard Bruzual & Charlot (2003) population synthesis libraries, weighted by the SFH. We used the default CIGALE nebular emission module. The module controlling UV attenuation followed Calzetti et al. (2000) and Leitherer et al. (2002). This module is parameterized by the young population color excess $E(B - V)_{\text{young}}$ of stellar continuum light, the reduction factor of the color excess for the old population $E(B - V)_{\text{old factor}}$ as compared with the young population, the UV bump central wavelength, FWHM, and amplitude (the CIGALE default values for these parameters of 2175 \AA , 350 \AA , and 0 were used), and the power-law slope (δ) which modifies the attenuation curve.

The dust emission was modeled following Dale et al. (2014), implementing a modified blackbody spectrum with a power-law distribution of dust mass at each temperature,

$$dM \propto U^{-\alpha} dU \quad (1)$$

where U is the local heating intensity.

We adopted the same overall AGN model as D18 to estimate the AGN fraction f_{AGN} in our sample galaxies, i.e., the Fritz et al. (2006) model. Because one of our primary goals is to investigate the emission fraction coming from the obscured AGNs in our sample galaxies, we sampled the AGN fraction parameter f_{AGN} somewhat more finely than D18, in steps of 0.05 between 0.1 and 0.9, as well as at 0.0 (i.e., zero AGN contribution). We adopted a single value for the viewing angle into the AGN ($\psi = 30.1$), as intermediate between type 1 and 2 AGNs. We tested the effect of varying the viewing angle in the samples of this work. We run a similar grid as in Table 2 with half of the steps for α and β , and adding $\psi = 70.1$. In general, changing the angle does not usually make a significant difference in the output parameters. However, we also find that CIGALE can identify Type 1 AGNs: their output parameters, especially stellar mass, suddenly become sensitive with $\psi = 70.1$ and a lower χ^2 compared with $\psi = 30.1$. We detected six AGN galaxies that fall into this category, all of them are already known to be Type 1

³ <http://cigale.lam.fr/>, version 0.12.1

Table 2. CIGALE grid parameter values adopted for the modeling described in Section 4.1

Parameter	Values	Description
Star formation history (SFH): Delayed		
τ_{main}	50, 500, 1000, 2500, 5000, 7500	e-folding time of the main stellar population model (Myr).
Age	500, 1000, 2000, 3000, 4000, 5000, 6000	Age of the oldest stars in the galaxy (Myr).
Single-age stellar population (SSP): Bruzual & Charlot (2003)		
Separation Age	10	Age of the separation (to differentiate) between the young and the old star populations (Myr).
Dust attenuation: Calzetti et al. (2000)		
$E(B - V)_{\text{young}}$	0.1, 0.25, 0.4, 0.55, 0.7	Color excess of the stellar continuum light for the young population.
$E(B - V)_{\text{old factor}}$	0.22, 0.44, 0.66, 0.88	Reduction factor for the $E(B - V)$ of the old population compared to the young one.
Power-law slope (δ)	0.0, 0.25, 0.5	Slope delta of the power law modifying the attenuation curve.
Dust emission: Dale et al. (2014)		
α	1.0, 1.25, 1.5, 1.75, 2.0, 2.25, 2.5, 2.75, 3.0	Alpha from the power-law distribution in eq. 1.
AGN model: Fritz et al. (2006)		
$R_{\text{max}}/R_{\text{min}}$	10.0, 30.0, 60.0, 100.0, 150.0	Ratio of the maximum to minimum radii of the dust torus.
τ	0.1, 0.6, 1.0, 6.0, 10.0	Optical depth at $9.7 \mu\text{m}$.
β	-1.00, -0.75, -0.50, -0.25, 0.00	Beta from the power-law density distribution for the radial component of the dust torus (eq. 3 of Fritz 2006).
γ	0.0, 2.0	Gamma from the power-law density distribution for the polar component of the dust torus (eq. 3 of Fritz 2006).
Opening Angle (θ)	60.0, 100.0, 140.0	Full opening angle of the dust torus (Fig 1 of Fritz 2006).
ψ	30.1 ^a	Angle between equatorial axis and line of sight.
f_{AGN}	0.1 – 0.9 in steps of 0.05	Fraction of AGN torus contribution to the IR luminosity (fracAGN in Equ. 1 of Ciesla 2015)

^a The apparent precision was adopted to accommodate an idiosyncrasy in CIGALE’s mode of operation, fractional degree precision is not implied.

Seyfert AGN. We present the derived parameters for those galaxies with $\psi = 70.1$ in Table A14. We use these lower χ^2 values in all the Figures of this work. A new version of CIGALE, “X-CIGALE” (Yang et al. 2020), has been recently released that is specifically designed to be more attentive to the angle and to the high-energy contributions to the SED. A study focusing on Type 1 AGN will benefit from both this new version and from a more detailed angle analysis, but is beyond the current work.

We also sampled α in increments of 0.25 between 1.0 and 3.0, and extended the values for the slope delta power-law modifying the dust attenuation curve (0.25 and 0.5 in addition to 0), the optical depth at $9.7 \mu\text{m}$ (including 0.1) and the density radial exponent of the torus (adding the values -0.5 , -0.25 , and 0). Our tests indicate that by choosing a compact grid of values for α and f_{AGN} , and a single value for the viewing angle into the AGN $\psi = 30.1$, we can obtain well-behaved PDFs for these grid-parameters (i.e., they are well resolved probability distributions). We might therefore expect an improvement relative to the measurements of D18 because of the more finely sampled parameter space.

Our strategy was to run two different families of CIGALE models. The first family included AGNs parameterized according to Table 2, while the otherwise identical second family was run without. We adopted this approach because D18 found that f_{AGN} was typically uncertain by $\pm 10\%$. Thus, cases when $f_{\text{AGN}} < 0.20$ are not inconsistent with $f_{\text{AGN}} = 0$, i.e., no AGN being present. We therefore chose to treat cases for which $f_{\text{AGN}} < 0.20$ as if they had no AGN. We thereby avoid the pitfall noted by Ciesla et al. (2015) i.e., that the AGN contribution can be overestimated, an effect often seen

when deriving low-valued parameters with truncated PDF analysis (Noll et al. 2009).

We present some examples of the best SED fitting for each of the four samples presented in this work in Figures A1–A4.

4.2 Neon emission lines

The MIR provides spectral features that are excited by the intense UV radiation from massive young stars. Among the most prominent infrared emission features are the PAHs bands that arise in the photon-dominated regions (PDR) around HII regions. Also, the forbidden nebular lines emitted by ionised atomic gas play an essential role in the characterisation of the gas physics.

Strong radiation fields such as those around AGNs are necessary to reach the ionization potential (IP) of the [Ne v] emission line at $14.3 \mu\text{m}$ (97.1 eV). Such radiation strength is unlikely to be produced by star formation (Sturm et al. 2002; Brandl et al. 2006). This line is therefore used as a tracer of AGN activity.

An additional advantage of using the [Ne v] emission line relates to the fact that dust extinction at $15 \mu\text{m}$ is small and typically independent of the orientation (Wu et al. 2011). Goulding & Alexander (2009) show that optical spectroscopic surveys, in contrast, can miss approximately half of the AGN population due to extinction through the host galaxy. Genzel et al. (1998) found a correlation between the strength of emission lines, higher stages of ionisation, and the level of AGN activity. Therefore, [Ne v] can be used to quantify AGN activity. The forbidden [O IV] at $25.9 \mu\text{m}$ is also used for similar reasons. This line has a lower IP (54.9 eV) and is detected

in a more significant fraction of AGNs, but can also be produced in star-forming galaxies, mainly in the presence of WR stars and ionising shocks (Abel & Satyapal 2008; Pereira-Santaella et al. 2010; Weaver et al. 2010; Alonso-Herrero et al. 2012). Although [O IV] has proved to be useful as an AGN tracer by some authors (Veilleux et al. 2009; Gruppioni et al. 2016), here we have decided to use the [Ne v] emission only, in order to avoid any contamination from star formation.

The [Ne II] low ionisation line at $12.8 \mu\text{m}$ ($IP = 21.6 \text{ eV}$) traces the thermal stellar emission in star-forming galaxies (Sturm et al. 2002). Therefore, comparing its strength to that of the [Ne V] line provides a straightforward measurement of the relative contribution from star formation and AGN to the overall energy budget. The proximity of the two neon lines in wavelength implies that both of them are subject to similar extinction (Tommasin et al. 2010). A caveat is that the [Ne II] line blends with the PAH feature at $12.7 \mu\text{m}$ and the [Ne v] line blends with the [Cl II] line. We work under the assumption that the effect of this blending in the estimation of the line strengths is not very significant. As noted in Goulding & Alexander (2009), it is safe to make this assumption when high signal-to-noise data is available, as is our case. In the present work the uncertainty in line strengths due to blending is smaller than the uncertainty due to instrumental and detection effects.

The [Ne v]/[Ne II] line ratio has been used to calibrate the relative AGN contribution to the total infrared luminosity of galaxies (Genzel et al. 1998; Sturm et al. 2002; Tommasin et al. 2008; Veilleux et al. 2009; Tommasin et al. 2010; Wu et al. 2011; Dixon & Joseph 2011; Díaz-Santos et al. 2017, among others). For example, Wu et al. (2011) estimate a 100% AGN contribution corresponding to a [Ne v]/[Ne II] ratio of ≈ 1.0 and a 0% AGN contribution corresponding to a [Ne v]/[Ne II] ratio of ≈ 0.01 . As pointed out by Petric et al. (2011), discrepancies in the measured contribution of the AGN to the bolometric luminosity can be due to different calibrations of the line ratio. For instance, Pereira-Santaella et al. (2010) have argued that for pure AGN emission, the line ratio should be closer to [Ne v]/[Ne II] $\approx 2-3$.

The fluxes of the [Ne v] lines for 19 of the 23 galaxies in the SB sample, are presented in Table A5 along with other useful lines in the Spitzer SH mode⁴: the [Ne III], [S III], [S IV], [Fe II] and H₂ S(2) and H₂ S(1). For Mrk 52, NGC 23, NGC 253 and NGC 7714 we took upper limits from the literature (Bernard-Salas et al. 2009; Pereira-Santaella et al. 2010) and we use those values for comparison.

Although the results for the SB sample fall in a region dominated by upper limits in the detection of the [Ne v]/[Ne II], some of the results could be affected by the adopted emission-line detection procedure and signal-to-noise ratio threshold used in weak cases, as noted by Goulding & Alexander (2009). Most of the spectroscopic data come from the nuclear region of the galaxies, so when we compare with the global values of the galaxies in the SED for the given apertures, we are comparing global characteristics with a measure of the central emission (most predominant) region of the samples.

5 DISTRIBUTIONS OF DERIVED GALAXY PROPERTIES

This section describes the CIGALE-based SED fitting results for the 199 objects in the SIGS, SB, AGN, and LSM subsamples described in Sect 2. The large overall sample size and the well-defined

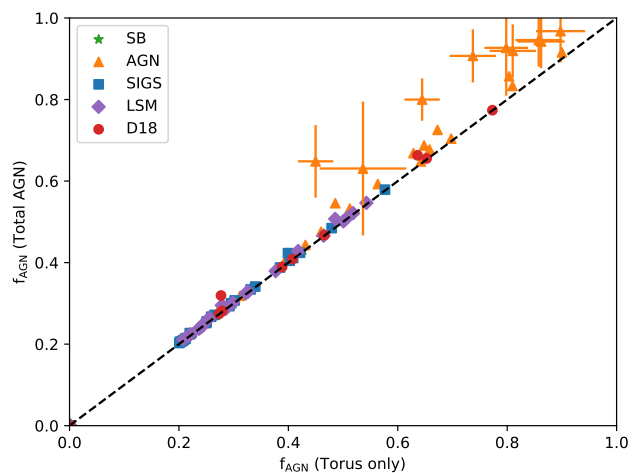


Figure 3. The total AGN contribution to the infrared luminosity, f_{AGN} , compared to the fractional contribution from the molecular torus alone in CIGALE’s implementation of the Fritz AGN model. For clarity, error bars are only shown for galaxies that deviate significantly from the line of equality. The uncertainties for points without drawn error bars are similar. Symbols indicate which of the four subsamples the objects belong to (Sec. 2); the D18 galaxies are also shown. Here and in the main text we use f_{AGN} to indicate the total AGN fraction, which differs from the popular convention that considers emission only from the torus (see Sec. 5). The distinction matters for a significant number of objects in the AGN sample.

subsets facilitate some useful statistical comparisons. A total of 94 objects have $f_{\text{AGN}} \geq 0.2$; for these objects we present the CIGALE parameters as computed. For the remaining objects we present the CIGALE parameters as computed with their AGN contribution set to zero. Ten galaxies (marked with an ^b in Tables A1–A4) have sparse photometric coverage and consequently lack reliable SED fits; we omit these objects from further analysis.

Out of the ~ 60 parameters that CIGALE estimates, we focus on those most relevant to star formation and AGN activity; the parameters we emphasize are listed in Tables A10–A13.

CIGALE treats the AGN as a composite object consisting of contributions from three elements in the context of the Fritz model, namely: 1) the primarily mid-IR emission arising from the molecular torus, 2) the emission from the accretion disk in the optical and near-IR, and 3) light scattered from the torus. The CIGALE parameter f_{AGN} is typically used to mean the ratio of the mid-IR emission from the torus only to the total infrared luminosity (see for example D18). However, our investigations show that the emission from the torus does not accurately account for the total AGN output for some of our galaxies (Fig. 3). In most cases this makes very little difference, as demonstrated by the near one-to-one correlation between f_{AGN} (TOTAL) and the fractional contribution arising only from the torus (f_{AGN} (Torus Only), in Fig. 3). Therefore, throughout this work we define f_{AGN} as the contribution coming from the torus. We find that nine objects (NGC 3516, NGC 5548, ESO 141-55, Mrk 771, Mrk 841, Mrk 1383, Mrk 1513, Mrk 335, and 2XMM J141348.3+440014) are significant outliers of this correlation. All of them are characterized by an accretion-disk luminosity that exceeds that of the torus, including both the thermal and the scattering components, as calculated by CIGALE using the Fritz model. They all have good wavelength coverage in their SEDs and reliable CIGALE fits, with reduced- χ^2 between 1 and 3. No other CIGALE parameters single out these objects as having high

⁴ With a slit size of $4.7'' \times 11.3''$

accretion or identify them as unusual in other ways. The SFRs in this set, for example, vary from about $30.5 M_{\odot} \text{ yr}^{-1}$ (Mrk 1513) to $0.04 M_{\odot} \text{ yr}^{-1}$ (NGC 3516). The most extreme outlier, Mrk 771, has an accretion luminosity almost five times larger than its torus emission. This object is noted for having soft X-ray excess emission of $0.15 \times 10^{-11} \text{ erg cm}^{-2} \text{ sec}^{-1}$ (Boissay et al. 2016). The excess in the soft band and the high accretion luminosity favors an interpretation in which UV photons from the accretion disk are comptonized by the electrons in the hot plasma (comptonization) as the cause for excess soft emission (Boissay et al. 2016).

For purposes of qualitative illustration, we collect the CIGALE model SEDs in Fig. 4. We indicate the median-averaged SEDs with bold lines, normalized to their K_S flux densities, for each of our four subsamples, together with the most likely fitted SEDs. Some aspects of the SEDs are immediately evident. For example, the SB and LSM subsamples show qualitatively similar overall behavior, which suggests that star formation dominates the SEDs of the LSM galaxies. There is however a weak bump in the median SB and LSM SED at about $50 \mu\text{m}$ of uncertain origin; it may reflect the presence of warm dust. The AGN sample has a higher median ratio of NIR to FIR flux than do any of the other samples. It also, unsurprisingly, has a higher median ratio of MIR to FIR flux, reflecting the presence of the hot dust associated with the AGN component. Finally, the SIGS sample shows the greatest variety in individual galaxy SEDs. The latter can be understood as reflecting the much larger variety of star formation activity present throughout the merger sequence as compared with our other samples.

We calculated IR luminosities (L_{IR}) by integrating the best fitted SEDs from 5 to $1000 \mu\text{m}$. We chose this definition to conform to that in Fritz et al. (2006), to account for PAH features between 5 and $8 \mu\text{m}$, and to avoid the near-infrared stellar emission that enters into the 1-5 μm window. When the contribution of the AGN to the SED drops below about 20% it becomes increasingly difficult to use the SED to reliably determine the Fritz parameter values.

To illustrate the effect of low AGN fractions in the accuracy of our results, in Figure 5 we include all fits with f_{AGN} fraction values larger than 15%, i.e., we include objects that are below the 20% threshold of what we consider reliable AGN fractions. The uncertainties of these points in the plots are not any larger than those of higher AGN fraction, but a closer look at the SED fits and their reduced- χ^2 in all samples prompt us to use the 20% cutoff in the remaining figures so that genuine effects can be highlighted. (A galaxy whose AGN contribution is less than 20% is then reanalyzed with CIGALE with the AGN parameters set equal to zero, and the other resultant parameter values are the ones listed in the Tables.) The left panel of Fig. 5 shows no clear relation between f_{AGN} and L_{IR} for any of the subsamples considered here, but it does clearly reveal the tendency of the AGN sample galaxies to host strong and in some cases dominant AGNs. Measurable AGN contributions are only present at IR luminosities above $\sim 10^{9.5} L_{\odot}$.

f_{AGN} is plotted as a function of $L_{\text{AGN}}/L_{\text{IR}}$ (L_{AGN} from CIGALE output) for all modeled galaxies in the right panel of Figure 5. The expected relationship is apparent, and at the smallest values of f_{AGN} the flattening confirms our decision to limit further analyses to values exceeding 20%. Toward large ratios, the trend in f_{AGN} flattens and becomes more scattered. The flattening is the result of a larger fraction of the AGN luminosity being emitted at UV wavelengths for the brightest AGNs. The scattering, on the other hand, is explained by the different levels of obscuration in each case, related to geometrical (i.e., inclination) effects, and the contribution of the f_{AGN} coming only from the torus (Fig. 5).

5.1 Galaxy Properties by Merger Stage

We segregated the LSM+SIGS galaxies by merger stage and compared them to the SB and AGN subsets using a Kolmogorov-Smirnov (KS) test to determine how statistically different the derived parameters are between samples. The KS statistic is a measure of how likely it is that two distributions are consistent with being two realizations of the same underlying distribution. The higher the KS probability between two parameter distributions, the more likely it is that they are coming from the same parent distribution.

Lanz et al. (2013) reported KS tests on a smaller sample of mergers in the original SIGS program (before the availability of Herschel data) and tentatively did not find statistically significant correlations between SED shape, merger stage, and star-forming properties. With our enlarged study sample, analyzed with an SED code that does take into account the AGN contribution, we are more successful at finding meaningful statistical differences.

We summarize the results of this comparison for selected parameters in Table 3 and present the distributions for SF and SFR in Fig. 6. Analogous results for the other derived parameters are presented in Fig. A5.

The KS tests reveal a number of trends:

- First, the parameter distributions of advanced merger stages (4,5), especially f_{AGN} , M_* , and α_{dust} , are most similar to those of the starburst sample, and are less statistically correlated with the parameters of the AGN sample.
- Second, KS scores for consecutive stages (2-3, 3-4, 5-6) are higher than for non-consecutive stages, with the smallest correlation occurring for stages that are farther apart along the merger evolution (e.g. 2-5), which is expected if the properties of the system evolve gradually as the merger progresses.
- Third, apart from their dust luminosities and $E(B - V)$ values, the AGN sample parameters have a very small statistical correlation with the parameters of any other samples, but the KS scores are slightly larger between the AGN galaxies and the advanced merger stages than between AGN and the early merger stages.
- Fourth, lowest statistical correlation occurs between the SB and the AGN samples, even for parameters that tend to be correlated between all the other samples.
- Finally, the parameters that show more dispersion between samples are f_{AGN} and α_{dust} , which implies that they are the most useful parameters to discriminate between galaxy types.

The picture that emerges from these results (and from the overall SED shapes in Fig. 4) is in agreement with a classical interpretation: in the local Universe, mergers trigger starburst activity in galaxies (Hopkins et al. 2006; Pearson et al. 2019). They also trigger AGN activity, but to a lesser extent (Hopkins et al. 2006; Satyapal et al. 2017; Blecha et al. 2018; Dietrich et al. 2018).

5.2 Dust spectral slope (α) and the star formation main sequence

Fig. 7 shows how galaxies from the four samples populate the $M_* - \text{SFR}$ plane, using M_* and SFR results from CIGALE. The so-called star formation main sequence (MS) is usually defined in terms of a positive correlation followed by star-forming galaxies between star formation rate and stellar mass. Both Figs. 6 and 7 show that the SB and stage 5 galaxies indeed lie in a narrow and relatively high range of SFRs. We have color coded the symbols according to their CIGALE-derived estimates for α , the exponent of the power law defined in Eq. 1, which parametrizes the average dust temperature.

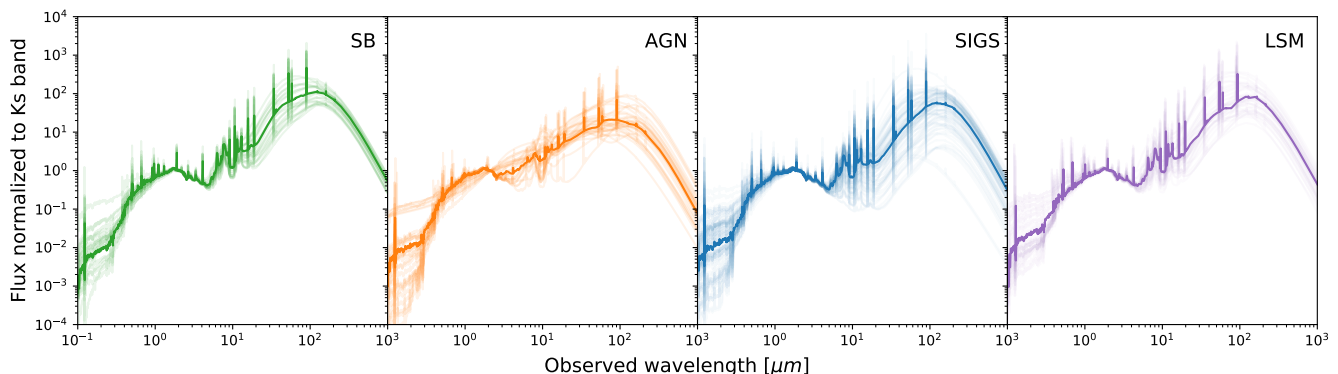


Figure 4. Model spectra normalized in the K_s band for all galaxies in this work, separated by sample. From left to right: the SB sample (in green), the AGN sample (in orange), the SIGS sample (in blue), and finally the LSM sample (in violet). Faint spectra are those of individual galaxies. The bold lines indicate the median-averaged spectra for the full subsamples. This comparison highlights the differences seen among the subsamples on average, especially those of the AGN sample in the mid-infrared relative to the other samples.

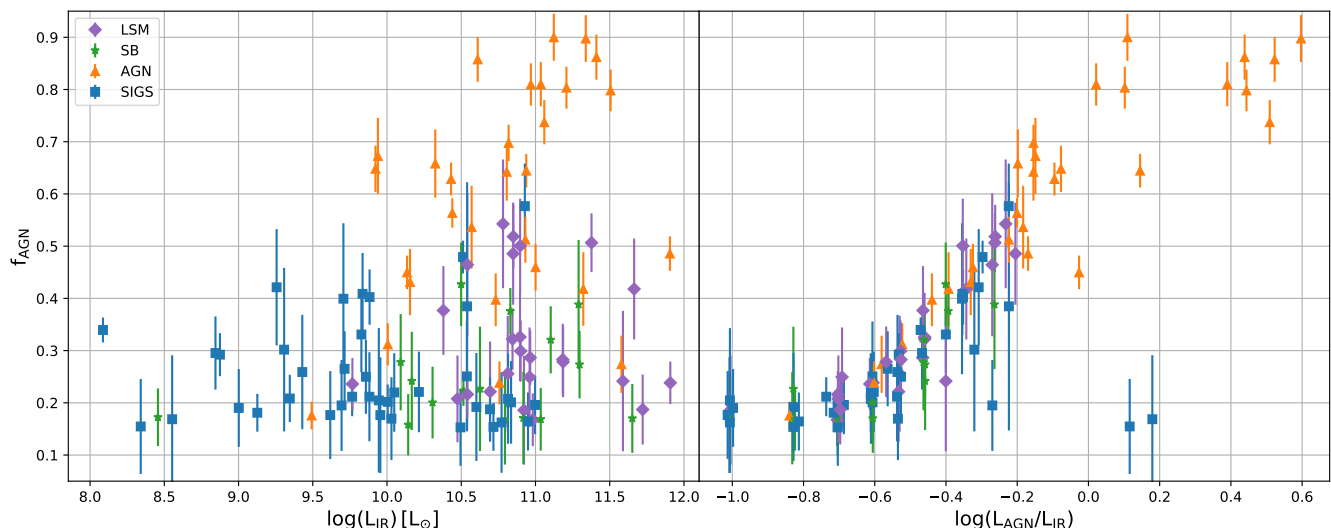


Figure 5. CIGALE-estimated total fractional AGN contribution to the IR luminosity versus CIGALE-estimated total luminosities for the SIGS (blue squares), SB (green stars), AGN (orange triangles) and LSM (violet squares) galaxies. *Left panel:* AGN fraction as a function of L_{IR} . Unsurprisingly, the AGN sample behavior is distinct from that of the other three subsamples. *Right panel:* AGN fraction as a function of the ratio of AGN luminosity and L_{IR} . AGN emission at UV wavelengths can in some cases drive the ratio of AGN luminosity to IR luminosity to values greater than unity.

For the same range of masses, the AGN and SIGS samples extend to lower ($< 10^{-1} M_{\odot} \text{ yr}^{-1}$) SFRs compared to the other two samples.

The bulk of the SIGS galaxies follows the MS over three orders of magnitude in stellar mass, and over four orders of magnitude in SFR. There are some outliers at low SFR, consistent with these being quiescent galaxies. The LSM and SB galaxies also seem to follow the MS, but they are more massive, than the SIGS sample and consequently show higher values of SFR. The AGNs in our sample have masses limited to a narrow range between $10^{10} M_{\odot}$ and $4 \times 10^{11} M_{\odot}$ and a broad range of SFRs.

The behavior of the AGN galaxies is notable especially when we consider dust temperatures as parametrized by α . For all the other samples, dust temperature positively correlates with sSFR, that is, for a given stellar mass, dust becomes hotter (alpha decreases) as SFR increases. Using simulations and observations of SIGS galaxies, [Martínez-Galarza et al. \(2016\)](#) have shown that this evolution

of the dust temperature as galaxies depart the MS is linked to the interaction stage: initially (at early interaction stages) galaxies have low SFRs and relatively cool dust temperatures, but SFR and dust temperature both increase as the systems approach coalescence. This is related to an increase in the *compactness* of the ISM, i.e. the average distance of the dust to the heating sources, normalized by the luminosity of the source.

We observe a similar evolution of dust temperature with distance from the MS for the SB and LSM samples. The AGN sample, however, is different. For AGN sample galaxies the α parameter is completely uncorrelated with the location of the system relative to the MS, and moreover, SEDs compatible with hot dust are observed at very low SFRs. The average dust temperature is therefore not controlled by star formation in AGN-dominated galaxies, and the concept of compactness should be interpreted from a different perspective for these systems.

Table 3. Results of KS tests comparing fitted parameters by subsample.

Samples Compared	f_{AGN}	L(AGN)	E($B - V$) (Old Stars)	E($B - V$) (Young Stars)	α (Dust)	L(dust)	SFR	age(stars)	Mgas	M_*	sSFR
2-3	0.44	0.42	0.95	0.96	0.24	0.88	0.91	0.62	0.59	0.92	0.24
2-4	0.3	0.05	0.01	0.01	0.38	<0.01	0.01	0.07	0.42	0.26	0.5
2-5	0.12	0.01	0.03	0.03	0.34	0.02	0.05	0.75	0.49	0.49	0.07
2-AGN	<0.01	<0.01	<0.01	0.66	<0.01	0.02	0.84	0.19	<0.01	<0.01	0.09
3-4	0.43	0.18	<0.01	0.01	<0.01	0.01	0.02	0.26	0.63	0.49	0.1
3-5	0.21	0.02	0.03	0.08	0.06	0.05	0.17	0.8	0.22	0.22	0.14
3-AGN	<0.01	<0.01	<0.01	0.86	<0.01	<0.01	0.76	0.03	<0.01	<0.01	<0.01
4-5	0.61	0.42	0.51	0.97	0.84	0.83	0.98	0.92	0.51	0.51	0.38
4-AGN	<0.01	<0.01	0.31	0.06	0.08	0.43	0.10	0.01	0.01	0.04	<0.01
5-AGN	<0.01	0.02	0.56	0.15	0.38	0.56	0.15	0.17	0.07	0.07	<0.01
SB-2	0.31	0.03	0.01	0.01	0.11	<0.01	0.01	0.2	0.43	0.41	0.05
SB-3	0.61	0.05	<0.01	0.01	<0.01	<0.01	0.02	0.44	0.35	0.35	0.1
SB-4	>0.99	0.85	0.22	0.43	0.42	0.43	0.43	0.76	0.98	0.99	0.18
SB-5	0.53	0.38	0.08	0.64	0.93	0.26	0.48	0.85	0.58	0.64	0.96
SB-AGN	<0.01	<0.01	0.07	0.01	0.60	0.07	0.04	0.03	0.04	0.09	<0.01
noAGN-AGN	<0.01	0.01	0.18	0.03	<0.01	0.28	0.04	0.01	0.02	0.02	<0.01

Note. KS-derived probabilities indicating the likelihood that the CIGALE-derived parameter distributions (column headings) for two galaxy subsamples were drawn from the same parent sample. The left-hand column indicates the two samples tested. For this test, the SIGS and LSM samples were combined and then divided into merger-stage-based subsamples. The numbers in the left column indicate the merger stage used. The 9th column [age(stars)] refers to the mean age of the stellar population. Because the subsamples were relatively small (e.g., 29 AGN galaxies), we made no attempt to refine probabilities below 1% (> 99% confidence that the two samples differ).

Perhaps more relevant here is that by disentangling AGN and SF activity we can obtain more reliable SFR estimates for these systems unbiased by the thermal emission from the AGN. We also corroborate that mergers can be an important factor in contributing to the scatter of the MS, since galaxies move away from the MS as they evolve into later phases of the merger. One additional note has to do with quenching. Although the SIGS galaxies lying below the MS (as indicated by the dot-dashed lines in Fig. 7) are most likely quenched systems with small or negligible gas reservoirs, some of the galaxies that we would infer to be actively forming stars might actually be recently quenched systems where the stars formed right before the quenching are still dust-enshrouded, as demonstrated in Hayward et al. (2014). Additionally, the fact that we find AGN systems below the MS suggests AGN activity persists after the quenching, even at very low levels of SF.

Figure 8 shows how galaxy morphology affects location within the star-forming main sequence by using the method of de Vaucouleurs et al. (1991), which assigns numerical values to the Hubble stages (usually called T values, de Vaucouleurs 1977). We were unable to classify four galaxies (2XMM J141348.3+440014, 4U 0557-385, LEDA 68751, Mrk 1383), which was unsurprising given that these are among the most distant galaxies in this work. For three galaxies with morphologies not available in de Vaucouleurs et al. (1991) we use the NASA/IPAC Extragalactic Database (NED). The three galaxies classified using NED are ESO 033-02 (a SB0; T= -3), Mrk 841 (E; T= -5), and MCG-03-34-064 (S0/a and S0+ are both given; we assigned it T= -0.5). Not all galaxies have T values in the range from -6 to 11. Six are classified as Non-Magellanic irregulars (NGC 2820A, NGC 2968, NGC 3034, NGC 3077, NGC 3448, M51B) and three as peculiar irregulars (NGC 2623, NGC 3256, NGC 520). For close mergers (NGC 4038/4039 and NGC 5614/5615) we only use the information of the most prominent galaxy. We were unable to determine morphologies for seven galaxies with NED or a literature search;

these object were ESO 141-55, ESO 383-35, Mrk 1502, Mrk 1513, Mrk 335, Mrk 771, and IC 694). They do not appear in Figure 8.

Unsurprisingly, most of early type galaxies lie in the quiescent region (below the lowest diagonal line) of the MS diagram, while most of the spiral galaxies follow the MS. No obvious trend is apparent for the irregular galaxies, which scatter widely in SFR for a given stellar mass. This is in harmony with the demographics of disk-dominated (“blue cloud”) and spheroid-dominated (“red sequence”) systems (Kauffmann et al. 2003; Brinchmann et al. 2004; Somerville & Davé 2015).

The emission from warm dust is an essential contributor to the SED in most stages of mergers. Martínez-Galarza et al. (2016) found that the compactness parameter C that relates the distribution of dust temperatures with the geometry of the environment is correlated with the sSFR. The position of our galaxies in the MS, (Figure 7 and 8) supports a picture in which the dust within star-forming galaxies evolves as those galaxies evolve and transform their morphologies.

5.3 Comparisons with other AGN indicators

In this Section we compare our fitted f_{AGN} and other CIGALE-derived AGN-related parameters to widely used AGN indicators.

5.3.1 IRAS 60/25 μm and Neon emission-line ratios

The IRAS 60 μm to 25 μm flux ratio f_{60}/f_{25} is an indicator of hot dust content (Wu et al. 2011), and thus suggestive of the strength of the AGN relative to ongoing star formation because dust in the AGN torus is on average hotter than in star formation regions. In combination with mid-infrared emission-line ratios, f_{60}/f_{25} can be quite effective at separating AGNs from starbursts (Tommasin et al. 2008; Veilleux et al. 2009; Tommasin et al. 2010). In the top panel of Fig. 9 the f_{60}/f_{25} ratio is plotted as a function of the [Ne v]/[Ne II] integrated intensity ratio for our galaxies. There is a clear separation

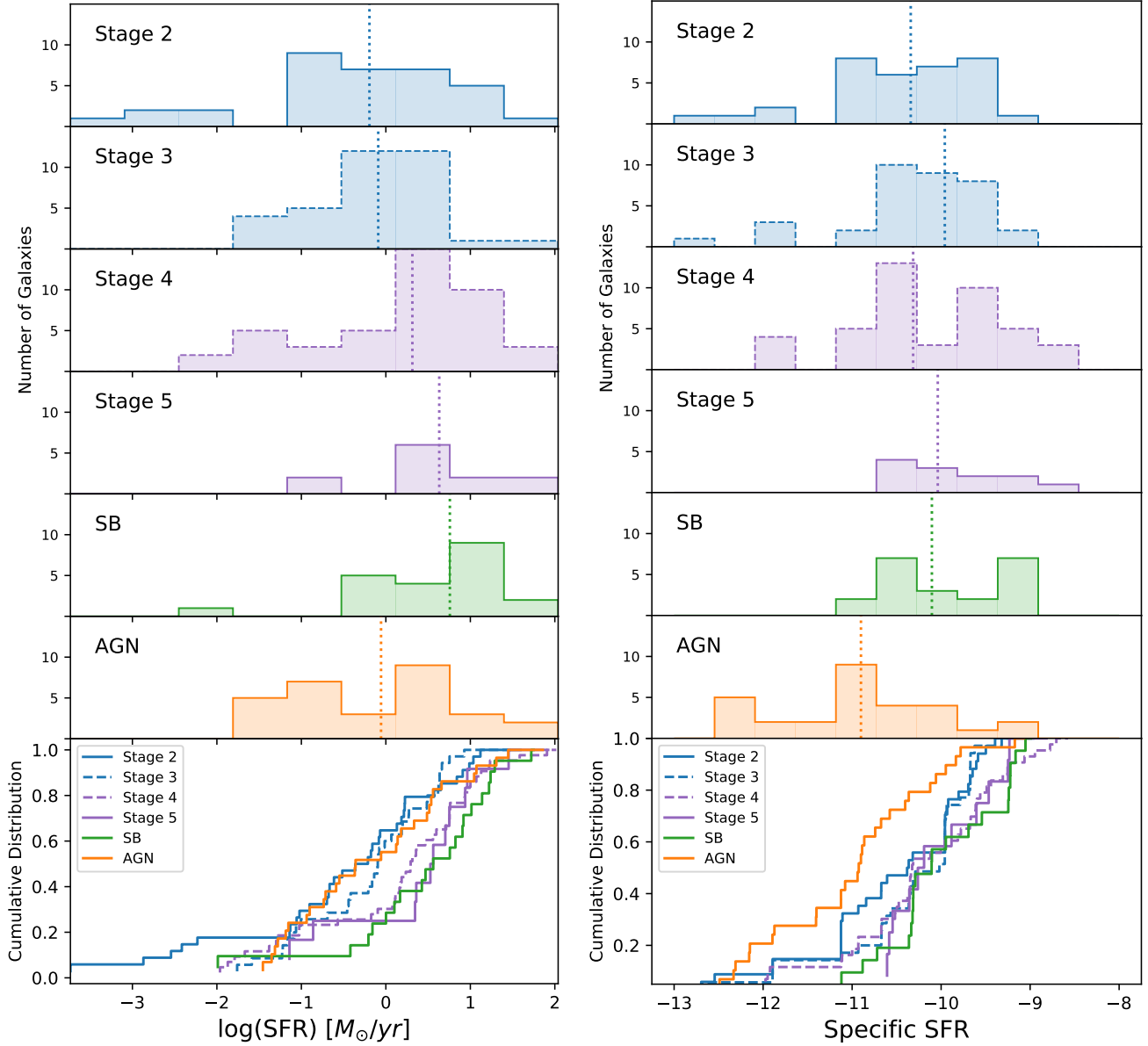


Figure 6. Histograms (top) for the stages of the combined SIGS+LSM sample and the normalized cumulative distributions (bottom) of SFR (*Left panel*) and sSFR (*Right panel*). In the histograms we present the stage 2 (blue), 3 (dashed blue), 4 (dashed purple) and 5 (purple) from the SIGS+LSM sample, and the SB (green) and AGN (orange) samples. The respective median value is represented in the histograms by dotted vertical lines. In the cumulative distributions we present all the previous samples.

between star formation-dominated galaxies ($[\text{Ne v}]/[\text{Ne II}] \lesssim 0.7$, $f_{60}/f_{25} \gtrsim 3$) and AGNs, in agreement with Tommasin et al. (2010) and Higuera-G. & Ramos P. (2013). The result, together with Fig. 4, supports the common assumption that the shape of the mid-IR continuum of galaxies with significant emission from AGNs can be approximated by a power-law and thus that the continuum in this region is a good discriminator between galaxies with and without strong AGN emission (Brandl et al. 2006; Tommasin et al. 2008; Dixon & Joseph 2011). Veilleux et al. (2009, figures 24-26) found a similar relationship with the analogous $[\text{O IV}]/[\text{Ne II}]$ ratio and less dramatically with the $[\text{Ne v}]/[\text{Ne II}]$ ratio. They find a progression of these line ratios from low to high starting with star-forming galaxies, followed by Seyferts 2, Seyferts 1, ULIRGs, and finally QSOs.

The SIGS sample unfortunately only possesses a few pub-

lished measurements or upper limits for these lines. Most of them have $[\text{Ne v}]/[\text{Ne II}] \lesssim 0.1$ and $f_{\text{AGN}} < 0.2$. We would expect the interacting systems in the SIGS sample to have a different fraction of AGN emission as they move from early on in the interaction towards the coalescence phase, to fall in between the two regimes of $[\text{Ne v}]/[\text{Ne II}]$ ratio presented here.

We observe that those SIGS galaxies for which we were able to collect line emission and that are not upper limits, do fall in between the SB and the AGN galaxies, with intermediate cases. The AGN galaxies with the highest *IRAS* ratio (cooler dust) are NGC 3281, ESO428-14, NGC 4941, NGC 4388 and NGC 7674, and the SB with the most elevated $[\text{Ne v}]/[\text{Ne II}]$ are NGC 2623, NGC 1365, NGC 4088, NGC 4194 and NGC 4676. There is one upper limit

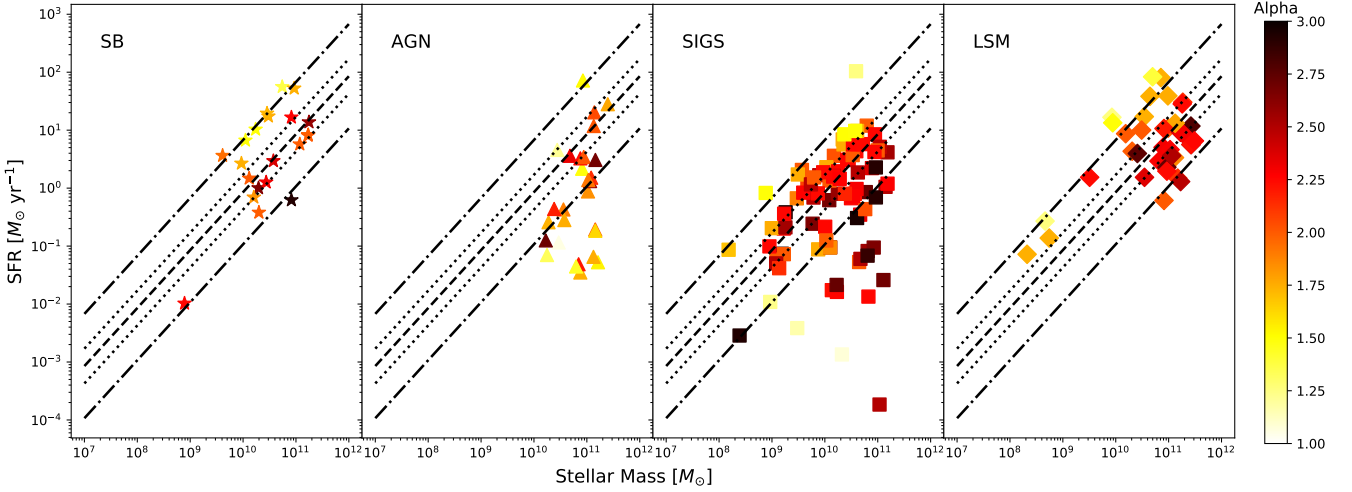


Figure 7. SFR as a function of stellar mass with selected galaxies color-coded by the derived parameter α (Dale et al. 2014) obtained from CIGALE. The dashed, dotted, and dashed-dotted lines in every panel indicate respectively the $z = 0$ MS and the 0.3 and 0.9 dex limits above and below it. We compare the SB (left panel), AGN (middle-left panel), SIGS (middle-right panel) and LSM samples (right panel). All the SB galaxies follow the MS and the gradient of α seems to agree with Martínez-Galarza et al. (2016) with the parameter C , as we discuss in Section 5.2. As expected, the AGN sample galaxies do not follow the MS, and no trend with α is evident. The SIGS sample shows a large scatter across the MS and some SIGS galaxies appear in the region where SF is quenched.

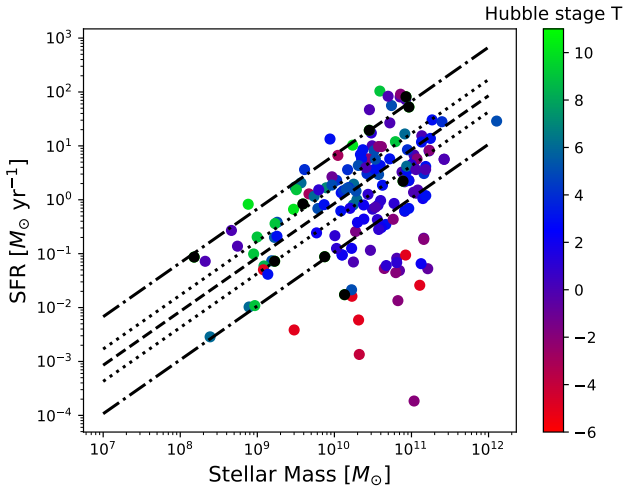


Figure 8. Main sequence of star-forming galaxies showing the galaxies in this work, but color-coded by Hubble stage (T). Peculiar galaxies outside of range of colors shown for T in the color bar are plotted in black. The dashed lines are identical to those in Figure 7. Early types (elliptical and lenticular galaxies; $T < 0$) tend to have low SFRs while the spirals follow the MS. Irregular galaxies scatter over in several order of magnitude in SFR for a given stellar mass.

published for a LSM galaxy (2MASXJ10591815+2432343, with $[\text{Ne v}]/[\text{Ne II}] < 0.02$), so we do not include that galaxy in Fig. 9.

5.3.2 Comparing galaxy parameters with their emission line ratios

The fine structure Ne-lines can help us discriminate between the SB and AGN samples as well as with the SIGS galaxies because they flag the presence of an AGN even in galaxies otherwise classified

as a star-forming (Abel & Satyapal 2008). One of the most useful outputs of CIGALE is the fraction of AGN derived from the SED (Sect. 4.1). The bottom panel of Figure 9 offers confirmation of the CIGALE estimated AGN contributions, compared with other estimations not using SED from Veilleux et al. (2009, table 12) and Díaz-Santos et al. (2017, table 2, column 7). We can see that the AGN sample and SB sample separate very well in Figure 9. However, the estimated AGN fraction can in some cases have a value near to 40% in the SB sample galaxies (NGC 1365 and NGC 660). In the same way, three AGN galaxies have a AGN fraction below 0.3 (NGC 4941, NGC 7674 and NGC 4388).

Most of the SIGS sample galaxies have weak or no AGN contributions (Lanz et al. 2013). A particular outlier of this behaviour is NGC 3034, with the highest $f_{\text{AGN}} = 0.48 \pm 0.03$ in the sample but yet a very low $[\text{Ne v}]/[\text{Ne II}]$. Lanz et al. (2013) show that this galaxy was very difficult to fit with MAGPHYS (da Cunha et al. 2008), possibly due to the high obscuration, the presence of an outflow, or some other unaccounted for activity. We were also unable to obtain a good fit with CIGALE except when we include the AGN component model; in that case our reduced- χ^2 was 3.29, which is low enough to be considered a reliable fit. Therefore, even when strong star formation is present, f_{AGN} estimates with CIGALE could reveal a hidden AGN, that is invisible in optical wavelengths. This estimate can only be checked by the emission spectra of high IP lines like $[\text{Ne v}]$.

5.3.3 Infrared color diagnostics

Infrared colors are well-known diagnostics of the energy sources powering infrared-luminous galaxies; two salient examples are the color-color diagrams developed by Stern et al. (2005) and Lacy et al. (2004) to discriminate between galaxies dominated by star formation and AGN emission. More strict criteria can be applied (e.g. Donley et al. 2012), but they depend on other factors, as luminosity. We can use our more precise AGN and SFR measurements to test the reliability of these diagrams. Fig. 10 shows *Spitzer*/IRAC and

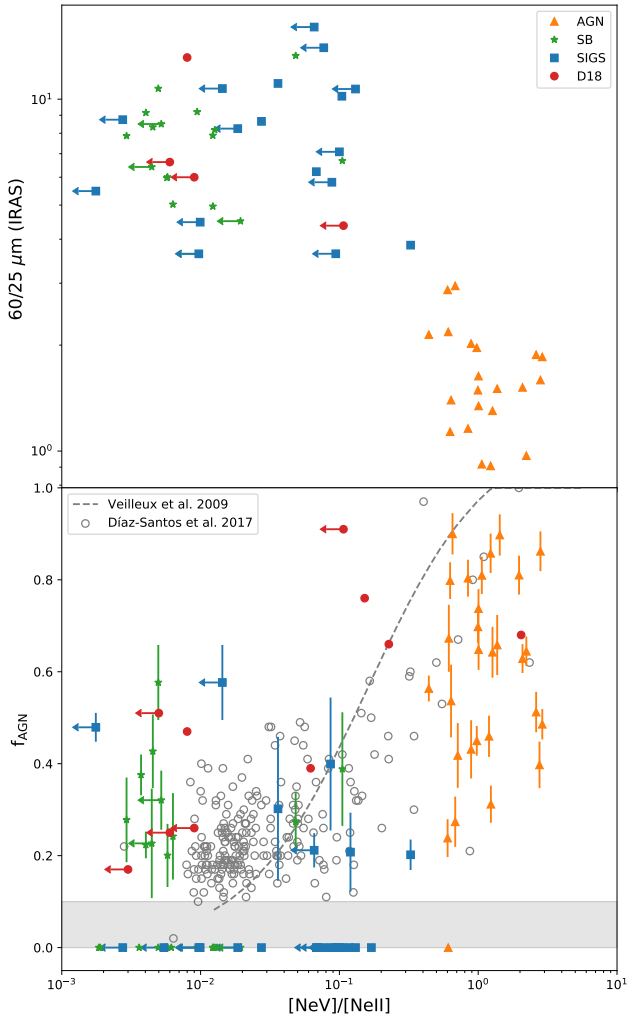


Figure 9. *Top panel:* The ratio of integrated IRAS flux densities at 60 and 25 μm f_{60}/f_{25} as a function of the $[\text{Ne v}]/[\text{Ne II}]$ integrated line intensity ratio. The symbols are the same as in Figure 5 with the addition of values from D18. Upper limits are indicated with arrows. *Bottom panel:* Total AGN fraction as a function of the $[\text{Ne v}]/[\text{Ne II}]$ integrated line intensity ratios. The markers are the same as in the top panel, with the errorbars on f_{AGN} indicating the uncertainty estimates taken from CIGALE. We added the estimations from Veilleux et al. (2009) (dashed line) and Díaz-Santos et al. (2017) (empty gray circles) to compare with literature results. The grey region indicates where the f_{AGN} estimates are not believed to be reliable; we treat objects in this region as if they have $f_{\text{AGN}} = 0$. In both panels the SB and AGN samples are well-separated. The SIGS galaxies tend not to have significant AGN contributions.

WISE color-color diagrams for our galaxies. Galaxies that lie within the wedge enclosed by the dotted lines in left panel are expected to be AGN-dominated. Only five of the 29 galaxies from our AGN sample (ESO428-14, NGC 3516, NGC 4941, NGC 4388, IC5063) lie outside the wedge. This is not unexpected: Petric et al. (2011) find that faint AGNs with measurable PAH 6.2 μm EW fall outside the wedge.

AGN- and star formation-dominated galaxies are also efficiently segregated in a complementary *WISE* color-color diagram (Fig. 10, right panel). All but three of our AGN sample galaxies lie in the AGN selection region described by Blecha et al. (2018); two

of the outliers are located close to the boundary. However, some SB populate the AGN wedge in this plot. We include the late-stage mergers from (D18) in Fig. 10. Many of the (D18) late-stage mergers have weak or undetected AGNs; they appear to populate both the AGN- and star formation-dominated regions of both panels of Fig. 10.

Stern et al. (2012) proposed that *WISE* $W1 - W2 \geq 0.7$ colour is a robust indicator of AGN emission. The majority (22) of our 29 AGN sample galaxies meet this criterion. A less conservative $W1 - W2 \geq 0.5$ colour cut (Ashby et al. 2009) is similar to the lower boundary of the wedge in the left panel of Fig. 10, and is identical to that shown in the right panel. The two AGN galaxies which fail to satisfy the less stringent criterion are ESO 428-14 and NGC 4388. Our most-likely CIGALE models for them yield total AGN fractions of $f_{\text{AGN}} = 0.31 \pm 0.04$ and 0.24 ± 0.04 respectively, which are significant although not large enough to make them AGN-dominated, and help indicate the reliability limits of these diagrams.

NGC 4941 is the only AGN having a blue $W1 - W2$ colour comparable to those of the SIGS galaxies, with $f_{\text{AGN}} < 20\%$ yet also possessing a high $[\text{Ne v}]/[\text{Ne II}]$ ratio (Sec. 5.3.1). Its blue mid-IR color and high Ne line ratio is consistent with NGC 4941 being a heavily absorbed low-luminosity AGN (Kawamuro et al. 2013) and illustrates how the $[\text{Ne v}]$ emission can help identify the AGN contribution in highly obscured cases. Overall, we confirm that mid-IR color diagnostics in general do identify AGNs, and with f_{AGN} we quantify their contribution to the total galaxy output.

Some of the SB and SIGS galaxies lie close to the AGN wedge in the right-hand panel of Fig. 10. We decided to test whether their location in Fig. 10 could be interpreted straightforwardly to mean that they are composite objects hosting significant AGN and star formation but not necessarily dominated by either. We examined galaxies having intermediate *WISE* colours $W1 - W2 > 0.3$. This included five SIGS galaxies (NGC 838, NGC 839, NGC 3034, NGC 3227 and NGC 3690) and eight SB galaxies (NGC 660, NGC 1222, NGC 1365, NGC 1614, NGC 2146, NGC 2623, NGC 3256 and NGC 4194).

We consider the SIGS galaxies first. For NGC 838 and 839 the most likely CIGALE fits give $f_{\text{AGN}} \sim 0.0$ for both galaxies. B15 classify NGC 839 as a low-ionization nuclear emission-line region (LINER, e.g., Kewley et al. 2006). The most likely f_{AGN} estimate for NGC 3690 is 0.0, but D18 notice different classification for this galaxy, as LINER, AGN and star-forming. The optical spectroscopic classifications (Pereira-Santaella et al. 2010) for NGC 3034 and 3227 are HII and Seyfert 1, these galaxies have an SED that is consistent with an AGN contribution of $f_{\text{AGN}} = 0.48 \pm 0.03$ and 0.20 ± 0.03 , respectively.

Next we consider the SB galaxies. For NGC 660 we estimated $f_{\text{AGN}} = 0.43 \pm 0.08$. This object is usually classified as star-forming (Petric et al. 2011; Wu et al. 2011), and there are also signs of interaction. NGC 1365 has one of the highest $[\text{Ne v}]/[\text{Ne II}]$ ratios in the SB sample. Its calculated f_{AGN} estimate is 0.39. Hernán-Caballero et al. (2015) obtained 0.6. NGC 1614 has $f_{\text{AGN}}=0.0$; Hernán-Caballero et al. (2015) obtained 0.3. This object is classified as an “uncertain AGN” by Asmus et al. (2014). NGC 1222, NGC 2146 and NGC 3256 have $f_{\text{AGN}} \sim 0.0, 0.37$ and 0.0, respectively. Finally, NGC 4194 has a high ratio of $[\text{Ne v}]/[\text{Ne II}]$ and seems to be undergoing a merger, but the CIGALE results show a $f_{\text{AGN}} = 0.0$, consistent with there being no AGN contribution. It is nonetheless classified as a Seyfert 2 galaxy (Pereira-Santaella et al. 2010).

Lastly, for NGC 2623 the $[\text{Ne v}]/[\text{Ne II}]$ ratio is among the highest in the SB sample (see Sect. 2.4), with $f_{\text{AGN}} = 0.27 \pm 0.06$.

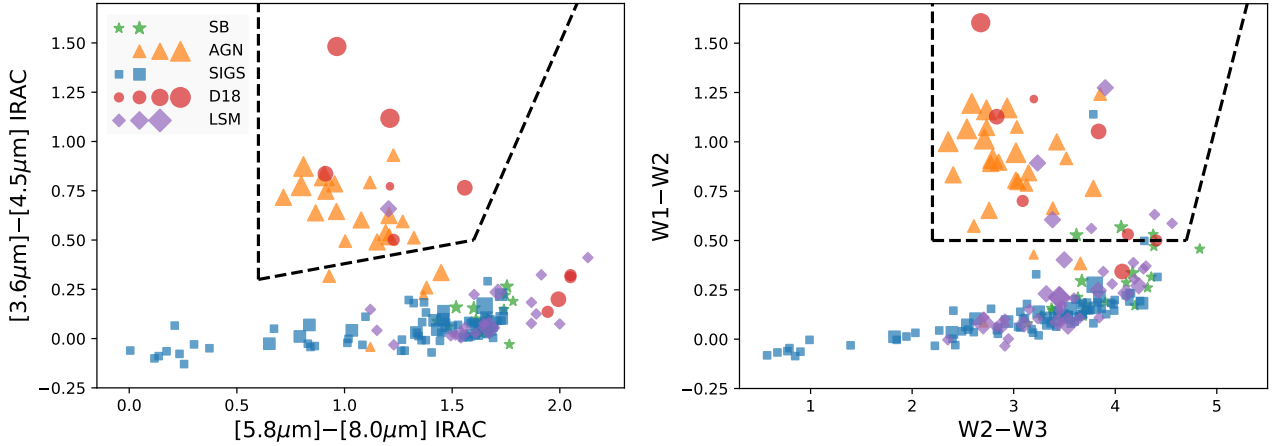


Figure 10. Mid-infrared color-color classification diagrams showing the SIGS (blue squares), SB (green stars), LSM (purple diamonds) and AGN (orange triangles) galaxies together with late-stage mergers (red circles) from D18. The markers sizes are divided in four ranges for the $f_{\text{AGN}} < 0.25, 0.25-0.5, 0.5-0.75$ and > 0.75 , where not all the samples cover the four ranges. *Left panel:* $[5.8\mu\text{m}] - [8.0\mu\text{m}]$ vs. $[3.6\mu\text{m}] - [4.5\mu\text{m}]$ color-color diagram following Stern et al. (2005) for all sample galaxies with available IRAC photometry. Sources in the region enclosed by the dashed lines (commonly referred to as the Stern wedge) are dominated by AGN emission in the mid-infrared, while sources below this region are dominated by star-formation. *Right panel:* $W2 - W3$ vs. $W1 - W2$ color-color diagram, with an AGN wedge (dashed lines) per Blecha et al. (2018). Most late-stage mergers and AGN fall in this wedge with some galaxies from the SIGS and SB sample. The separation of these wedges with the f_{AGN} is in agreement with the expected behaviour of AGN activity onset.

Unfortunately, we obtained a relatively poor fit to the SED of this source, so our CIGALE model for it may be unreliable. It has been classified as starburst (e.g. Wu et al. 2011), composite (Asmus et al. 2014) and AGN (e.g. Hernán-Caballero et al. 2015) where a fraction of AGN of 0.44 is obtained, comparable to the AGN fraction of 0.39 ± 0.05 from D18. These are intermediate cases in which both an AGN presence and also intense star-formation are underway, and color alone is insufficient to categorize the source unambiguously.

The last sample we examine in Figure 10 is the LSM. Twelve galaxies are above the cut at $W1 - W2 > 0.3$ and six of them with values of $W1 - W2 > 0.5$. Galaxies 2MASX J01221811+0100262 and 2MASX J08434495+3549421 have the highest f_{AGN} of the LSM sample, 0.42 ± 0.10 and 0.48 ± 0.10 respectively. The former was found to be a tentative dual AGN with mixed signs of star-formation by Satyapal et al. (2017). The latter is classified as Seyfert 2 by Véron-Cetty & Véron (2010). The rest of the galaxies have values for f_{AGN} below $\lesssim 0.25$.

In summary, these five SIGS and eight SB galaxies that lie close to the AGN wedge in Fig. 10 appear to be composite systems, and the LSM systems inside the wedge are classified as AGN as one would expect: the CIGALE models indicate varying fractional contributions of AGNs to their emission, but in none of them there is a dominant AGN that was somehow ‘missed’ by the color-color diagram. We can identify systems like the ones presented here, which do have AGN contribution, but not large enough to make the Stern cut, and quantify the amount of the contribution in terms of f_{AGN} . Likewise, our SED analysis is consistent with the implications of the canonical infrared color-color diagnostic diagrams.

5.3.4 sSFR and stellar mass estimates in light of prior results

B15 and Lanz et al. (2013) use the MAGPHYS SED fitting code (a version that did not include an AGN component) plus DECOMPIR (Mullaney et al. 2011) to characterize the SIGS galaxies. In Fig. 11 we compare our results with those from B15, focusing on the stellar mass and specific star formation rate, parameters only indirectly influenced by the presence of an AGN.

The left panel of Fig. 11 shows that our stellar mass estimates agree on average with those from B15, but with a large scatter. No obvious dependence on the total AGN fraction is apparent, which can be related to the selected sample. SED models with AGN and without AGN reproduce similar stellar masses and specific star formation rates, although objects with high AGN fraction show a small trend for being outliers in stellar mass. IC 694 is a conspicuous outlier because of aperture issues (Sec. 3.4). Even more scatter is observed in the comparison for derived sSFR (right panel of Fig. 11), especially below $\log(\text{sSFR}) = -11.5$, where the accuracy of SED-based methods in measuring the sSFR significantly decreases (Eales et al. 2017). The coarse CIGALE input parameter grid below $\log(\text{sSFR}) = -11.5$ produces the entirely artificial grouping of galaxies along discrete sSFR values. NGC 4933A, NGC 5353 and NGC 5481 are not shown because their estimated sSFRs fall in an extremely low, likely unreliable, sSFR regime ($< 10^{-13}$).

6 DISCUSSION

In this Section we discuss the implications of the SED modeling for star formation and AGN emission in interacting galaxies.

6.1 Interaction Stage

B15 note that almost all their galaxies with $\log(\text{sSFR}) < -11.0$ are at early interaction stages. Morphologically disturbed systems lie along a broad range of sSFRs, with the range occupied by stage 4 galaxies extending to higher sSFRs than the earlier stages (Fig. 6). Our results are equivocal with respect to stage 4 systems and sSFR, however, because the KS tests applied in Sec. 5.1 do not provide compelling evidence, even with our enlarged sample, that stage 4 systems differ significantly from stage 2 or 3 systems (Table 3). However, the outcome is different for the stage 5 systems. They differ significantly in the aggregate from the AGN sample, marginally from the stage 2 and 3 systems (7% and 14% chance of being drawn from the same parent sample, respectively), and there is no

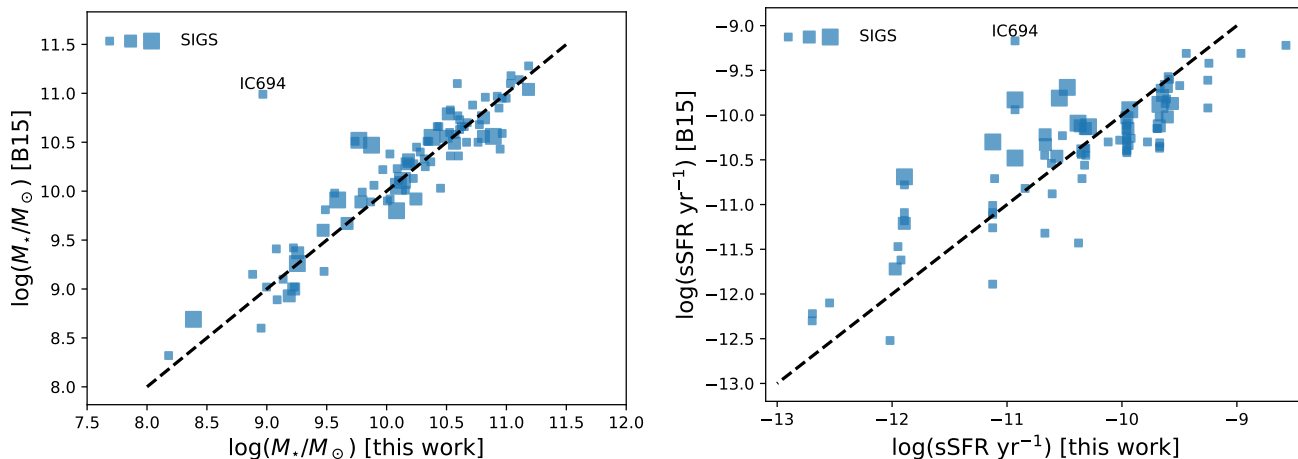


Figure 11. Stellar mass (*Left panel*) and specific star formation rate (*Right panel*) estimates derived in this work compared to those obtained with MAGPHYS by B15 for the SIGS galaxies. Symbol sizes indicate the total AGN contributions f_{AGN} : the smallest symbols indicate an AGN contribution below 20%, the intermediate symbols indicate an AGN contribution between 20 and 30%, and the largest symbols indicate an AGN contribution above 30%. The line of equality is indicated with the dashed line in both panels. The stellar masses are in good overall agreement, with large scatter. The sSFR estimates also show approximate overall agreement, but also with significant scatter, especially below $\log(\text{sSFR}) = -11.5$.

evidence that they differ from the starburst systems. Collectively, the evidence thus favors a picture in which sSFRs are greatest in stage 5 systems, i.e., in or approaching coalescence. This is in agreement with hydrodynamical simulations (Hayward et al. 2014; Martínez-Galarza et al. 2016), which show a steep increase of the SFR very close to coalescence (more for massive systems).

As discussed in Sect. 5.1, Lanz et al. (2013) did not find statistically significant correlations between SED shape, merger stage, and star-forming properties. In the present work we have enlarged the study sample and the available photometry, and analyzed these data with CIGALE, i.e., a code that explicitly accounts for AGN emission. With these enhancements, we observe that f_{AGN} does show a correlation with luminosity (see Sect. 6.4). Our results also point to a weak correlation between f_{AGN} and interaction stages, with a larger fraction of late stage mergers showing a higher f_{AGN} . SED analysis can therefore be used to infer the physical conditions associated with different stages.

6.2 The Schmidt-Kennicutt Relation

Star-forming galaxies form a relatively narrow distribution in the two-dimensional parameter space defined by total stellar mass and SFR, commonly known as the star-forming main sequence (MS). This scaling relation has been widely used to study the relationship between galaxy morphology, star formation, and SED shapes (e.g., Elbaz et al. 2011). However, the SFR is not a directly measured quantity, as it is indirectly derived from different observables; total stellar mass estimations, although generally robust, also suffer from being model-dependent. As an example, the vast majority of papers discussing the MS rely on a version of Schmidt-Kennicutt (S-K) relation to infer SFRs from the infrared luminosity of galaxies, that is first converted to a dust mass, and then, via a gas to dust ratio, to a gas mass. In this sub-section we re-examine the reliability of that relation for LIRGs. For the analysis, we rely on parameters derived from our full CIGALE modeling of the SEDs.

In order to estimate the obscured SFR, the $8\ \mu\text{m}$ or $24\ \mu\text{m}$ luminosities are often used (see Lanz et al. 2013, for a more detailed discussion), but when possible, it is convenient to use the integrated

infrared luminosity between $5\text{--}1000\ \mu\text{m}$, which is related to the thermal emission from dust heated by star formation (at wavelengths shorter than about $5\ \mu\text{m}$ the SED is dominated by emission from stellar photospheres rather than dust heated by star formation). The Schmidt-Kennicutt relation, often formulated as the relationship between gas surface density and SFR, can also be formulated as a relationship between the total SFR and the infrared luminosity (Lanz et al. 2013). This has been a very useful SFR diagnostic ever since the infrared was first made accessible by the *IRAS* and *ISO* satellites. With panchromatic datasets now at hand, incorporating photometry from *Spitzer*, *WISE*, *AKARI*, and *Herschel*, there is room for considerable improvement.

An important caveat in this conventional approach is that the infrared emission is often interpreted as originating from thermal emission from dust heated only by star formation. However, other heating mechanisms are often in place and need to be accounted for, such as AGN activity and older stellar populations. (Hopkins et al. 2010; Lanz et al. 2013; Wilson et al. 2019). Although for most star-forming galaxies this additional contribution is small or negligible, in some cases it can be significant or even dominate the infrared luminosity of the entire galaxy. For the galaxies included in this work, which by construction emphasize infrared-luminous systems and mergers at various stages, we show that the AGN alone can contribute up to $\sim 80\%$ of the infrared luminosity for these systems.

Figure 12 plots derived SFR as a function of dust luminosity for all galaxies in Tables A1–A4, color-coded by the estimated f_{AGN} . We observe that for dust luminosities above roughly $10^{10.5}\ L_{\odot}$, the S-K diagnostic provides a good measure of the amount of star formation taking place. In particular, the fact that at those luminosities there is so little scatter at all levels of f_{AGN} indicates that our approximation correctly accounts for other sources of dust heating, allowing a better estimation of the SFR. At lower luminosities we observe a significant scatter in the SFR at a given luminosity. This indicates that the S-K diagnostic might not provide a reliable measure of the SFR at these lower dust luminosities. A plausible explanation for this is that low dust luminosities also implies a larger relative amount of unobscured star formation that is not accounted

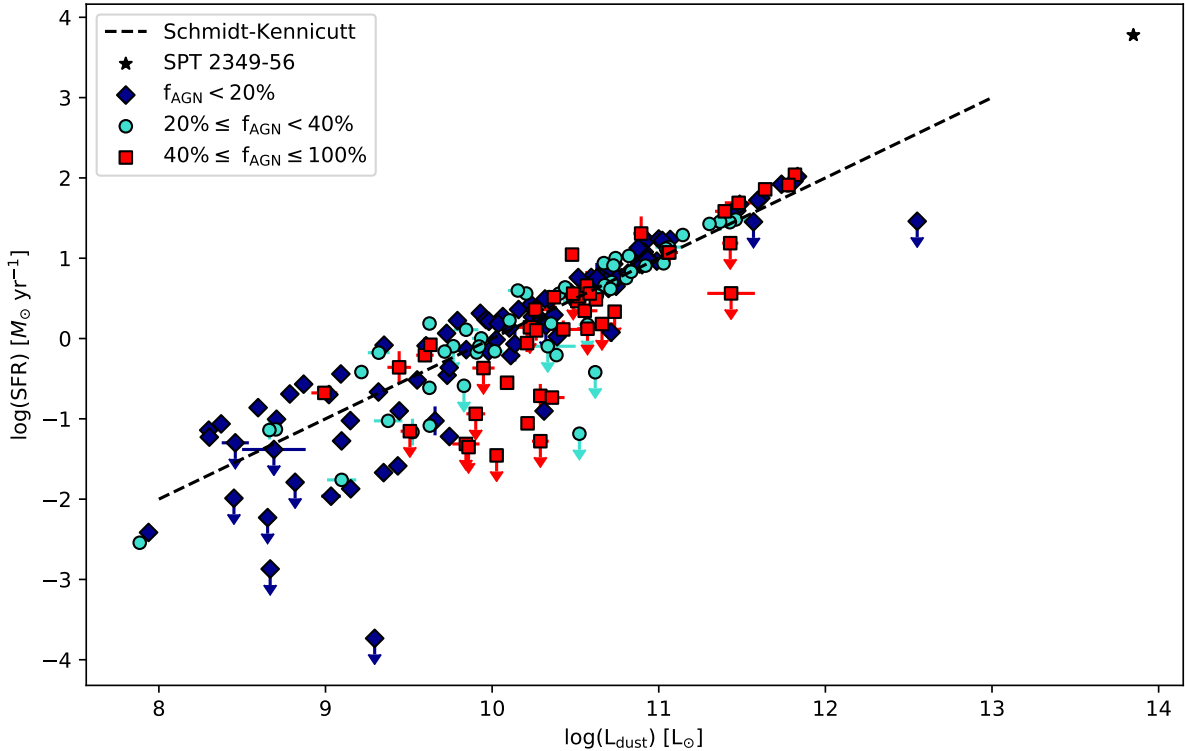


Figure 12. Total derived SFR as a function of total dust luminosity for all galaxies modeled in this work. Red squares, cyan circles, and blue diamonds respectively indicate galaxies with total AGN fraction $> 40\%$, in the range $20\text{--}40\%$, and below 20% . The dashed line is the S-K relation. Also plotted for comparison is an IR-luminous cluster SPT2349–56 at $z = 4.6$ (black star, Miller et al. 2018). Arrows indicate the galaxies for which the SFR are only estimated to within a factor of roughly two (see Table A10).

for by the infrared diagnostics. Less luminous, less morphologically disturbed systems are less optically thick to UV radiation, and therefore a pan-chromatic approach such as the one we have adopted here is more likely to provide reliable estimates.

Figure 12 also indicates that galaxies that are less luminous in the infrared have a broader range of AGN contributions skewed towards smaller contributions, i.e., very few galaxies with infrared luminosities below $10^9 L_{\odot}$ have $f_{\text{AGN}} > 20\%$. This supports an scenario in which significant AGN emission occurs preferentially in highly disturbed/obscured systems, and is in agreement with hydrodynamical simulations. Finally, our results are also consistent with a wider dynamical range of SFR at lower luminosities, in absolute terms. At low luminosities, star formation can range from being a negligible to being a significant factor in the galaxy evolution, but at high infrared luminosities, the dust heating from SFR and AGN completely dominates the galactic evolution. This also has to do with the timescales of this evolution. Luminous systems are morphologically disturbed with starburst-like, short-term episodes of star formation and AGN accretion, whereas low luminous systems evolve more secularly, impacting the range of possible fractional SFR contributions.

6.3 The Galaxy Main-Sequence: New Subtleties and Issues

In Fig. 13 we plot the CIGALE-derived stellar masses and SFRs for our galaxies, together with the location of the MS as derived by Elbaz et al. (2011) for comparison. Several interesting inferences follow from the way our sample galaxies populate this two-dimensional space. First, only a minority of galaxies are located on

the nominal MS locus. Some lie above it, in the zone associated by Elbaz et al. (2011) with starburst-like star formation, whereas a significant amount lie below it, even by a few orders of magnitude. At high stellar masses, the majority of those systems above the MS have higher AGN contributions, which indicates that not only the SFR per unit stellar mass is enhanced, but also the AGN activity.

What is more puzzling is the significant amount of systems that we observe below the MS. Significant divergences from the MS have been reported both in observations of high redshift galaxies within protoclusters, due to environmental quenching (e.g. Zavala et al. 2019), and in cosmological simulations that relate the growth of galactic halos to that of stellar mass, in which the MS scatter depends on the timescale of star formation variability (e.g. Hahn et al. 2019).

In our case, the large scatter is probably due to the way we assembled our sample. We have selected preferentially galaxies that are luminous and that are morphologically disturbed through mergers. In some of these cases, it is impossible to tell from the morphology alone whether the system has undergone coalescence, and it is likely that in some of those systems star formation has been suppressed due to negative feedback from the AGN, after coalescence. This interpretation is consistent is supported by the results shown in Figure 8, with early type galaxies showing significantly lower SFRs. Our sample is therefore not representative of the secular stages of star formation in galaxies. Instead it represents systems with enhanced star formation through the effect of mergers, and systems where AGN feedback has probably quenched star formation. The fact that both high and low f_{AGN} values are similarly represented below the MS indicates that quenching takes place very rapidly

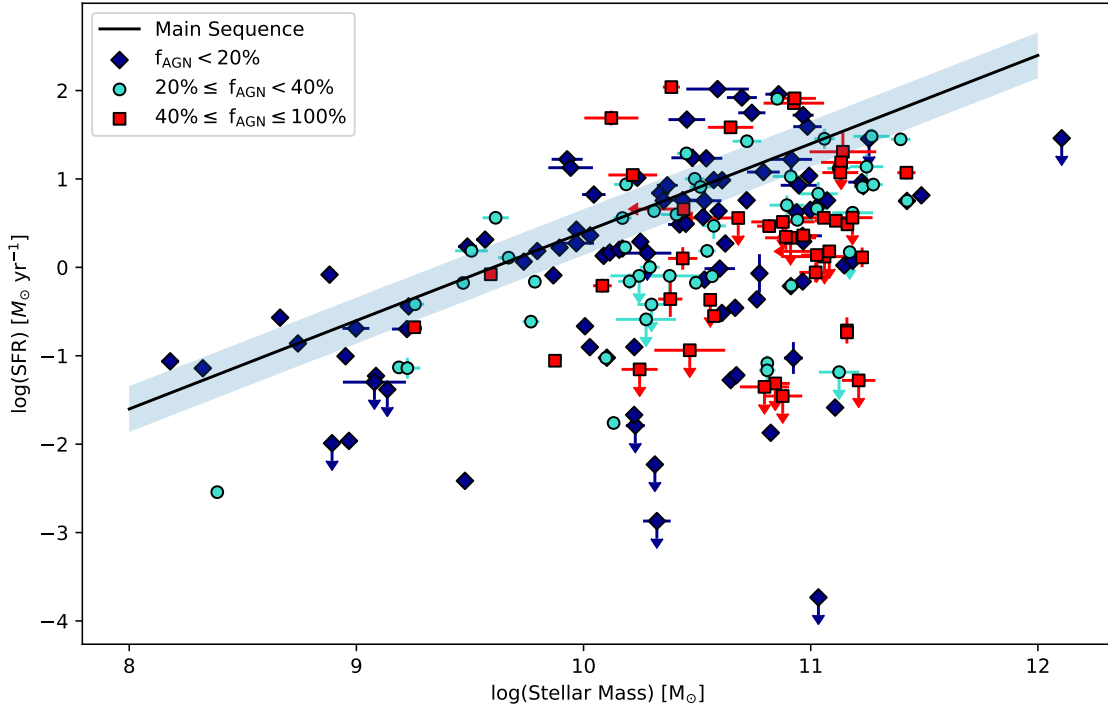


Figure 13. Integrated derived SFR as a function of total stellar mass populated with all galaxies modeled in this work. Red squares, cyan circles, and blue diamonds respectively indicate galaxies with total AGN fraction $> 40\%$, in the range $20\text{--}40\%$, and below 20% . The star forming main sequence per [Elbaz et al. \(2011\)](#) is indicated with the black line; the shaded region extends to ± 0.26 dex about it. Values of SFR below -1 in the log are relatively uncertain. Arrows indicate the galaxies for which the SFR or stellar masses are only estimated to within a factor of roughly two (see [Table A10](#))

after the onset of the AGN. In an upcoming paper ([Della Costa et al. in prep.](#)), we discuss this latter conclusion in more detail.

In [Fig. 14](#) we compare the stellar mass to the total infrared luminosity from dust heated by stars and AGN in the left panel and to the AGN luminosity only in the right panel. We note that out of a total of 188 galaxies, 42 galaxies have $f_{\text{AGN}} \geq 40\%$ whereas 51 of them have $f_{\text{AGN}} \geq 20\%$. We observe a mild correlation between stellar mass and luminosity for systems with low contribution from AGN. Presumably, in these systems the infrared luminosity is dominated by star formation, and the correlation confirms that more massive systems tend to have more dust heating, but not always and there are wide variations. A similar correlation is found for systems with a significant contribution from the AGN, but notably the scatter is much smaller. For galaxies with AGN, we also observe a correlation that implies that most luminous AGNs tend to live in the most massive galaxies regardless of the fraction of total luminosity that the AGN contributes, as long as it is above 20% . The apparent scatter for systems above $10^{10} M_{\odot}$ is most likely due to larger uncertainties in the determination of stellar masses for these systems. In the context of galaxy assembly, this positive correlation supports a joint evolution of super massive black holes and their hosts.

[Fig. 15](#) shows the correlation between SFR and AGN luminosity for those systems with $f_{\text{AGN}} > 20\%$. We observe that systems with intermediate AGN contributions (cyan dots) show a tight correlation in this plane over 5 orders of magnitude in SFR. For systems with high AGN contributions (red dots), we observe a similar correlation, but there is a larger scatter, and also, the luminosity of the AGN at a given SFR is higher in comparison with the intermediate systems. Similar correlations between AGN luminosity and SFR have been found in more uniform samples, such as the COSMOS

field ([Lanzuisi et al. 2017](#)); such correlations support scenarios proposed in recent galaxy evolution models in which black hole accretion and star formation are correlated due to the compression of large amounts of gas in nuclear regions.

The fact that the correlation is less tight at higher AGN contributions, at evolutionary stages closer to coalescence, can be interpreted in terms of star formation quenching: as hydrodynamical simulations show, the AGN reaches a peak in luminosity right after coalescence, and star formation gets quenched very rapidly. This supports a real effect of AGN feedback on SFR, as opposed to recent studies ([Harrison et al. 2019](#)) that suggest that AGN activity does not quench galaxy wide AGN. One possible explanation of this discrepancy could be the difference between galaxy-wide star formation and the nuclear, merger-induced star formation that we are measuring in the present work.

6.4 The AGN as crucial ingredient in galaxy evolution

We have shown (e.g., [Figs. 13-15](#) and related discussions), that accounting for the AGN emission is a necessary step in order to gain a better understanding of the physics and energy budget of infrared-luminous galaxies, specially in the late stage of mergers. In particular, we have provided evidence that dust heating by the AGN can be a dominant factor in the galaxy SED, and that the latter can provide hints as to the specific stage of the merger. We have also shown that the rapid evolution of AGN accretion an SFR right before and right after coalescence creates significant spread in the so-called Main Sequence, partly due to star formation quenching. This conclusion echoes that by earlier works (e.g., [Alonso-Herrero et al.](#)

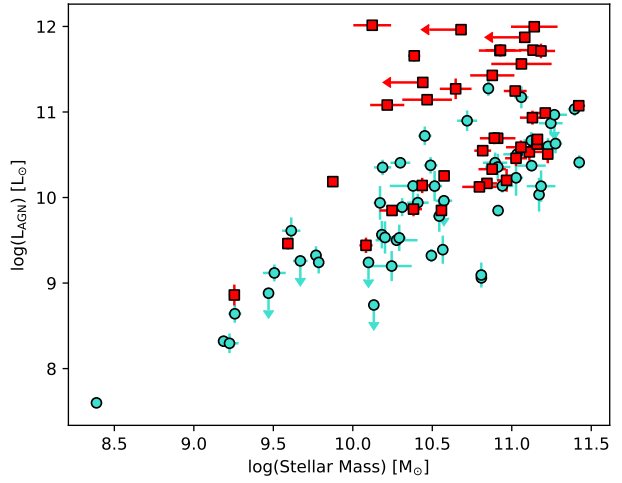
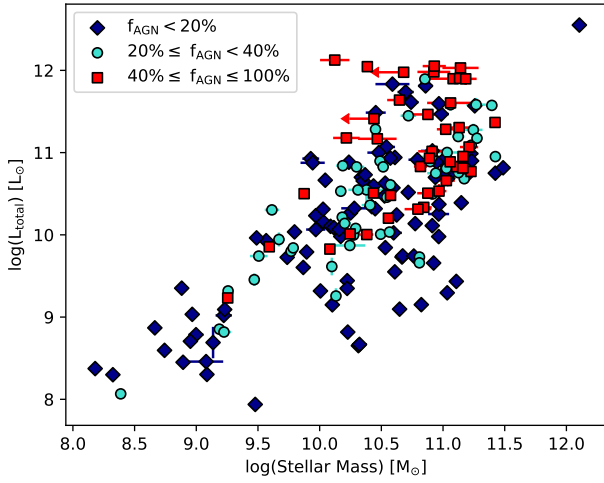


Figure 14. Left panel: The total dust luminosity as a function of stellar mass. Note that sources with a CIGALE-estimated AGN fraction below 20% are recalculated and plotted here assuming its AGN contribution is zero. Right panel: The AGN luminosity only as a function of stellar mass. Arrows indicate the galaxies for which the luminosities or stellar masses are only estimated to within a factor of roughly two (see Table A10)

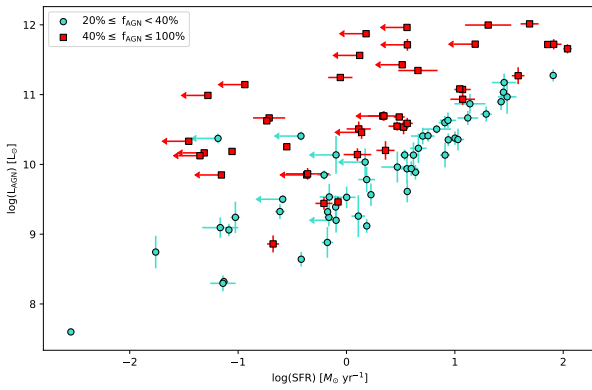


Figure 15. Total AGN luminosity as a function of SFR. Red squares indicate objects with $f_{\text{AGN}} > 40\%$, whereas cyan dots indicate those with f_{AGN} in the range of 20–40%. Arrows indicate the galaxies for which the luminosities or SFR are only estimated to within a factor of roughly two (see Table A10)

2012; Hayward et al. 2014). Here we elucidate some implications of these findings.

Alonso-Herrero et al. (2012) suggest that the prevalence of galaxies with $f_{\text{AGN}} > 0.05$ correlates with IR luminosity, increasing from $f_{\text{AGN}} \sim 0.3$ for $10^{11}L_{\odot} < L_{\text{IR}} < 10^{12}L_{\odot}$ to $f_{\text{AGN}} \gtrsim 0.5$ in $L_{\text{IR}} > 10^{12}L_{\odot}$. Our Figure 5 points to a similar trend. They also found that the AGN contribution is close to 50% for LIRGs, and that it reaches 80% in the case of ULIRGs. Our results are consistent with those numbers, with galaxies in the AGN sample reaching the highest values of fractional AGN contribution. We also see an increase in the fractional AGN contribution for bins of increasing luminosity. For bins centered at 10^9 , 10^{10} , 10^{11} , 10^{12} in L_{IR} , the respective means in f_{AGN} values are 5%, 14%, 20% and 36%. Similar results were found by Dai et al. (2018) in a larger sample of U(LIRGS) with a measured AGN contribution. Including the AGN contribution in the SED analysis of luminous infrared galaxies is therefore a required step in any reliable study of their physical properties.

There are a number of diagnostics that can be better interpreted if a reliable determination of the merger or AGN onset stages can be

made from SED analysis, as we are doing in this work. For example, Tommasin et al. (2010) notice that if the AGN ionising continuum is switched off, the photoionized narrow line region (NLR) could still be detected due to its large extension and long line recombination time (~ 300 yr, depending on the density). They also suspect that this delay might be related to the existence of many different types of AGNs as classified by their line emission properties. Our work provides a sample that can be used as a proxy to study how line emission properties change as a function of AGN fractional contribution and amount of star formation quenching. A combination of f_{AGN} estimations in addition to fine structure lines ratios (as Fig. 9) can lead to a reliable analysis of AGN stages and their relation with interacting galaxies, as with the $f_{\text{AGN}} - [\text{Ne V}]/[\text{Ne II}]$ plane. We have confirmed that line ratios are a more reliable proxy for AGN presence than the SED analysis alone.

Funneling of large amounts of gas into the nuclear regions during a merger can trigger large episodes of star-formation and AGNs activity (Weaver et al. 2010; Lanzuisi et al. 2017). The resulting obscuration can significantly attenuate the AGN optical emission (Blecha et al. 2018). Our results support a co-evolution of star formation and AGN activity during a merger, while correcting by obscuration effects by using a pan-chromatic, energy-conserving approach.

In their study of post-starbursts, Alatalo et al. (2017) find that, well before coalescence, merging galaxies are generally located in the “green valley” and show bluer $W1 - W2$ *WISE* colours, characteristic of AGN activity (see also our Fig. 10). These galaxies thus may contain buried AGNs that emit in the infrared and are better traced by infrared emission lines (see Figure 9). They suggest that the AGNs do not radiatively dominate the post-starburst phase, and that a better census of these post-starbursts can be constructed if there are reliable tracers of the AGN activity during the early phases of quenching. Our work provides an example of such search, and the fact that we see a significant number of less luminous AGNs below the main sequence in Fig. 7 agrees with their results.

The need for more extensive samples and better indicators of the interaction stage specially during the obscured and morphologically disturbed phase is critical for an improved understanding of the evolution of mergers. Our work provides a pilot study of what

JWST and the SPace IR Telescope for Cosmology and Astrophysics (SPICA) (Spinoglio et al. 2017) will be able to do with their improved sensitivity and spectral resolution.

7 CONCLUSIONS

We have re-reduced and re-analysed photometric observations from the UV to the FIR on 199 luminous and ultra-luminous galaxies in four different sets of objects including mergers and AGN, analyzed their physical properties using the CIGALE SED modeling code, and presented an analysis of the results. This is the largest systematic, wide, multi-band SED analysis program yet done on an ULIRG sample. In particular, our approach included galaxies over a broad range of AGN activity as reported in the literature. Our goal was to accurately measure the fractional AGN contribution to the total luminosity in these systems, and to assess how this contribution impacts popularly used SED diagnostics of star formation and ISM properties. We also aimed at examining the evolving effects of AGN activity across the merger sequence. From the original sample, we excluded ten objects that either had limited or uncertain datasets and/or unreliable SEDs. Our primary conclusions apply to the remaining 189 objects. Here are our major findings:

1. A reliable measure of the fractional contribution of AGN emission to the total luminosity of galaxies is essential in the understanding of galaxy-wide physics, such as star formation evolution and total energy output. About half of the galaxies in our sample have more than 20% AGN contribution to their total luminosities, and about a quarter of the systems had contributions over 40%. This results in warmer dust temperatures that can be wrongly associated to star formation if AGN is not included in the modelling. Overall, we find only a weak correlation between the merger stage and the AGN fractional contribution, in agreement with other studies (Lanz et al. 2013, e.g.,).

2. AGN activity can be responsible for a significant displacement of galaxies across the so-called "Main Sequence" of star formation. Outliers of this correlation must therefore be interpreted in terms of their AGN activity, and not only in terms of their star formation properties. We have produced a carefully remeasured SFR- M_* plane that shows significant deviations from the MS correlation, both above and below it. These deviations are only partially explained by increased star formation, as increased AGN activity and feedback-driven star formation quenching can have a significant role in the emission properties, specially at merger stages just before and just after coalescence.

3. As a result of the previous statement, infrared galaxies at intermediate and high redshifts should not have their physical properties, specially those related to star formation, interpreted as if they were local MS infrared galaxies, without first accounting for their merger stage and AGN fractional contribution. Possible diagnostics to do this from their SED and spectra include their location in the $f_{\text{AGN}} - [\text{Ne v}]/[\text{Ne II}]$ plane.

4. At high (>40%) fractional AGN contributions, both the star formation luminosity and the AGN luminosity independently correlate with the total stellar mass of the galaxy. This is in agreement with findings in large uniform surveys such as COSMOS, and supports scenarios in which both black hole accretion and star formation are driven by gas compression in the nuclear regions during the merger. The lack of correlation between the total luminosity and the stellar mass at low AGN fractional contributions calls into question the use of infrared diagnostics alone to estimate SFR in the early stages of mergers.

5. The SFR- M_* plane for our 189 luminous galaxies reveals significant outliers from the Main Sequence, specially among systems larger than about $10^{10}M_*$. In particular, many systems in late stages of the merger fall up to a few orders of magnitude below the MS. This suggests that the MS paradigm stops being valid for luminous merging systems near to coalescence, due to the rapid quenching of star formation by the AGN feedback. This is in agreement with recent evidence of quenching in intermediate redshift galaxies affecting the MS, and implies that the MS paradigm needs to be evaluated carefully for samples without a thorough SED analysis that includes AGN emission. A similar study with a much larger sample of galaxies might be more conclusive in this respect.

6. Our sample is significantly larger than many other studies and (we argue) the SED method is more accurate; using it we support and refine earlier conclusions that f_{AGN} correlates with L_{IR} , with the average AGN contribution to a galaxy's L_{IR} increasing from about 5% to 36% as L_{IR} increases from 10^9 to $10^{12}L_{\odot}$.

CIGALE was in many cases able to identify Type 1 AGNs by varying the viewing angle Ψ and looking for a minimum χ^2 value (and other parameters changes); Type 1's had optimum fits with $\psi \gtrsim 70$. This feature may be of particular value in studies of high- z objects whose morphology is unknown but whose line strengths cannot be properly analyzed without attention to the possible extinction corrections. A new version of CIGALE has recently been released which we plan to use in a more detailed analysis of viewing angle effects.

In the near future, planned and proposed facilities such as JWST and SPICA, and ground-based telescopes, will provide better resolution and new insights into the physical processes at work in galaxies and their evolution. In particular, they will begin to piece together the cosmic history of galaxies in the universe. The method of meticulous SED modelling, as presented in this work, can play an important role in the interpretation of these new datasets.

ACKNOWLEDGEMENTS

The authors gratefully thank Steve Willner, Andreas Zezas, Lingyu Wang, Elizabeth Hora, Madison Hora, John Della Costa III, and Antonio Frigo for their assistance and advice. They particularly thank Denis Burgarella and Laura Ciesla from the CIGALE team for their expert guidance and assistance. We acknowledge the anonymous referee for a careful reading of the manuscript and very helpful questions and comments. HAS, MA, and JRM-G acknowledge partial support from NASA Grants NNX14AJ61G and NNX15AE56G.

The SAO REU program is funded by the National Science Foundation REU and Department of Defense ASSURE programs under NSF Grant AST-1659473, and by the Smithsonian Institution.

This publication makes use of data products from the Two Micron All Sky Survey, which is a joint project of the University of Massachusetts and the Infrared Processing and Analysis Center/California Institute of Technology, funded by the National Aeronautics and Space Administration and the National Science Foundation.

This research is based on observations made with the Galaxy Evolution Explorer, obtained from the MAST data archive at the Space Telescope Science Institute, which is operated by the Association of Universities for Research in Astronomy, Inc., under NASA contract NAS 5-26555.

Funding for SDSS-III has been provided by the Alfred P. Sloan Foundation, the Participating Institutions, the National Science Foundation, and the U.S. Department of Energy Office of Science.

The SDSS-III web site is <http://www.sdss3.org/>. SDSS-III is managed by the Astrophysical Research Consortium for the Participating Institutions of the SDSS-III Collaboration including the University of Arizona, the Brazilian Participation Group, Brookhaven National Laboratory, Carnegie Mellon University, University of Florida, the French Participation Group, the German Participation Group, Harvard University, the Instituto de Astrofísica de Canarias, the Michigan State/Notre Dame/JINA Participation Group, Johns Hopkins University, Lawrence Berkeley National Laboratory, Max Planck Institute for Astrophysics, Max Planck Institute for Extraterrestrial Physics, New Mexico State University, New York University, Ohio State University, Pennsylvania State University, University of Portsmouth, Princeton University, the Spanish Participation Group, University of Tokyo, University of Utah, Vanderbilt University, University of Virginia, University of Washington, and Yale University.

This work is based in part on observations made with the *Spitzer Space Telescope*, which is operated by the Jet Propulsion Laboratory, California Institute of Technology under a contract with NASA. This publication makes use of data products from the *Wide-field Infrared Survey Explorer*, which is a joint project of the University of California, Los Angeles, and the Jet Propulsion Laboratory/California Institute of Technology, funded by the National Aeronautics and Space Administration." Herschel is an ESA space observatory with science instruments provided by European-led Principal Investigator consortia and with important participation from NASA.

This research has also made use of results from NASA's Astrophysics Data System. This research has made use of the NASA/IPAC Extragalactic Database (NED), which is operated by the Jet Propulsion Laboratory, California Institute of Technology, under contract with the National Aeronautics and Space Administration. This research has made use of the SIMBAD database, operated at CDS, Strasbourg, France. This research made use of Astropy, a community-developed core Python package for Astronomy ([Astropy Collaboration et al. 2013](#)). We thank the people that support photutils ([Bradley et al. 2018](#)).

DATA AVAILABILITY

The data underlying this article are available in the article and in its online supplementary material.

REFERENCES

- Abel N. P., Satyapal S., 2008, *ApJ*, **678**, 686
- Alatalo K., et al., 2017, *ApJ*, **843**, 9
- Alonso-Herrero A., Pereira-Santaella M., Rieke G. H., Rigopoulou D., 2012, *ApJ*, **744**, 2
- Amblard A., Riguccini L., Temi P., Im S., Fanelli M., Serra P., 2014, *ApJ*, **783**, 135
- Ashby M. L. N., et al., 2009, *ApJ*, **701**, 428
- Asmus D., Hönig S. F., Gandhi P., Smette A., Duschl W. J., 2014, *MNRAS*, **439**, 1648
- Astropy Collaboration et al., 2013, *A&A*, **558**, A33
- Bernard-Salas J., et al., 2009, *ApJS*, **184**, 230
- Bertin E., Arnouts S., 1996, *A&AS*, **117**, 393
- Bitsakis T., Charmandaris V., da Cunha E., Díaz-Santos T., Le Floch E., Magdis G., 2011, *A&A*, **533**, A142
- Blecha L., Snyder G. F., Satyapal S., Ellison S. L., 2018, *MNRAS*, **478**, 3056
- Boissay R., Ricci C., Paltani S., 2016, *A&A*, **588**, A70
- Boquien M., Burgarella D., Roehly Y., Buat V., Ciesla L., Corre D., Inoue A. K., Salas H., 2019, *A&A*, **622**, A103
- Boselli A., et al., 2014, *A&A*, **570**, A69
- Bradley L., et al., 2018, astropy/photutils: v0.5, doi:10.5281/zenodo.1340699, <https://doi.org/10.5281/zenodo.1340699>
- Brandl B. R., et al., 2006, *ApJ*, **653**, 1129
- Brandl B. R., Martín-Hernández N. L., Schaerer D., Rosenberg M., van der Werf P. P., 2012, *A&A*, **543**, A61
- Brassington N. J., Zezas A., Ashby M. L. N., Lanz L., Smith H. A., Willner S. P., Klein C., 2015, *ApJS*, **218**, 6
- Brinchmann J., Charlot S., White S. D. M., Tremonti C., Kauffmann G., Heckman T., Brinkmann J., 2004, *MNRAS*, **351**, 1151
- Bruzual G., Charlot S., 2003, *MNRAS*, **344**, 1000
- Burgarella D., Buat V., Iglesias-Páramo J., 2005, *MNRAS*, **360**, 1413
- Calzetti D., Armus L., Bohlin R. C., Kinney A. L., Koornneef J., Storchi-Bergmann T., 2000, *ApJ*, **533**, 682
- Ciesla L., et al., 2014, *A&A*, **565**, A128
- Ciesla L., et al., 2015, *A&A*, **576**, A10
- Clark C. J. R., et al., 2018, *A&A*, **609**, A37
- Cohen M., Megeath S. T., Hammersley P. L., Martín-Luis F., Stauffer J., 2003a, *AJ*, **125**, 2645
- Cohen M., Wheaton W. A., Megeath S. T., 2003b, *AJ*, **126**, 1090
- Dai Y. S., Wilkes B. J., Bergeron J., Kuraszewicz J., Omont A., Atanas A., Teplitz H. I., 2018, *MNRAS*, **478**, 4238
- Dale D. A., et al., 2005, *ApJ*, **633**, 857
- Dale D. A., Helou G., Magdis G. E., Armus L., Díaz-Santos T., Shi Y., 2014, *ApJ*, **784**, 83
- Dasyra K. M., Ho L. C., Netzer H., Combes F., Trakhtenbrot B., Sturm E., Armus L., Elbaz D., 2011, *ApJ*, **740**, 94
- Díaz-Santos T., et al., 2017, *ApJ*, **846**, 32
- Dietrich J., et al., 2018, *MNRAS*, **480**, 3562
- Dixon T. G., Joseph R. D., 2011, *ApJ*, **740**, 99
- Doi M., et al., 2010, *AJ*, **139**, 1628
- Donley J. L., et al., 2012, *ApJ*, **748**, 142
- Dopita M. A., Pereira M., Kewley L. J., Capaccioli M., 2002, *ApJS*, **143**, 47
- Eales S., de Vis P., Smith M. W. L., Appah K., Ciesla L., Duffield C., Schofield S., 2017, *MNRAS*, **465**, 3125
- Elbaz D., et al., 2011, *A&A*, **533**, A119
- Engelbracht C. W., et al., 2007, *PASP*, **119**, 994
- Fazio G. G., et al., 2004, *ApJS*, **154**, 10
- Fritz J., Franceschini A., Hatziminaoglou E., 2006, *MNRAS*, **366**, 767
- Genzel R., et al., 1998, *ApJ*, **498**, 579
- Goulding A. D., Alexander D. M., 2009, *MNRAS*, **398**, 1165
- Griffin M. J., et al., 2010, *A&A*, **518**, L3
- Groves B., Dopita M. A., Sutherland R. S., Kewley L. J., Fischera J., Leitherer C., Brandl B., van Breugel W., 2008, *ApJS*, **176**, 438
- Gruppioni C., et al., 2016, *MNRAS*, **458**, 4297
- Guillard P., et al., 2012, *ApJ*, **747**, 95
- Gunn J. E., et al., 1998, *AJ*, **116**, 3040
- Gunn J. E., et al., 2006, *AJ*, **131**, 2332
- Hahn C., et al., 2019, *ApJ*, **872**, 160
- Harrison C. M., Alexander D. M., Rosario D. J., Scholtz J., Stanley F., 2019, arXiv e-prints, p. arXiv:1912.01020
- Hayward C. C., et al., 2014, *MNRAS*, **445**, 1598
- Hernán-Caballero A., et al., 2015, *ApJ*, **803**, 109
- Higuera-G. M. A., Ramos P. A. F., 2013, *Rev. Mex. Astron. Astrofís.*, **49**, 301
- Higuera-G. M. A., Rodríguez-Ardila A., Tejero J. M., 2009, *Star Formation Analysis in Active Galactic Nuclei, Starburst, Ultraluminous Infrared, and Quasar Objects*. p. 72
- Hopkins P. F., Hernquist L., Cox T. J., Di Matteo T., Robertson B., Springel V., 2006, *ApJS*, **163**, 1
- Hopkins P. F., Younger J. D., Hayward C. C., Narayanan D., Hernquist L., 2010, *MNRAS*, **402**, 1693
- Houck J. R., et al., 2004, *ApJS*, **154**, 18
- Ishibashi W., Fabian A. C., 2016, *MNRAS*, **463**, 1291

- Johnson K. E., Hibbard J. E., Gallagher S. C., Charlton J. C., Hornschemeier A. E., Jarrett T. H., Reines A. E., 2007, *AJ*, 134, 1522
- Kauffmann G., et al., 2003, *MNRAS*, 341, 54
- Kawamuro T., Ueda Y., Tazaki F., Terashima Y., 2013, *ApJ*, 770, 157
- Keel W. C., Kennicutt R. C. J., Hummel E., van der Hulst J. M., 1985, *AJ*, 90, 708
- Keremedjiev M., Hao L., Charmandaris V., 2009, *ApJ*, 690, 1105
- Kewley L. J., Groves B., Kauffmann G., Heckman T., 2006, *MNRAS*, 372, 961
- Lacy M., et al., 2004, *ApJS*, 154, 166
- Lanz L., et al., 2013, *ApJ*, 768, 90
- Lanz L., Hayward C. C., Zezas A., Smith H. A., Ashby M. L. N., Brassington N., Fazio G. G., Hernquist L., 2014, *ApJ*, 785, 39
- Lanzuisi G., et al., 2017, *A&A*, 602, A123
- Leitherer C., Li I. H., Calzetti D., Heckman T. M., 2002, *ApJS*, 140, 303
- Lintott C. J., et al., 2008, *MNRAS*, 389, 1179
- Lintott C., et al., 2011, *MNRAS*, 410, 166
- Martin D. C., et al., 2005, *ApJ*, 619, L1
- Martínez-Galarza J. R., et al., 2016, *ApJ*, 817, 76
- Matthee J., Schaye J., 2019, *MNRAS*, 484, 915
- Miller T. B., et al., 2018, *Nature*, 556, 469
- Morrissey P., et al., 2007, *ApJS*, 173, 682
- Mullaney J. R., Alexander D. M., Goulding A. D., Hickox R. C., 2011, *MNRAS*, 414, 1082
- Müller-Sánchez F., González-Martín O., Fernández-Ontiveros J. A., Acosta-Pulido J. A., Prieto M. A., 2010, *ApJ*, 716, 1166
- Narayanan D., et al., 2010, *MNRAS*, 407, 1701
- Neugebauer G., et al., 1984, *ApJ*, 278, L1
- Noll S., Burgarella D., Giovannoli E., Buat V., Marcellac D., Muñoz-Mateos J. C., 2009, *A&A*, 507, 1793
- Pearson W. J., et al., 2019, *A&A*, 631, A51
- Pereira-Santaella M., Diamond-Stanic A. M., Alonso-Herrero A., Rieke G. H., 2010, *ApJ*, 725, 2270
- Petric A. O., et al., 2011, *ApJ*, 730, 28
- Planck Collaboration et al., 2016, *A&A*, 594, A13
- Poglitsch A., et al., 2010, *A&A*, 518, L2
- Renzini A., Peng Y.-j., 2015, *ApJ*, 801, L29
- Rieke G. H., et al., 2004, *ApJS*, 154, 25
- Sanders D. B., Mirabel I. F., 1996, *ARA&A*, 34, 749
- Satyapal S., et al., 2017, *ApJ*, 848, 126
- Serra P., Amblard A., Temi P., Burgarella D., Giovannoli E., Buat V., Noll S., Im S., 2011, *ApJ*, 740, 22
- Silva A., et al., 2018, *ApJ*, 868, 46
- Skrutskie M. F., et al., 2006, *AJ*, 131, 1163
- Smith J. D. T., et al., 2007a, *PASP*, 119, 1133
- Smith J. D. T., et al., 2007b, *ApJ*, 656, 770
- Somerville R. S., Davé R., 2015, *ARA&A*, 53, 51
- Speagle J. S., Steinhardt C. L., Capak P. L., Silverman J. D., 2014, *ApJS*, 214, 15
- Spinoglio L., et al., 2017, *Publ. Astron. Soc. Australia*, 34, e057
- Stern D., et al., 2005, *ApJ*, 631, 163
- Stern D., et al., 2012, *ApJ*, 753, 30
- Stierwalt S., et al., 2013, *ApJS*, 206, 1
- Sturm E., Lutz D., Verma A., Netzer H., Sternberg A., Moorwood A. F. M., Oliva E., Genzel R., 2002, *A&A*, 393, 821
- Su S., Kong X., Li J., Fang G., 2013, *ApJ*, 778, 10
- Swinyard B. M., et al., 2010, *A&A*, 518, L4
- Tommasin S., Spinoglio L., Malkan M. A., Smith H., González-Alfonso E., Charmandaris V., 2008, *ApJ*, 676, 836
- Tommasin S., Spinoglio L., Malkan M. A., Fazio G., 2010, *ApJ*, 709, 1257
- Vaddi S., O'Dea C. P., Baum S. A., Whitmore S., Ahmed R., Pierce K., Leary S., 2016, *ApJ*, 818, 182
- Veilleux S., et al., 2009, *ApJS*, 182, 628
- Véron-Cetty M. P., Véron P., 2010, *A&A*, 518, A10
- Wang L., Rowan-Robinson M., Norberg P., Heinis S., Han J., 2014, *MNRAS*, 442, 2739
- Weaver K. A., et al., 2010, *ApJ*, 716, 1151
- Wenger M., et al., 2000, *A&AS*, 143, 9
- Wilson C. D., Elmegreen B. G., Bemis A., Brunetti N., 2019, *ApJ*, 882, 5
- Wright E. L., et al., 2010, *AJ*, 140, 1868
- Wu Y.-Z., Zhao Y.-H., Meng X.-M., 2011, *ApJS*, 195, 17
- Yang G., et al., 2020, *MNRAS*, 491, 740
- York D. G., et al., 2000, *AJ*, 120, 1579
- Yun M. S., Reddy N. A., Condon J. J., 2001, *ApJ*, 554, 803
- Zavala J. A., et al., 2019, *ApJ*, 887, 183
- Zucker C., Walker L. M., Johnson K., Gallagher S., Alatalo K., Tzanavaris P., 2016, *ApJ*, 821, 113
- da Cunha E., Charlot S., Elbaz D., 2008, *MNRAS*, 388, 1595
- de Vaucouleurs G., 1977, in Tinsley B. M., Larson Richard B., Gehret D. C., eds, *Evolution of Galaxies and Stellar Populations*. p. 43
- de Vaucouleurs G., de Vaucouleurs A., Corwin Herold G. J., Buta R. J., Paturel G., Fouque P., 1991, *Third Reference Catalogue of Bright Galaxies*

APPENDIX A: EXTRA MATERIAL

Here we present all the information for the samples, photometry values, line emissions, examples of the CIGALE SED fitting, CIGALE derived parameters and histograms of the parameters analysed for all the 188 galaxies presented in this work. We include a table with the derived parameters for six AGN galaxies where a different viewing angle in CIGALE give different output parameters. In addition, as online material, we provide the SED fits of the 178 galaxies with good fits. For the remaining 10 galaxies where the SED fit is not good enough, we provide the AGN and no-AGN SED fits.

Table A1. Basic data for the SIGS sample galaxies.

Group ID	Galaxy ID	RA (J2000)	Dec	Redshift (z)	Sample	Interaction Stage	Size (" × ")	Angle ^a (°)
1	NGC 274 ^b	00:51:01.6	-07:03:22.7	0.0058	A	4	33.8 × 23.0	130.0
	NGC 275	00:51:04.8	-07:03:59.8	0.0058	A	4	38.2 × 28.1	25.0
2	NGC 470	01:19:44.9	03:24:35.6	0.0079	A	2	90.0 × 55.1	65.0
	NGC 474	01:20:06.7	03:24:55.4	0.0077	A	2	225.0 × 175.0	165.0
3	NGC 520	01:24:35.1	03:47:32.7	0.0076	A	5	147.3 × 97.2	235.0
4	IC 195 ^b	02:03:44.6	14:42:33.5	0.0122	A	3	37.8 × 21.2	39.8
	IC 196	02:03:49.8	14:44:20.8	0.0122	A	3	95.0 × 55.1	62.0
5	NGC 833	02:09:20.8	-10:07:59.2	0.0129	A	4	42.5 × 23.0	175.0
	NGC 835	02:09:24.6	-10:08:09.2	0.0136	A	4	42.8 × 35.3	125.0
	NGC 838	02:09:38.5	-10:08:48.1	0.0128	A	3	45.0 × 25.9	175.0
	NGC 839	02:09:42.9	-10:11:02.8	0.0129	A	2	45.0 × 28.0	5.0
6	NGC 935	02:28:10.6	19:36:05.4	0.0138	A	4	53.6 × 33.1	65.0
	IC 1801	02:28:12.7	19:34:59.9	0.0134	A	4	34.2 × 19.1	120.0
7	NGC 1241	03:11:14.6	-08:55:19.6	0.0135	A	3	100.1 × 60.1	50.0
	NGC 1242	03:11:19.3	-08:54:08.6	0.0134	A	3	28.1 × 19.4	44.4
8	NGC 1253	03:14:09.0	-02:49:22.4	0.0057	A	3	168.1 × 52.6	175.0
	NGC 1253A	03:14:23.3	-02:48:02.9	0.0061	A	3	55.1 × 20.2	5.0
9	NGC 2276	07:27:28.3	85:45:23.8	0.0081	C	2	85.0 × 72.0	110.0
10	NGC 2444	07:46:53.2	39:02:05.3	0.0135	A	4	54.4 × 30.6	125.0
	NGC 2445	07:46:55.1	39:00:41.8	0.0133	A	4	52.2 × 45.4	110.0
11	NGC 2633	08:48:04.6	74:05:56.0	0.0072	C	2	79.9 × 50.0	90.0
	NGC 2634 ^b	08:48:25.4	73:58:01.9	0.0075	C	2	40.7 × 35.3	135.0
	NGC 2634A	08:48:38.1	73:56:21.5	0.007	C	2	38.2 × 18.0	155.0
12	NGC 2719A	09:00:15.5	35:43:09.5	0.0104	A	2	22.0 × 15.1	35.0
	NGC 2719	09:00:15.6	35:43:41.9	0.0103	A	2	40.0 × 13.0	40.0
13	NGC 2805	09:20:20.4	64:06:10.1	0.0058	C	2	165.0 × 140.0	120.0
	NGC 2814	09:21:11.5	64:15:11.5	0.0053	C	2	50.0 × 20.2	90.0
14	NGC 2820A	09:21:29.8	64:14:14.6	0.0051	C	3	15.5 × 11.2	110.0
	NGC 2820	09:21:45.6	64:15:28.4	0.0053	C	3	119.9 × 20.2	151.0
15	NGC 2964	09:42:54.2	31:50:50.6	0.0044	C	2	78.5 × 41.0	8.0
	NGC 2968 ^b	09:43:12.0	31:55:43.3	0.0052	C	2	71.3 × 54.4	145.0
	NGC 2970	09:43:31.1	31:58:37.2	0.0054	C	2	24.8 × 24.8	0.0
16	NGC 2976	09:47:15.5	67:54:59.0	0.0008	C	2	209.2 × 84.6	50.6
17	NGC 3031	09:55:33.2	69:03:55.1	0.0008	C	2	834.8 × 420.1	75.0
	NGC 3034	09:55:52.7	69:40:45.8	0.0007	C	2	285.1 × 159.8	155.0
	NGC 3077	10:03:19.1	68:44:02.0	0.0009	C	2	143.6 × 110.0	135.0
18	NGC 3165	10:13:31.3	03:22:30.0	0.0045	C	3	70.9 × 30.2	78.5
	NGC 3166	10:13:45.8	03:25:30.0	0.0045	C	3	141.1 × 68.8	175.0
	NGC 3169	10:14:15.0	03:27:58.0	0.0041	C	2	150.1 × 110.2	145.0
19	NGC 3185	10:17:38.6	21:41:17.9	0.0041	C	2	79.9 × 55.1	35.0
	NGC 3187	10:17:47.9	21:52:23.9	0.0053	C	3	90.0 × 40.0	170.0
	NGC 3190	10:18:05.6	21:49:56.3	0.0042	C	3	141.8 × 50.0	32.0
20	NGC 3226	10:23:27.0	19:53:54.6	0.0044	C	4	56.9 × 44.6	110.0
	NGC 3227	10:23:30.6	19:51:54.0	0.0039	C	4	95.0 × 60.1	55.0
21	NGC 3395	10:49:49.3	32:58:45.5	0.0054	C	4	55.1 × 32.0	120.0
	NGC 3396	10:49:55.6	32:59:24.7	0.0054	C	4	63.0 × 29.9	10.0
22	NGC 3424	10:51:46.3	32:54:02.9	0.005	C	2	93.6 × 28.8	20.0
	NGC 3430	10:52:11.4	32:57:01.4	0.0053	C	2	119.2 × 69.1	115.0
23	UGC 6016 ^b	10:54:14.6	54:17:11.8	0.005	A	3	74.9 × 47.9	150.0
	NGC 3448	10:54:38.6	54:18:22.3	0.0045	A	3	84.6 × 40.3	155.0
24	IC 694	11:28:27.3	58:34:42.6	0.0132	C	4	11.9 × 11.9	0.0
	NGC 3690	11:28:32.3	58:33:42.8	0.0104	C	4	65.9 × 47.2	35.0
25	NGC 3786	11:39:42.7	31:54:27.7	0.0089	C	3	62.3 × 33.5	170.0
	NGC 3788	11:39:44.6	31:55:52.3	0.009	C	3	58.0 × 25.9	85.0
26	NGC 3799	11:40:09.4	15:19:38.3	0.011	A	3	25.2 × 18.4	14.2
	NGC 3800	11:40:13.5	15:20:32.6	0.011	A	3	61.2 × 24.5	142.0
27	IC 749	11:58:34.1	42:44:02.4	0.0027	C	2	79.9 × 65.2	65.0
	IC 750	11:58:52.2	42:43:21.0	0.0023	C	2	79.9 × 45.4	130.0
28	NGC 4038	12:01:54.3	-18:53:03.1	0.0055	A	4	142.9 × 107.6	84.3
29	NGC 4382 ^b	12:25:24.1	18:11:29.4	0.0024	C	2	150.1 × 114.8	95.0
	NGC 4394	12:25:55.5	18:12:50.8	0.0031	C	2	110.2 × 95.0	15.0

Table A1 – *continued* Basic data for the SIGS sample galaxies.

Group ID	Galaxy ID	RA (J2000)	Dec	Redshift (z)	Sample	Interaction Stage	Size (″ × ″)	Angle ^a (°)
30	NGC 4567	12:36:31.5	11:15:43.6	0.0075	C	3	72.0 × 43.2	145.0
	NGC 4568	12:36:34.5	11:14:12.5	0.0075	C	3	142.9 × 41.8	122.0
31	NGC 4618	12:41:32.9	41:08:42.4	0.0018	C	3	135.0 × 105.1	115.0
	NGC 4625	12:41:52.7	41:16:26.4	0.0021	C	3	65.5 × 57.2	56.7
32	NGC 4647	12:43:31.7	11:35:03.5	0.0047	C	3	68.0 × 55.1	20.0
	NGC 4649	12:43:40.0	11:33:09.7	0.0037	C	3	119.9 × 95.0	10.0
33	NGC 4933A ^b	13:03:53.9	-11:30:23.8	0.0104	A	4	24.8 × 20.2	155.0
	NGC 4933B	13:03:57.2	-11:29:43.8	0.0108	A	4	40.0 × 38.2	130.0
	NGC 4933C	13:04:01.1	-11:29:26.2	0.0106	A	4	15.8 × 14.0	20.0
34	M51A	13:29:51.6	47:10:34.7	0.0015	C	3	273.2 × 204.0	120.0
	M51B	13:29:59.6	47:15:58.0	0.0016	C	3	107.6 × 65.5	5.0
35	NGC 5350	13:53:21.6	40:21:50.0	0.0077	C	3	100.1 × 69.8	125.0
35	NGC 5353	13:53:26.7	40:16:58.8	0.0078	C	3	52.9 × 28.1	52.0
	NGC 5354	13:53:26.7	40:18:10.1	0.0086	C	2	42.1 × 36.0	0.0
36	NGC 5394	13:58:32.4	37:27:14.8	0.0115	C	4	50.0 × 45.0	110.0
	NGC 5395	13:58:38.0	37:25:28.2	0.0117	C	4	92.2 × 50.4	87.2
37	NGC 5457	14:03:12.5	54:20:56.4	0.0008	C	3	650.2 × 650.0	0.0
	NGC 5474	14:05:01.6	53:39:43.9	0.0009	C	3	142.6 × 124.0	282.5
38	NGC 5426	14:03:24.8	-06:04:08.8	0.0086	A	4	79.9 × 51.8	75.0
	NGC 5427	14:03:26.0	-06:01:50.9	0.0087	A	4	77.0 × 61.9	0.0
39	NGC 5480	14:06:21.6	50:43:30.4	0.0062	C	2	62.6 × 50.0	85.0
	NGC 5481	14:06:41.3	50:43:23.9	0.0066	C	2	60.1 × 42.1	15.0
40	NGC 5544	14:17:03.0	36:34:19.6	0.0101	C	3	69.8 × 42.1	150.0
41	NGC 5614	14:24:07.6	34:51:31.7	0.013	C	4	79.2 × 45.4	45.0
42	NGC 5846 ^b	15:06:29.3	01:36:20.2	0.0057	C	2	92.2 × 81.4	125.0
	NGC 5850	15:07:07.7	01:32:39.1	0.0085	C	2	138.0 × 110.0	10.0
43	NGC 5905	15:15:23.3	55:31:02.6	0.0113	C	3	160.0 × 75.0	38.0
	NGC 5908	15:16:43.2	55:24:33.5	0.011	C	2	83.5 × 41.8	63.2
44	NGC 5929	15:26:05.4	41:40:07.3	0.0083	C	4	22.7 × 20.2	130.0
	NGC 5930	15:26:08.2	41:40:44.0	0.0087	C	4	67.0 × 23.4	70.0
45	NGC 5953	15:34:31.9	15:11:38.8	0.0066	A	4	31.0 × 28.1	160.0
	NGC 5954	15:34:34.8	15:12:05.8	0.0065	A	4	38.5 × 20.9	90.0
46	NGC 5981	15:37:53.4	59:23:30.5	0.0059	C	2	95.0 × 15.5	49.2
	NGC 5985	15:39:37.1	59:19:54.8	0.0084	C	2	169.9 × 82.1	110.0
47	Arp 314A	22:58:02.2	-03:46:10.9	0.0123	A	4	34.9 × 28.1	115.0
	Arp 314C ^b	22:58:07.4	-03:48:41.4	0.0123	A	4	38.2 × 31.0	70.0
	Arp 314B	22:58:07.9	-03:47:19.7	0.0124	A	4	34.9 × 32.0	90.0
48	NGC 7715	23:36:22.1	02:09:23.4	0.0092	A	4	52.9 × 23.4	160.0
	NGC 7714	23:36:14.1	02:09:18.6	0.0093	A	4	81.7 × 53.3	155.0

Note: Group IDs, Redshifts, Sample, and Interaction Stages are taken from B15, as described in Sec. 2.1. A Sample of C or A indicates objects belonging to the Keel-Complete sample or the Arp sample, respectively. The RA, Dec, Size, and Angle columns correspond to the centroids, semi-axis lengths, and position angles of the elliptical apertures used for the photometry as described in Sec. 3.3.

^a Angles are given in degrees from the East as measured by *photutils* (Sec. 3.2), so Angle=PA-90 degrees.

^b This galaxy was not analyzed in the SED models described in Sec. 4.1 because the photometry was too sparse to support reliable SED models.

Table A2. Basic data for the SB sample galaxies.

Galaxy ID	RA (J2000)	Dec	Redshift (z)	Sample	Size (″ × ″)	Angle ^a (°)
NGC 23	00:09:53.4	25:55:25.6	0.0152	S	86.3 × 58.2	90.0
NGC 253	00:47:32.4	-25:17:44.0	0.0008	S	820.4 × 226.5	140.0
NGC 660	01:43:02.4	13:38:42.2	0.0028	SB	304.8 × 124.2	75.0
NGC 1222	03:08:56.7	-02:57:18.5	0.0081	B	73.4 × 60.0	70.0
NGC 1365	03:33:36.4	-36:08:28.2	0.0055	B	353.8 × 221.6	128.0
IC 342	03:46:48.5	68:05:46.9	0.0001	B	716.5 × 598.5	0.0
NGC 1614	04:33:59.8	-08:34:44.0	0.0159	B	82.9 × 54.9	114.7
NGC 1797	05:07:44.9	-08:01:08.7	0.0149	S	66.7 × 41.0	162.9
NGC 2146	06:18:37.7	78:21:25.3	0.003	B	174.8 × 125.9	210.0
NGC 2623	08:38:24.0	25:45:16.1	0.0185	B	76.4 × 45.8	160.0
NGC 3256	10:27:51.3	-43:54:13.5	0.0094	SB	224.4 × 135.8	10.0
NGC 3310	10:38:45.9	53:30:12.2	0.0033	B	126.4 × 104.4	93.3
NGC 3556	11:11:31.0	55:40:26.8	0.0023	B	262.2 × 85.7	170.0
NGC 3628	11:20:17.0	13:35:22.9	0.0028	B	508.4 × 219.2	13.0
NGC 4088	12:05:34.2	50:32:20.5	0.0025	SB	187.7 × 103.1	143.0
NGC 4194	12:14:09.5	54:31:36.6	0.0083	B	92.2 × 53.4	90.0
Mrk 52	12:25:42.8	00:34:21.4	0.0071	B	62.7 × 38.4	170.0
NGC 4676	12:46:10.7	30:43:38.0	0.022	B	155.1 × 54.5	90.0
NGC 4818	12:56:48.8	-08:31:37.0	0.0036	B	145.8 × 66.0	90.0
NGC 4945	13:05:27.5	-49:28:05.6	0.0019	SB	571.9 × 150.0	133.0
NGC 7252	22:20:44.7	-24:40:41.7	0.016	B	71.0 × 62.7	80.0

Note: The RA, Dec, Size, and Angle columns define the centroids, semi-axis lengths, and angles of the elliptical apertures used for the photometry of the starburst sample galaxies. Redshifts were taken from NED. Samples are B for Brandl et al. (2006) and S for added well known local starbursts.

^a Angles are given in degrees from the East as measured by *photutils* (Sec. 3.2), so Angle=PA-90 degrees.

Table A3. Basic data for the AGN sample galaxies.

Galaxy ID	RA (J2000)	Dec	Redshift (z)	Sample	Size (″ × ″)	Angle ^a (°)
Mrk 335	00:06:19.5	20:12:10.5	0.0258	S	26.9 × 26.8	84.2
Mrk 1502	00:53:34.9	12:41:36.2	0.0589	S	29.0 × 28.5	45.0
NGC 931	02:28:14.5	31:18:42.0	0.0167	S	100.9 × 35.7	165.7
NGC 1068	02:42:40.7	-00:00:47.8	0.0038	HRG	215.1 × 174.7	170.0
NGC 1194	03:03:49.1	-01:06:13.5	0.0136	S	100.7 × 42.7	50.6
NGC 1320	03:24:48.7	-03:02:32.2	0.0089	S	63.5 × 33.9	47.2
ESO 33-2	04:55:59.0	-75:32:28.2	0.0181	S	31.0 × 29.0	45.0
4U 0557-385	05:58:02.0	-38:20:04.7	0.0339	S	25.0 × 23.0	229.3
Mrk 3	06:15:36.4	71:02:15.1	0.0135	S	48.6 × 42.9	55.0
ESO 428-14	07:16:31.2	-29:19:29.0	0.0057	S	46.2 × 32.0	230.0
NGC 3281	10:31:52.1	-34:51:13.3	0.0107	S	114.6 × 54.7	55.0
NGC 3516	11:06:47.5	72:34:06.9	0.0088	S	53.3 × 52.4	33.8
NGC 4151	12:10:32.6	39:24:20.6	0.0033	HR	256.1 × 246.5	50.0
NGC 4388	12:25:46.8	12:39:43.5	0.0084	S	200.7 × 54.2	179.4
Mrk 771	12:32:03.6	20:09:29.2	0.063	S	27.8 × 26.6	21.1
NGC 4941	13:04:13.1	-05:33:05.8	0.0037	S	121.6 × 78.3	286.9
MCG -03-34-064	13:22:24.5	-16:43:42.5	0.0165	G	41.5 × 31.0	141.9
ESO 383-35	13:35:53.7	-34:17:43.9	0.0077	S	27.9 × 19.4	29.7
ESO 445-50	13:49:19.3	-30:18:34.0	0.0161	S	42.0 × 26.0	133.7
NGC 5506	14:13:14.9	-03:12:27.3	0.0062	S	87.3 × 34.9	179.8
2XMM J141348.3+440014	14:13:48.3	44:00:14.0	0.0896	S	28.0 × 24.0	54.3
NGC 5548	14:17:59.5	25:08:12.4	0.0172	S	54.2 × 44.6	190.2
Mrk 1383	14:29:06.6	01:17:06.5	0.0866	S	29.2 × 28.5	3.9
Mrk 841	15:04:01.2	10:26:16.1	0.0364	S	37.5 × 34.0	105.0
ESO 141-55	19:21:14.1	-58:40:13.1	0.0371	S	33.0 × 29.0	0.0
IC 5063	20:52:02.3	-57:04:07.6	0.0113	S	79.8 × 62.6	205.1
Mrk 1513	21:32:27.8	10:08:19.5	0.063	S	26.2 × 23.9	328.2
Leda 68751	22:23:49.5	-02:06:12.8	0.0559	S	20.0 × 18.0	15.0
NGC 7674	23:27:57.0	08:46:43.3	0.0289	HRG	50.0 × 50.0	0.0

Note: The RA, Dec, Size, and Angle columns define the centroids, semi-axis lengths, and angles of the elliptical apertures used for the photometry of the AGN sample galaxies. Redshifts were taken from NED. The Sample column indicates whether objects belong to the GOALS sample (G), [Higuera-G. & Ramos P. \(2013\)](#) (HR) or taken from SIMBAD (S).

^a Angles are given in degrees from the East as measured by *photutils* (Sec. 3.2), so Angle=PA-90 degrees.

Table A4. Basic data for 38 of the 49 LSM sample galaxies.

Galaxy ID	RA (J2000)	Dec	Redshift (z)	$\log(L_{IR})$ (L_{\odot})	Stage	Size (″ × ″)	Angle ^a (°)
NGC 0078	00:20:26.6	00:49:46.7	0.0183	9.98	2.0	60.0 × 35.0	145.0
UM 246	00:29:45.1	00:10:09.0	0.0594	10.83	4.5	60.0 × 30.0	45.0
2MASX J01221811+0100262	01:22:17.8	01:00:27.5	0.0555	11.54	4.0	39.0 × 36.0	30.0
CGCG 087-046	07:54:31.8	16:48:26.3	0.0463	11.28	4.0	45.0 × 35.0	115.0
UGC 04383	08:23:33.5	21:20:34.7	0.0179	10.46	3.0	55.0 × 38.0	125.0
2MASX J08343370+1720462	08:34:33.7	17:20:46.4	0.0479	10.86	4.0	30.0 × 28.0	115.0
2MASX J08381760+3054533	08:38:17.6	30:54:53.5	0.0477	10.62	4.0	28.0 × 22.0	110.0
2MASX J08434495+3549421	08:43:45.0	35:49:42.0	0.054	10.45	5.0	28.0 × 25.0	55.0
UGC 05044	09:27:44.0	12:17:12.3	0.029	10.52	4.0	50.0 × 45.0	110.0
Arp 142	09:37:44.0	02:45:15.1	0.0233	10.89	3.5	65.0 × 55.0	130.0
CGCG 266-026	10:10:00.8	54:40:19.8	0.0462	10.91	4.5	50.0 × 32.0	155.0
LSBCF 567-01	10:19:01.5	21:17:01.3	0.0036	8.38	5.0	65.0 × 35.0	65.0
2MASX J10225654+3446467	10:22:56.6	34:46:46.8	0.0561	10.66	3.5	40.0 × 32.0	65.0
UGC 05644	10:25:46.3	13:43:00.7	0.0323	10.52	3.0	75.0 × 32.0	130.0
CGCG 037-076	10:33:28.6	07:08:03.8	0.0445	10.79	4.0	33.0 × 28.0	70.0
UGC A219	10:49:05.0	52:20:07.8	0.008	8.82	5.0	30.0 × 25.0	60.0
NGC 3445	10:54:35.5	56:59:26.5	0.0068	9.76	3.0	50.0 × 45.0	70.0
2MASX J10591815+2432343	10:59:18.1	24:32:34.5	0.0431	12.18	3.5	50.0 × 42.0	20.0
VV 627	11:00:59.8	57:47:04.0	0.0477	10.60	4.0	70.0 × 40.0	145.0
IC 0700	11:29:15.5	20:35:05.7	0.0049	8.57	5.0	55.0 × 30.0	155.0
UGC 06665	11:42:12.4	00:20:02.5	0.0186	10.83	5.0	60.0 × 48.0	125.0
UGC 07388	12:20:15.7	33:39:38.9	0.0215	10.52	5.0	40.0 × 35.0	125.0
NGC 4320	12:22:57.7	10:32:54.0	0.0267	10.55	4.5	60.0 × 45.0	115.0
UGC 07936	12:46:00.1	45:12:00.0	0.0247	10.23	4.0	65.0 × 50.0	130.0
Mrk 0237	13:01:17.6	48:03:38.0	0.0298	10.87	4.0	50.0 × 38.0	30.0
UGC 08327	13:15:15.6	44:24:26.0	0.0367	11.17	3.5	60.0 × 42.0	0.0
UGC 08335	13:15:33.1	62:07:30.4	0.0308	11.70	4.0	60.0 × 35.0	35.0
NGC 5100	13:20:58.6	08:58:55.0	0.0319	11.21	3.5	60.0 × 50.0	50.0
CGCG 017-018	13:32:55.9	-03:01:37.0	0.0465	10.86	2.0	38.0 × 25.0	20.0
NGC 5331	13:52:16.3	02:06:10.9	0.033	11.23	3.0	65.0 × 50.0	80.0
CGCG 076-015 ^b	14:44:27.1	12:15:25.8	0.0528	10.96	4.0	23.0 × 23.0	0.0
UGC 09618	14:57:00.5	24:36:49.9	0.0329	11.26	2.0	60.0 × 40.0	95.0
2MASX J15015015+2332536	15:01:50.2	23:32:53.7	0.0463	10.92	4.5	32.0 × 27.0	60.0
SBS 1509+583	15:10:17.8	58:10:37.5	0.0319	10.37	2.0	35.0 × 25.0	30.0
KUG 1553+200	15:55:56.9	19:56:58.0	0.0413	11.00	4.0	32.0 × 32.0	0.0
KUG 1556+326	15:58:37.8	32:27:42.2	0.0482	10.76	3.0	38.0 × 32.0	110.0
Mrk 0881	16:25:49.4	40:20:42.7	0.0288	10.90	5.0	35.0 × 30.0	95.0
2MASX J17045097+3449020	17:04:50.9	34:49:02.4	0.0563	11.31	2.0	35.0 × 30.0	40.0

Note: The RA, Dec, Size, and Angle columns define the centroids, semi-axis lengths, and angles of the elliptical apertures used for the photometry of the LSM sample galaxies. This table presents data for 38 galaxies; corresponding quantities for the remainder of the 49-galaxy sample appear in Table 1 of [Dietrich et al. \(2018\)](#). Redshifts were taken from NED. Infrared luminosities were taken from the Revised IRAS-FSC Redshift Catalog (RIFSCz, [Wang et al. 2014](#)). The stages were determined by the entire team as described in Sec. 2.1.

^a Angles are given in degrees from the East as measured by *photutils* (Sec. 3.2), so Angle=PA−90 degrees.

^b This galaxy was not analyzed in the SED models described in Sec. 4.1 because the photometry was too sparse to support reliable SED models.

Table A5. Integrated IR line intensities measured for SB sample galaxies using PAHFIT in units of $1 \times 10^{-21} \text{ W cm}^{-2}$.

Galaxy ID	[Ne II] 12.81 μm	[Ne III] 15.56 μm	[Ne V] 14.32 μm	[S III] 18.71 μm	[S IV] 10.51 μm	[Fe II] 12.64 μm	H ₂ S(2) 12.28 μm	H ₂ S(1) 17.03 μm
NGC 23	49.37±0.14	6.95±0.04	...	16.08±0.14	1.62±0.06	0.48±0.06	5.71±0.11	6.65±0.07
NGC 253	2689.15±1.29	183.27±0.57	...	576.23±1.08	...	77.21±0.83	93.53±0.80	79.39±0.67
NGC 520	46.18±0.21	6.84±0.09	0.23±0.08	6.71±0.11	0.13±0.09	...	5.24±0.12	8.89±0.10
NGC 660	286.20±0.34	27.60±0.19	1.30±0.14	54.78±0.24	1.47±0.22	3.40±0.14	6.30±0.13	17.82±0.20
NGC 1222	82.21±0.16	78.18±0.13	0.47±0.06	49.33±0.17	25.16±0.12	0.69±0.09	4.79±0.09	7.92±0.08
NGC 1365	178.44±0.37	55.36±0.23	18.74±0.20	55.25±0.30	28.31±0.29	4.35±0.17	12.61±0.18	20.18±0.18
IC 342	639.63±0.38	34.58±0.16	2.31±0.16	255.47±0.39	5.20±0.21	11.80±0.21	12.01±0.26	9.30±0.18
NGC 1614	265.07±0.30	66.59±0.19	1.63±0.10	70.91±0.30	11.65±0.17	1.97±0.14	6.84±0.15	10.05±0.14
NGC 1797	67.82±0.19	5.33±0.07	0.34±0.12	18.63±0.16	1.11±0.09	0.53±0.10	3.50±0.14	3.92±0.10
NGC 2146	803.04±1.52	121.59±0.43	2.99±0.31	253.62±1.17	21.55±0.82	10.90±0.30	10.07±0.28	37.91±0.35
NGC 2623	73.10±0.57	20.68±0.26	3.54±0.11	13.55±0.32	7.31±0.42	1.31±0.21	5.51±0.17	14.12±0.31
NGC 3256	495.57±0.50	61.04±0.18	0.92±0.15	138.36±0.35	10.49±0.17	8.29±0.20	20.34±0.17	26.12±0.16
NGC 3310	43.45±0.22	28.62±0.15	0.25±0.10	19.36±0.26	5.56±0.15	0.46±0.09	0.84±0.16	2.04±0.13
NGC 3556	21.51±0.10	3.01±0.05	0.06±0.06	10.28±0.12	0.42±0.10	0.24±0.08	1.67±0.12	2.46±0.06
NGC 3628	170.98±0.66	13.28±0.12	0.69±0.09	32.91±0.31	...	2.92±0.18	10.02±0.21	28.46±0.29
NGC 4088	35.01±0.14	2.24±0.06	0.43±0.16	9.31±0.08	0.28±0.13	0.28±0.06	2.45±0.09	3.97±0.06
NGC 4194	162.22±0.26	50.57±0.17	1.99±0.09	56.92±0.22	15.11±0.21	2.50±0.14	6.63±0.15	7.26±0.13
Mrk 52	24.39±0.09	3.34±0.07	...	17.71±0.09	1.11±0.07	0.41±0.06	1.00±0.06	1.54±0.07
NGC 4676	34.68±0.23	6.87±0.12	0.44±0.05	16.18±0.22	2.63±0.20	0.65±0.08	3.07±0.09	8.86±0.15
NGC 4818	154.06±0.22	11.12±0.12	0.97±0.12	47.40±0.24	2.35±0.10	4.34±0.17	6.11±0.32	13.59±0.15
NGC 4945	978.73±2.18	114.10±0.49	9.49±0.27	106.69±0.77	31.63±2.62	17.47±0.50	80.48±0.50	228.37±1.41
NGC 7252	36.31±0.13	2.99±0.06	0.34±0.06	8.28±0.09	0.12±0.07	0.08±0.05	3.12±0.13	3.56±0.07
NGC 7714	94.55±0.17	63.77±0.11	...	56.86±0.14	16.38±0.15	2.26±0.11	3.44±0.10	3.19±0.09

Table A6. *GALEX* and SDSS DR12 photometry for the four study samples.

Galaxy ID	<i>GALEX</i>		SDSS DR12				
	FUV (mJy)	NUV (mJy)	<i>u</i> (mJy)	<i>g</i> (mJy)	<i>r</i> (mJy)	<i>i</i> (mJy)	<i>z</i> (mJy)
Photometry for the SIGS sample							
NGC274	4.53 ± 0.13	21.15 ± 0.42	43.97 ± 0.88	64.74 ± 1.30	81.14 ± 1.66
NGC275	3.30 ± 0.33	4.56 ± 0.46	10.80 ± 0.24	23.35 ± 0.47	36.91 ± 0.74	43.79 ± 0.88	50.87 ± 1.08
NGC470	3.18 ± 0.32	4.67 ± 0.47	16.59 ± 0.37	44.43 ± 0.89	78.42 ± 1.57	107.23 ± 2.15	131.44 ± 2.67
NGC474	1.44 ± 0.15	1.98 ± 0.20	20.66 ± 0.61	67.87 ± 1.36	125.69 ± 2.52	179.48 ± 3.61	243.94 ± 5.05
NGC520	1.69 ± 0.17	3.12 ± 0.31	4.25 ± 0.22	62.00 ± 1.25	113.32 ± 2.27	160.68 ± 3.22	192.31 ± 3.92
IC195	0.05 ± 0.01	0.10 ± 0.01	1.96 ± 0.06	9.48 ± 0.19	19.99 ± 0.40	29.45 ± 0.59	37.98 ± 0.77
IC196	0.65 ± 0.06	0.82 ± 0.08	4.33 ± 0.14	18.03 ± 0.36	36.51 ± 0.73	53.72 ± 1.08	68.04 ± 1.41
NGC833	...	0.29 ± 0.03	3.33 ± 0.09	16.49 ± 0.33	35.86 ± 0.72	53.35 ± 1.07	68.14 ± 1.39
NGC835	...	1.67 ± 0.17	7.74 ± 0.17	29.07 ± 0.58	57.24 ± 1.15	81.33 ± 1.63	102.36 ± 2.07
NGC838	...	2.04 ± 0.20	6.39 ± 0.14	16.92 ± 0.34	30.38 ± 0.61	39.34 ± 0.79	48.92 ± 1.02

Note: Photometry expressed in mJy in the UV and optical bands for the SIGS, SB, AGN, and LSM samples described in Sec. 2. The full table is available in the online version of this paper. A portion is shown here for guidance regarding its form and content.

Table A7. 2MASS and *Spitzer*/IRAC photometry for the four study samples.

Galaxy ID	2MASS			<i>Spitzer</i> /IRAC			
	<i>J</i> (mJy)	<i>H</i> (mJy)	<i>K_s</i> (mJy)	3.6 μm (mJy)	4.5 μm (mJy)	5.8 μm (mJy)	8.0 μm (mJy)
Photometry for the SIGS sample							
NGC274	111.29 ± 2.28	132.95 ± 2.76	102.24 ± 2.28	50.25 ± 1.51	31.65 ± 0.95	23.19 ± 0.70	17.06 ± 0.52
NGC275	64.31 ± 1.41	73.18 ± 1.68	59.58 ± 1.68	39.06 ± 1.17	27.29 ± 0.82	70.69 ± 2.13	170.52 ± 5.12
NGC470	186.08 ± 3.96	199.56 ± 4.58	184.86 ± 4.47	108.22 ± 3.25	73.47 ± 2.20	163.96 ± 4.93	417.70 ± 12.53
NGC474	296.05 ± 7.02	314.31 ± 8.98	271.30 ± 8.35	149.83 ± 4.50	86.50 ± 2.60	141.57 ± 4.34	100.29 ± 3.14
NGC520	288.70 ± 6.23	357.34 ± 8.33	312.68 ± 7.30	182.73 ± 5.48	138.65 ± 4.16	357.79 ± 10.74	916.85 ± 27.51
IC195	54.38 ± 1.22	66.50 ± 1.60	53.22 ± 1.47	25.29 ± 0.76	15.80 ± 0.47	10.82 ± 0.34	6.30 ± 0.21
IC196	95.34 ± 2.39	129.52 ± 3.48	105.90 ± 3.34	49.53 ± 1.49	32.17 ± 0.97	29.94 ± 0.92	42.85 ± 1.30
NGC833	101.56 ± 2.08	125.16 ± 2.62	106.44 ± 2.32	48.47 ± 1.45	30.78 ± 0.92	25.01 ± 0.76	25.52 ± 0.77
NGC835	155.86 ± 3.17	194.36 ± 4.01	166.35 ± 3.51	89.23 ± 2.68	60.95 ± 1.83	117.65 ± 3.53	291.88 ± 8.76
NGC838	73.96 ± 1.57	93.24 ± 2.04	86.14 ± 1.97	67.69 ± 2.03	50.08 ± 1.50	212.29 ± 6.37	589.03 ± 17.67

Note: Photometry in seven near- and mid-IR bands for the SIGS, SB, AGN, and LSM samples described in Sec. 2. The full table is available in the online version of this paper. A portion is shown here for guidance regarding its form and content.

Table A8. *WISE* and *Spitzer/MIPS* photometry for the four study samples.

Galaxy ID	<i>WISE</i>				<i>Spitzer/MIPS</i>		
	3.4 μm (mJy)	4.6 μm (mJy)	12 μm (mJy)	22 μm (mJy)	24 μm (mJy)	70 μm (Jy)	160 μm (Jy)
Photometry for the SIGS sample							
NGC274	52.6 \pm 3.2	28.3 \pm 1.7	11.3 \pm 0.7
NGC275	38.1 \pm 2.3	24.5 \pm 1.5	146.5 \pm 8.8	384.6 \pm 23.1	459.32 \pm 18.39	5.40 \pm 0.22	7.34 \pm 0.32
NGC470	112.5 \pm 6.8	69.5 \pm 4.2	334.5 \pm 20.1	802.2 \pm 48.1	799.55 \pm 32.02	9.59 \pm 0.39	13.72 \pm 0.55
NGC474	151.8 \pm 9.1	83.3 \pm 5.0	152.39 \pm 8.99
NGC520	183.0 \pm 11.0	131.4 \pm 7.9	738.3 \pm 44.3	2233.4 \pm 134.0	2347.72 \pm 93.94	33.44 \pm 1.34	...
IC195	26.0 \pm 1.6	13.9 \pm 0.8	4.2 \pm 0.3	3.5 \pm 0.3
IC196	52.6 \pm 3.2	28.4 \pm 1.7	37.5 \pm 2.3	36.0 \pm 2.2
NGC833	51.8 \pm 3.1	29.2 \pm 1.7	26.7 \pm 1.6	49.6 \pm 3.0
NGC835	89.9 \pm 5.4	56.5 \pm 3.4	242.0 \pm 14.5	412.1 \pm 24.7	434.53 \pm 17.43	6.82 \pm 0.27	9.33 \pm 0.38
NGC838	62.1 \pm 3.7	46.2 \pm 2.8	459.2 \pm 27.6	1344.6 \pm 80.7	1458.64 \pm 58.35	11.50 \pm 0.46	9.60 \pm 0.41

Note: Photometry in seven mid-IR bands for the SIGS, SB, AGN, and LSM samples described in Sec. 2. The full table is available in the online version of this paper. A portion is shown here for guidance regarding its form and content.

Table A9. *Herschel/PACS* and *SPIRE* photometry for the four study samples.

Galaxy ID	<i>Herschel/PACS</i>			<i>Herschel/SPIRE</i>		
	70 μm (Jy)	100 μm (Jy)	160 μm (Jy)	250 μm (Jy)	350 μm (Jy)	500 μm (Jy)
Photometry for the SIGS sample						
NGC274
NGC275	5.96 \pm 0.60	8.71 \pm 0.87	7.85 \pm 0.79
NGC470
NGC474
NGC520	41.68 \pm 4.17	51.86 \pm 5.19	39.13 \pm 3.91
IC195
IC196
NGC833	0.39 \pm 0.07	0.79 \pm 0.10	1.14 \pm 0.12	0.58 \pm 0.04	0.27 \pm 0.02	0.10 \pm 0.01
NGC835	7.44 \pm 0.75	11.72 \pm 1.17	10.58 \pm 1.06	4.04 \pm 0.28	1.49 \pm 0.10	0.46 \pm 0.03
NGC838	14.98 \pm 1.50	17.84 \pm 1.78	12.99 \pm 1.30	3.91 \pm 0.27	1.37 \pm 0.10	0.41 \pm 0.03

Note: Photometry in the FIR bands for the SIGS, SB, AGN, and LSM samples described in Sec. 2. The full table is available in the online version of this paper. A portion is shown here for guidance regarding its form and content.

This paper has been typeset from a $\text{\TeX}/\text{\LaTeX}$ file prepared by the author.

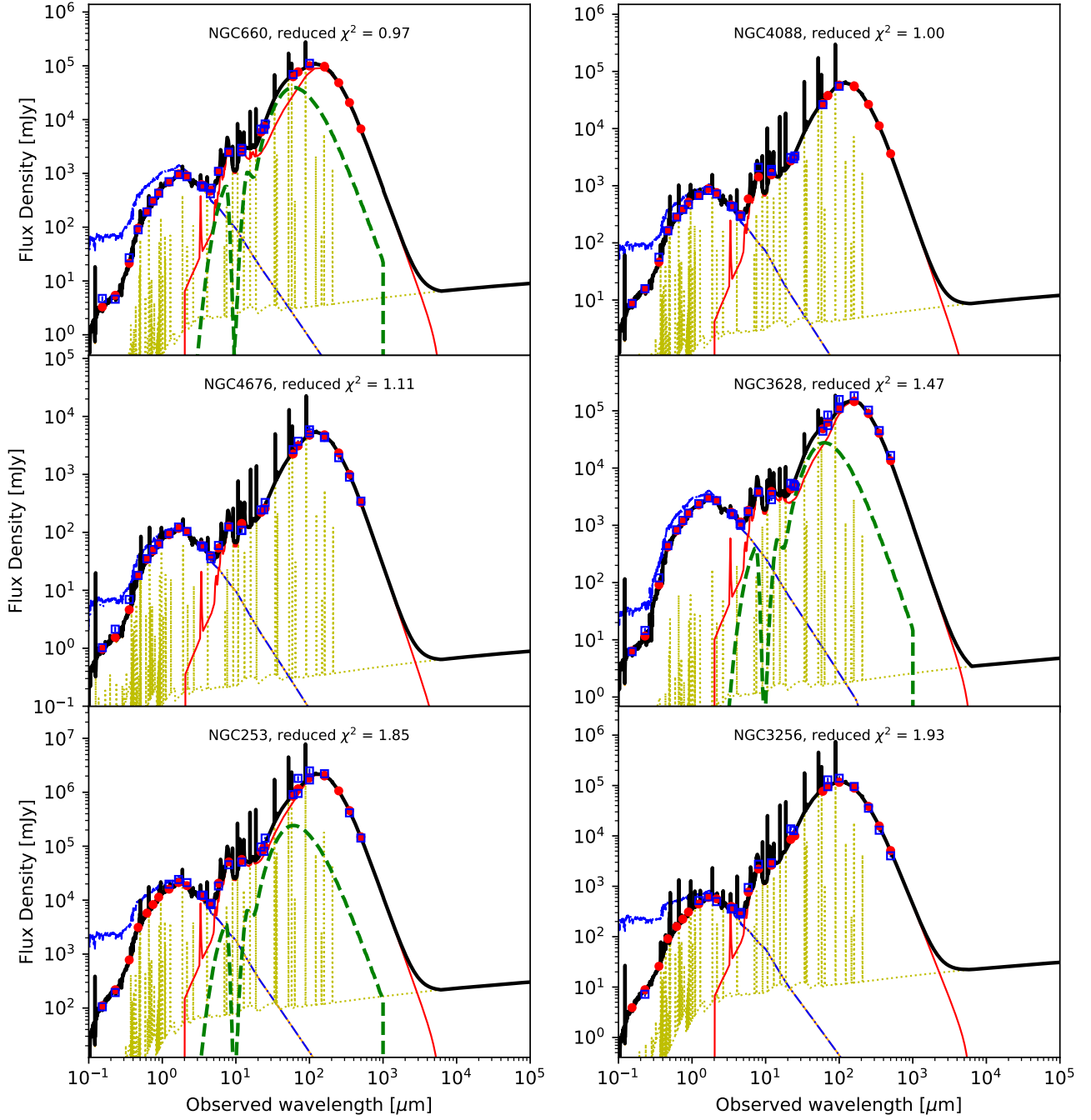


Figure A1. Best-fit SED models for 6 galaxies in the SB sample containing the nebular emission (gold dotted lines), both attenuated stellar emission (orange) and non-attenuated stellar emission (blue dot-dashed), dust emission (red solid), and AGN emission (green dashed). The red dots are the best model flux densities and the blue squares mark the observed flux densities with 1σ error bars.

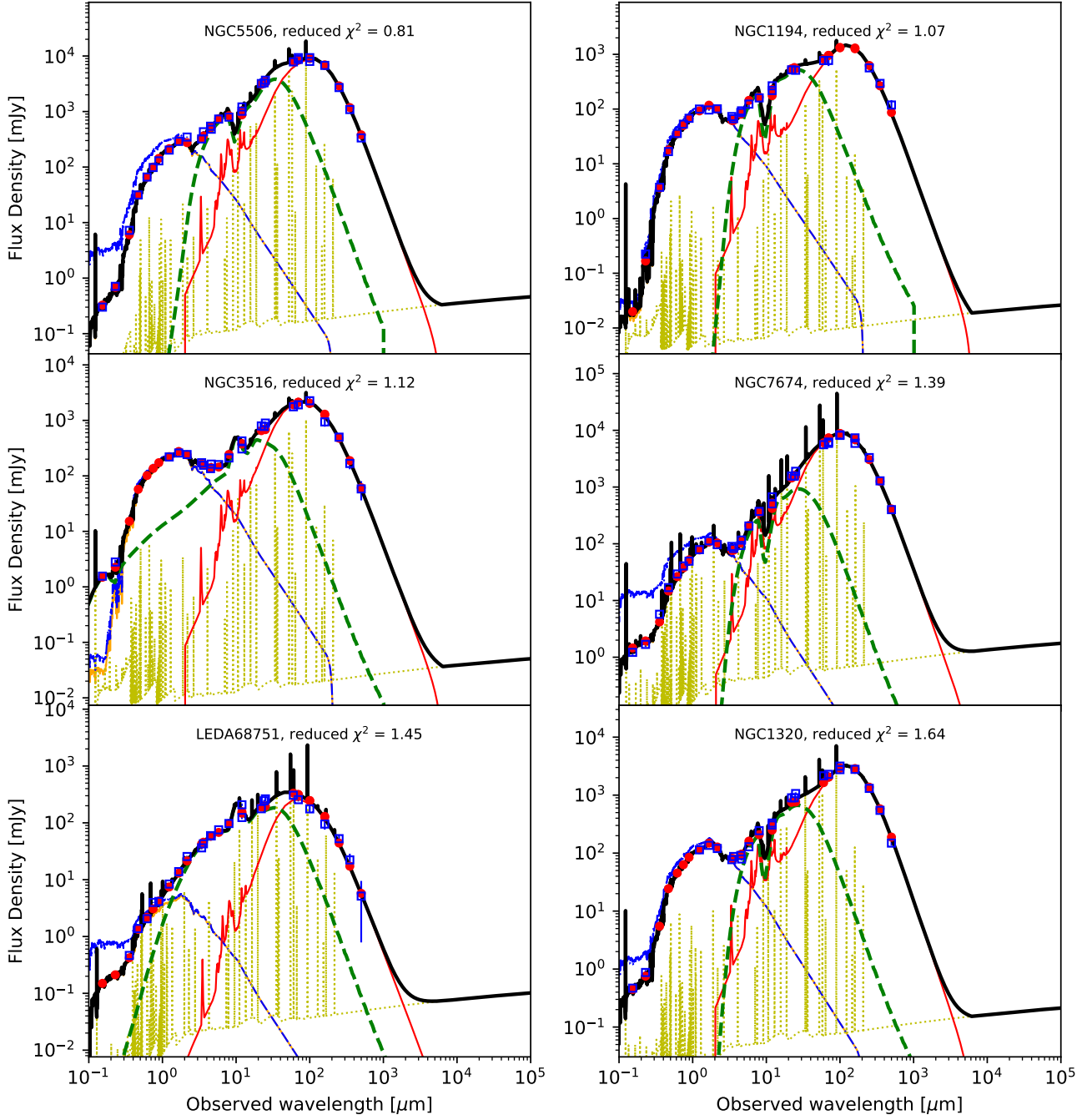


Figure A2. Best-fit SED models for 6 galaxies in the AGN sample. The colors and lines are identical to Figure A1.

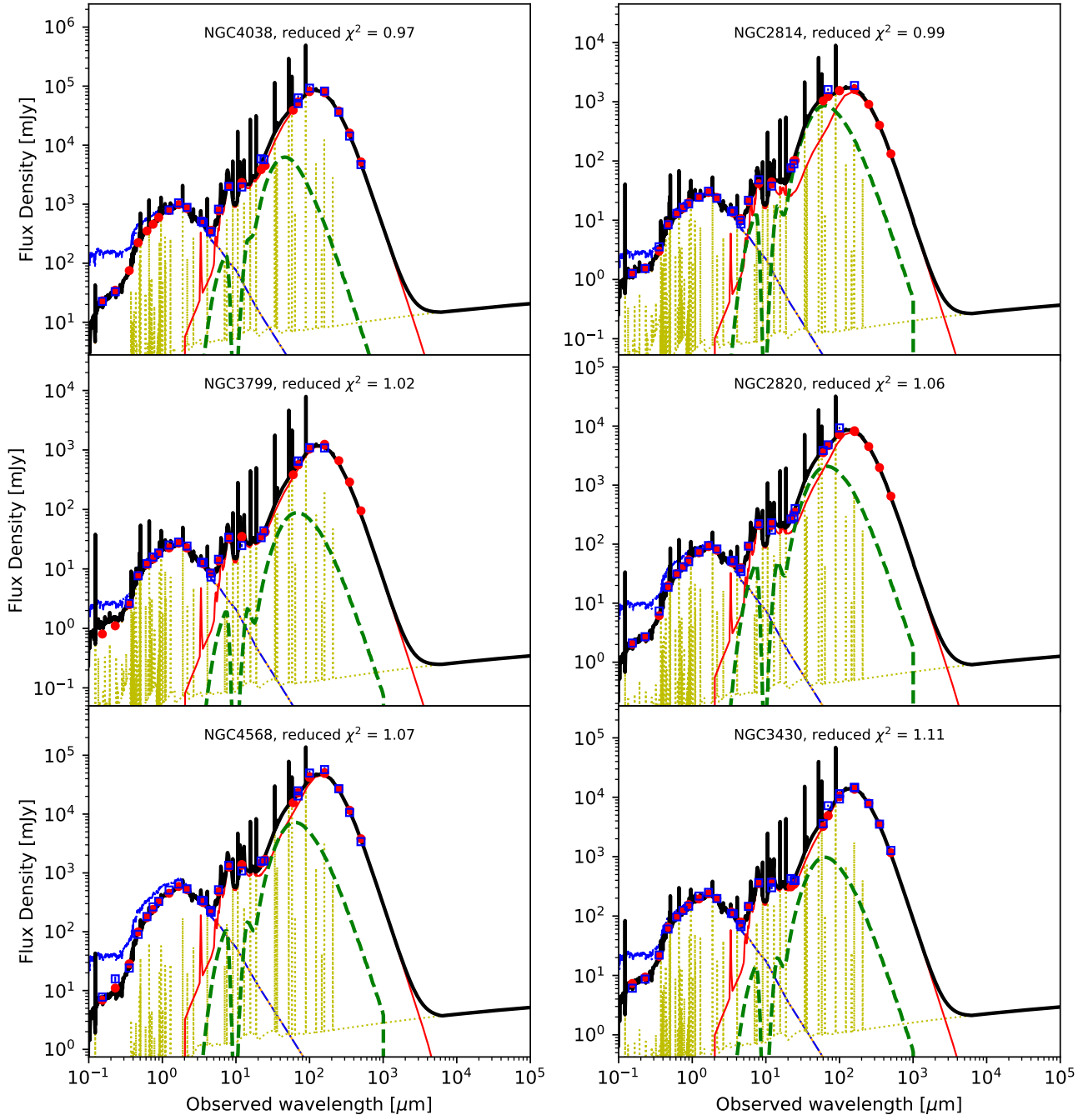


Figure A3. Best-fit SED models for 6 galaxies in the SIGS sample. The colors and lines are identical to Figure A1.

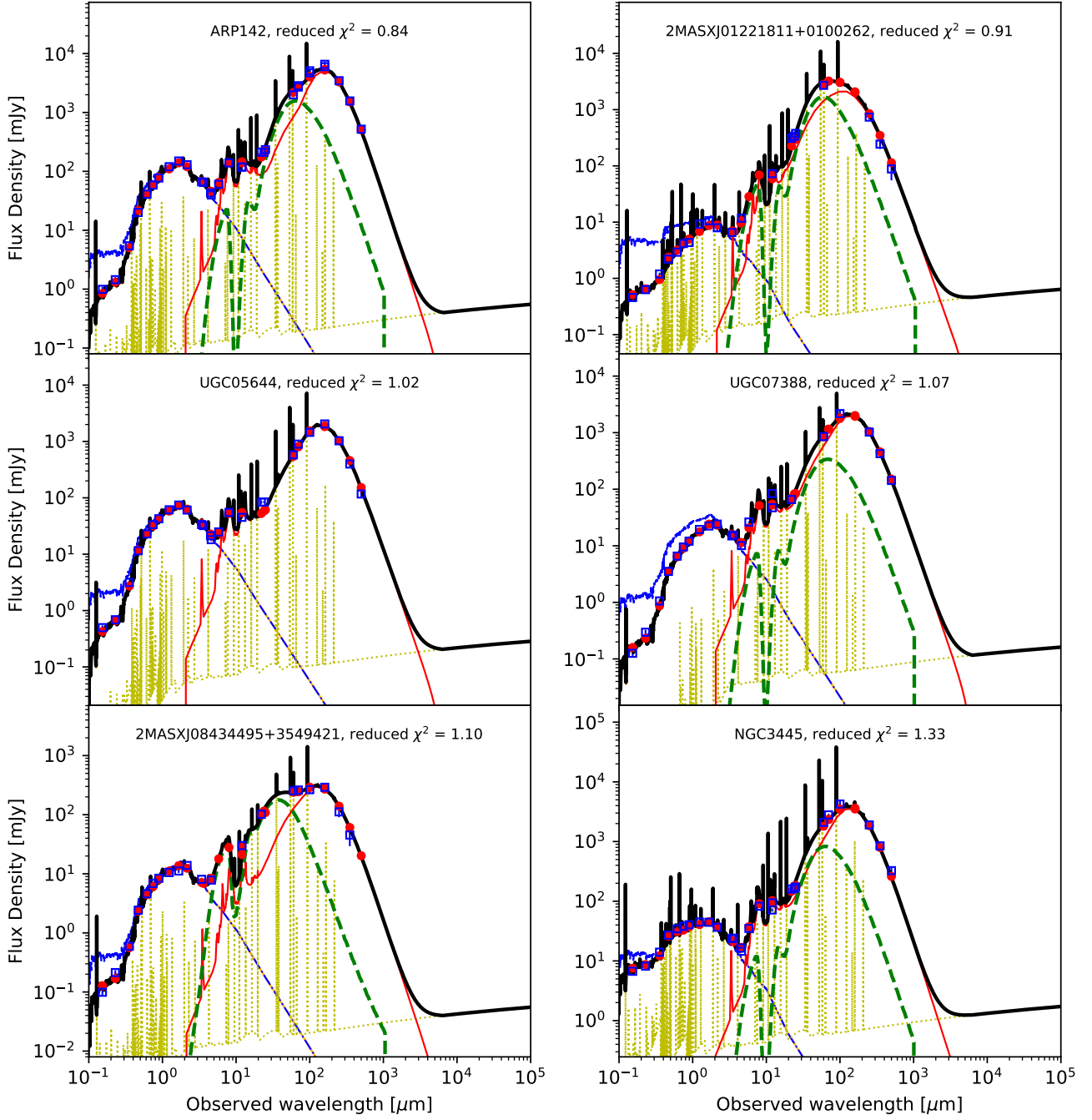


Figure A4. Best-fit SED models for 6 galaxies in the LSM sample. The colors and lines are identical to Figure A1.

Table A10. CIGALE-derived parameters for the AGN sample.

Galaxy ID	f_{AGN}	L_{AGN} $\log(L_{\odot})$	Old Att. $\log(L_{\odot})$	Young Att. $\log(L_{\odot})$	Dust α	L_{dust} $\log(L_{\odot})$
Mrk335	0.77 ± 0.04	11.03 ± 0.02	9.42 ± 0.15	9.78 ± 0.07	1.03 ± 0.08	9.99 ± 0.05
Mrk1502	0.49 ± 0.03	11.72 ± 0.02	11.28 ± 0.05	11.31 ± 0.04	1.52 ± 0.08	11.64 ± 0.03
NGC931	0.51 ± 0.04	10.68 ± 0.04	10.50 ± 0.04	9.95 ± 0.07	2.68 ± 0.21	10.62 ± 0.04
NGC1068	0.42 ± 0.07	10.93 ± 0.08	10.86 ± 0.07	10.56 ± 0.11	2.01 ± 0.10	11.06 ± 0.05
NGC1194	0.66 ± 0.07	10.17 ± 0.05	9.83 ± 0.08	8.06 ± 0.44	2.20 ± 0.24	9.84 ± 0.08
NGC1320	0.43 ± 0.06	9.85 ± 0.05	9.87 ± 0.06	9.08 ± 0.30	1.89 ± 0.12	9.95 ± 0.07
ESO33-2	0.63 ± 0.03	10.33 ± 0.02	10.02 ± 0.03	7.99 ± 0.59	1.75 ± 0.09	10.03 ± 0.03
4U0557-385	0.90 ± 0.04	11.25 ± 0.02	10.14 ± 0.04	9.32 ± 0.19	1.84 ± 0.12	10.21 ± 0.02
Mrk3	0.64 ± 0.06	10.62 ± 0.03	10.34 ± 0.08	8.75 ± 0.04	1.63 ± 0.13	10.36 ± 0.08
ESO428-14	0.31 ± 0.04	9.50 ± 0.06	9.77 ± 0.07	8.89 ± 0.44	1.74 ± 0.09	9.83 ± 0.03
NGC3281	0.40 ± 0.05	10.37 ± 0.07	10.52 ± 0.03	8.25 ± 0.99	1.75 ± 0.09	10.52 ± 0.03
NGC3516	0.45 ± 0.03	10.12 ± 0.05	9.85 ± 0.04	7.98 ± 1.06	1.44 ± 0.11	9.86 ± 0.03
NGC4151	0.67 ± 0.07	9.86 ± 0.08	9.25 ± 0.19	8.92 ± 0.20	2.18 ± 0.19	9.44 ± 0.07
NGC4388	0.24 ± 0.04	10.14 ± 0.08	10.49 ± 0.03	10.00 ± 0.05	2.01 ± 0.10	10.63 ± 0.02
Mrk771	0.53 ± 0.03	11.47 ± 0.04	10.63 ± 0.07	9.06 ± 1.66	1.68 ± 0.11	10.64 ± 0.04
NGC4941	9.39 ± 0.02	8.40 ± 0.02	2.71 ± 0.20	9.44 ± 0.02
MCG-03-34-064	0.46 ± 0.04	10.69 ± 0.06	10.67 ± 0.05	9.82 ± 0.29	1.49 ± 0.07	10.74 ± 0.03
ESO383-35	0.65 ± 0.04	9.85 ± 0.03	9.47 ± 0.05	8.31 ± 0.30	1.33 ± 0.12	9.51 ± 0.06
ESO445-50	0.81 ± 0.04	10.99 ± 0.02	10.28 ± 0.05	8.18 ± 0.56	1.55 ± 0.10	10.29 ± 0.05
NGC5506	0.56 ± 0.03	10.25 ± 0.03	10.05 ± 0.02	8.94 ± 0.02	1.75 ± 0.09	10.09 ± 0.02
2XMMJ141348.3+440014	0.85 ± 0.04	11.89 ± 0.13	10.09 ± 0.27	10.36 ± 0.16	2.02 ± 0.10	10.59 ± 0.04
NGC5548	0.54 ± 0.08	10.46 ± 0.09	10.13 ± 0.15	9.47 ± 0.33	1.92 ± 0.15	10.23 ± 0.07
Mrk1383	0.65 ± 0.03	12.11 ± 0.02	11.04 ± 0.03	9.33 ± 1.13	1.75 ± 0.09	11.05 ± 0.02
Mrk841	0.64 ± 0.03	11.08 ± 0.02	9.78 ± 0.03	10.31 ± 0.02	1.00 ± 0.05	10.48 ± 0.02
ESO141-55	0.52 ± 0.03	11.33 ± 0.10	10.20 ± 0.25	10.57 ± 0.09	2.00 ± 0.10	10.77 ± 0.02
IC5063	0.70 ± 0.03	10.67 ± 0.02	10.28 ± 0.02	8.59 ± 0.26	2.00 ± 0.10	10.29 ± 0.02
Mrk1513	0.66 ± 0.03	11.69 ± 0.04	10.48 ± 0.11	10.78 ± 0.05	1.52 ± 0.08	11.00 ± 0.02
LEDA68751	0.80 ± 0.04	11.35 ± 0.03	10.32 ± 0.14	10.13 ± 0.19	1.21 ± 0.15	10.57 ± 0.04
NGC7674	0.27 ± 0.05	11.03 ± 0.08	11.23 ± 0.05	10.92 ± 0.04	1.77 ± 0.09	11.43 ± 0.04

Note: Galaxy ID is the common identifier used in the same order as in Table A3, f_{AGN} is the fraction of AGN contribution (from both torus and accretion) to the IR, or $L_{\text{IR}}^{\text{AGN}} = f_{\text{AGN}} \times L_{\text{IR}}^{\text{Tot}}$ as defined by Ciesla et al. (2015), L_{AGN} is the AGN luminosity of the three AGN components by Fritz et al. (2006), Old Att. is the attenuation from the old stellar population, Young Att. is the attenuation from the young stellar population, Dust α is the parameter that defines the contribution of the local heating intensity in the dust (eq. 1) and L_{dust} is the dust luminosity.

Table A10 – *continued* CIGALE-derived parameters for the AGN sample.

Galaxy ID	SFR $\log(M_{\odot}/\text{yr})$	τ_{main} $\log(\text{yr})$	Stellar Age $\log(\text{yr})$	M_{gas} $\log(M_{\odot})$	M_{\star} $\log(M_{\odot})$
Mrk335	0.49 ± 0.09	9.60 ± 0.28	8.34 ± 0.44	8.29 ± 0.64	8.94 ± 0.37
Mrk1502	1.86 ± 0.03	9.56 ± 0.33	8.92 ± 0.20	10.40 ± 0.17	10.93 ± 0.13
NGC931	0.49 ± 0.05	8.99 ± 0.04	9.61 ± 0.02	10.77 ± 0.02	11.16 ± 0.02
NGC1068	1.07 ± 0.11	8.95 ± 0.10	9.36 ± 0.07	10.70 ± 0.09	11.13 ± 0.08
NGC1194	-1.31 ± 0.42	8.47 ± 0.33	9.55 ± 0.09	10.45 ± 0.07	10.84 ± 0.06
NGC1320	-0.37 ± 0.25	8.81 ± 0.15	9.52 ± 0.06	10.15 ± 0.03	10.56 ± 0.02
ESO33-2	-1.46 ± 0.58	8.39 ± 0.40	9.56 ± 0.12	10.48 ± 0.10	10.88 ± 0.09
4U0557-385	-0.06 ± 0.11	8.72 ± 0.12	9.48 ± 0.04	10.61 ± 0.07	11.02 ± 0.07
Mrk3	-0.74 ± 0.03	8.70 ± 0.02	9.60 ± 0.02	10.77 ± 0.02	11.16 ± 0.02
ESO428-14	-0.59 ± 0.43	8.72 ± 0.39	9.40 ± 0.27	9.85 ± 0.18	10.28 ± 0.13
NGC3281	-1.19 ± 0.93	8.21 ± 0.52	9.40 ± 0.16	10.71 ± 0.11	11.12 ± 0.09
NGC3516	-1.35 ± 1.11	8.26 ± 0.49	9.52 ± 0.17	10.40 ± 0.13	10.80 ± 0.11
NGC4151	-0.36 ± 0.20	8.92 ± 0.18	9.57 ± 0.09	9.98 ± 0.06	10.38 ± 0.05
NGC4388	0.54 ± 0.04	8.75 ± 0.13	9.35 ± 0.11	10.51 ± 0.09	10.94 ± 0.07
Mrk771	-0.28 ± 1.89	8.57 ± 1.11	9.62 ± 0.12	10.78 ± 0.13	11.17 ± 0.12
NGC4941	-0.90 ± 0.02	8.70 ± 0.02	9.48 ± 0.02	9.82 ± 0.02	10.22 ± 0.02
MCG-03-34-064	0.33 ± 0.29	8.69 ± 0.28	9.34 ± 0.20	10.48 ± 0.14	10.91 ± 0.11
ESO383-35	-1.15 ± 0.26	8.70 ± 0.02	9.54 ± 0.06	9.85 ± 0.09	10.25 ± 0.08
ESO445-50	-1.28 ± 0.53	8.53 ± 0.28	9.67 ± 0.07	10.83 ± 0.08	11.21 ± 0.07
NGC5506	-0.55 ± 0.02	8.70 ± 0.02	9.48 ± 0.02	10.17 ± 0.02	10.57 ± 0.02
2XMMJ141348.3+440014	1.06 ± 0.20	9.54 ± 0.33	8.91 ± 0.53	9.65 ± 0.77	10.13 ± 0.61
NGC5548	0.14 ± 0.32	8.85 ± 0.25	9.59 ± 0.08	10.63 ± 0.08	11.03 ± 0.07
Mrk1383	-0.16 ± 1.13	8.40 ± 0.47	9.60 ± 0.13	11.18 ± 0.14	11.57 ± 0.12
Mrk841	1.04 ± 0.02	9.59 ± 0.29	9.01 ± 0.14	9.71 ± 0.13	10.22 ± 0.11
ESO141-55	1.30 ± 0.09	9.61 ± 0.29	9.11 ± 0.26	10.18 ± 0.45	10.66 ± 0.37
IC5063	-0.71 ± 0.15	8.70 ± 0.02	9.60 ± 0.02	10.77 ± 0.02	11.16 ± 0.02
Mrk1513	1.49 ± 0.05	9.60 ± 0.28	8.39 ± 0.45	9.41 ± 0.75	10.03 ± 0.54
LEDA68751	0.66 ± 0.18	9.39 ± 0.42	9.22 ± 0.30	10.00 ± 0.45	10.44 ± 0.41
NGC7674	1.45 ± 0.04	9.01 ± 0.09	9.36 ± 0.03	10.96 ± 0.05	11.40 ± 0.04

Note: Galaxy ID is the common identifier used in the same order as in Table A3, SFR is the star formation rate, τ_{main} is the e-folding time of the main stellar population model, Stellar Age is the age of the oldest stars in the galaxy, M_{gas} is the gas mass and M_{\star} is the stellar mass.

Table A11. CIGALE-derived parameters for the SB sample. Units as Table A10.

Galaxy ID	f_{AGN}	L_{AGN} $\log(L_{\odot})$	Old Att. $\log(L_{\odot})$	Young Att. $\log(L_{\odot})$	Dust α	L_{dust} $\log(L_{\odot})$
NGC23	0.32 ± 0.06	10.60 ± 0.10	10.73 ± 0.04	10.39 ± 0.06	2.02 ± 0.10	10.92 ± 0.04
NGC253	0.23 ± 0.12	9.96 ± 0.22	10.32 ± 0.04	9.95 ± 0.15	2.38 ± 0.21	10.50 ± 0.07
NGC660	0.43 ± 0.08	10.14 ± 0.09	10.14 ± 0.04	9.59 ± 0.13	2.32 ± 0.25	10.26 ± 0.05
NGC1222	10.35 ± 0.02	10.31 ± 0.02	1.50 ± 0.07	10.66 ± 0.02
NGC1365	0.39 ± 0.12	10.87 ± 0.14	10.83 ± 0.10	10.60 ± 0.16	2.58 ± 0.34	11.06 ± 0.08
IC342	8.39 ± 0.03	7.49 ± 0.24	2.26 ± 0.11	8.45 ± 0.02
NGC1614	11.31 ± 0.04	11.24 ± 0.05	1.37 ± 0.12	11.61 ± 0.04
NGC1797	10.63 ± 0.07	10.68 ± 0.05	1.75 ± 0.09	11.00 ± 0.02
NGC2146	0.38 ± 0.04	10.41 ± 0.06	10.60 ± 0.04	9.09 ± 0.77	2.00 ± 0.10	10.62 ± 0.02
NGC2623	0.27 ± 0.06	10.72 ± 0.11	10.83 ± 0.04	10.78 ± 0.05	1.73 ± 0.09	11.14 ± 0.04
NGC3256	11.30 ± 0.02	11.21 ± 0.02	1.75 ± 0.09	11.59 ± 0.02
NGC3310	0.20 ± 0.07	9.61 ± 0.16	9.63 ± 0.05	10.00 ± 0.04	1.94 ± 0.11	10.20 ± 0.03
NGC3556	0.28 ± 0.09	9.53 ± 0.15	9.71 ± 0.05	9.47 ± 0.09	2.65 ± 0.29	9.93 ± 0.06
NGC3628	0.22 ± 0.03	9.85 ± 0.07	10.34 ± 0.02	9.29 ± 0.06	2.93 ± 0.15	10.39 ± 0.02
NGC4088	9.85 ± 0.03	9.64 ± 0.02	2.01 ± 0.10	10.09 ± 0.02
NGC4194	10.59 ± 0.02	10.50 ± 0.02	1.50 ± 0.07	10.88 ± 0.02
Mrk52	9.87 ± 0.04	9.91 ± 0.03	1.75 ± 0.09	10.23 ± 0.03
NGC4676	10.72 ± 0.02	10.36 ± 0.02	2.00 ± 0.10	10.90 ± 0.02
NGC4818	0.24 ± 0.09	9.53 ± 0.19	9.89 ± 0.05	9.33 ± 0.09	1.82 ± 0.15	10.02 ± 0.05
NGC4945	10.77 ± 0.17	10.60 ± 0.21	2.27 ± 0.11	11.02 ± 0.02
NGC7252	10.60 ± 0.03	10.23 ± 0.04	2.00 ± 0.10	10.78 ± 0.02

Table A11 – *continued* CIGALE-derived parameters for the SB sample. Units as Table A.

Galaxy ID	SFR $\log(M_{\odot}/yr)$	τ_{main} $\log(yr)$	Stellar Age $\log(yr)$	M_{gas} $\log(M_{\odot})$	M_{\star} $\log(M_{\odot})$
NGC23	0.91 ± 0.06	8.96 ± 0.09	9.47 ± 0.06	10.81 ± 0.04	11.23 ± 0.04
NGC253	0.47 ± 0.15	8.92 ± 0.12	9.36 ± 0.06	10.14 ± 0.06	10.57 ± 0.05
NGC660	0.10 ± 0.13	8.97 ± 0.09	9.49 ± 0.09	10.02 ± 0.08	10.44 ± 0.06
NGC1222	0.82 ± 0.02	9.68 ± 0.22	9.08 ± 0.09	9.54 ± 0.07	10.05 ± 0.05
NGC1365	1.14 ± 0.14	8.96 ± 0.11	9.39 ± 0.10	10.82 ± 0.09	11.25 ± 0.07
IC342	-1.99 ± 0.24	8.84 ± 0.15	9.53 ± 0.07	8.49 ± 0.02	8.89 ± 0.02
NGC1614	1.75 ± 0.05	9.60 ± 0.27	8.85 ± 0.12	10.19 ± 0.08	10.74 ± 0.06
NGC1797	1.24 ± 0.10	9.68 ± 0.22	9.12 ± 0.16	9.99 ± 0.12	10.48 ± 0.09
NGC2146	-0.42 ± 0.80	7.97 ± 0.92	8.69 ± 0.35	9.74 ± 0.11	10.30 ± 0.06
NGC2623	1.29 ± 0.05	9.58 ± 0.30	9.00 ± 0.09	9.94 ± 0.06	10.45 ± 0.04
NGC3256	1.72 ± 0.02	9.66 ± 0.24	9.09 ± 0.09	10.47 ± 0.06	10.97 ± 0.05
NGC3310	0.56 ± 0.03	9.67 ± 0.22	8.93 ± 0.10	9.08 ± 0.08	9.61 ± 0.06
NGC3556	0.00 ± 0.08	8.97 ± 0.08	9.47 ± 0.06	9.88 ± 0.05	10.29 ± 0.04
NGC3628	-0.21 ± 0.06	8.70 ± 0.03	9.48 ± 0.02	10.51 ± 0.02	10.91 ± 0.02
NGC4088	0.17 ± 0.02	8.99 ± 0.06	9.35 ± 0.04	9.68 ± 0.04	10.12 ± 0.04
NGC4194	1.01 ± 0.02	9.42 ± 0.39	9.01 ± 0.08	9.73 ± 0.04	10.24 ± 0.03
Mrk52	0.43 ± 0.03	9.59 ± 0.19	9.33 ± 0.06	9.52 ± 0.04	9.97 ± 0.03
NGC4676	0.92 ± 0.02	9.00 ± 0.03	9.50 ± 0.02	10.82 ± 0.02	11.23 ± 0.02
NGC4818	-0.16 ± 0.09	8.79 ± 0.15	9.36 ± 0.09	9.77 ± 0.06	10.20 ± 0.05
NGC4945	1.22 ± 0.25	9.32 ± 0.45	9.23 ± 0.21	10.45 ± 0.13	10.91 ± 0.09
NGC7252	0.76 ± 0.03	8.99 ± 0.05	9.49 ± 0.04	10.66 ± 0.03	11.07 ± 0.02

Table A12. CIGALE-derived parameters for the SIGS sample. Units as Table A10.

Galaxy ID	f_{AGN}	L_{AGN} $\log(L_{\odot})$	Old Att. $\log(L_{\odot})$	Young Att. $\log(L_{\odot})$	Dust α	L_{dust} $\log(L_{\odot})$
NGC275	0.20 ± 0.14	9.26 ± 0.30	9.42 ± 0.09	9.57 ± 0.07	2.09 ± 0.18	9.84 ± 0.07
NGC470	10.22 ± 0.02	10.04 ± 0.03	2.00 ± 0.10	10.47 ± 0.02
NGC474	9.65 ± 0.05	8.94 ± 0.06	2.04 ± 0.10	9.74 ± 0.04
NGC520	0.58 ± 0.08	10.69 ± 0.07	10.45 ± 0.06	9.81 ± 0.16	2.37 ± 0.28	10.56 ± 0.08
IC196	9.66 ± 0.02	8.82 ± 0.02	2.32 ± 0.12	9.73 ± 0.02
NGC833	0.27 ± 0.07	9.09 ± 0.15	9.50 ± 0.02	8.11 ± 0.17	2.87 ± 0.17	9.52 ± 0.02
NGC835	10.60 ± 0.04	10.12 ± 0.07	2.00 ± 0.10	10.74 ± 0.02
NGC838	10.71 ± 0.02	10.48 ± 0.04	1.75 ± 0.09	10.94 ± 0.02
NGC839	10.70 ± 0.02	10.48 ± 0.03	1.50 ± 0.07	10.93 ± 0.02
NGC935	10.54 ± 0.02	10.11 ± 0.03	2.25 ± 0.11	10.70 ± 0.02
IC1801	10.06 ± 0.02	9.77 ± 0.03	2.25 ± 0.11	10.27 ± 0.02
NGC1241	0.21 ± 0.09	10.13 ± 0.18	10.57 ± 0.05	10.09 ± 0.07	2.54 ± 0.27	10.71 ± 0.05
NGC1242	0.41 ± 0.08	9.44 ± 0.09	9.40 ± 0.07	9.09 ± 0.14	2.68 ± 0.23	9.60 ± 0.05
NGC1253	0.21 ± 0.09	9.20 ± 0.18	9.61 ± 0.14	9.19 ± 0.22	2.57 ± 0.27	9.77 ± 0.05
NGC1253A	8.22 ± 0.03	8.58 ± 0.02	1.75 ± 0.09	8.79 ± 0.02
NGC2276	0.20 ± 0.08	10.13 ± 0.18	10.40 ± 0.06	10.38 ± 0.06	2.44 ± 0.24	10.73 ± 0.04
NGC2444	9.05 ± 0.02	8.00 ± 0.09	2.00 ± 0.10	9.10 ± 0.02
NGC2445	10.28 ± 0.05	10.24 ± 0.05	1.97 ± 0.10	10.59 ± 0.02
NGC2633	10.40 ± 0.02	10.32 ± 0.02	1.75 ± 0.09	10.70 ± 0.02
NGC2634	8.64 ± 0.02	7.04 ± 0.36	2.96 ± 0.15	8.65 ± 0.02
NGC2719A	8.65 ± 0.06	9.19 ± 0.02	1.50 ± 0.07	9.35 ± 0.02
NGC2719	0.26 ± 0.11	8.88 ± 0.22	8.80 ± 0.14	9.10 ± 0.05	1.88 ± 0.13	9.32 ± 0.07
NGC2805	9.38 ± 0.04	9.51 ± 0.02	2.47 ± 0.12	9.79 ± 0.02
NGC2814	0.42 ± 0.11	8.86 ± 0.12	8.69 ± 0.08	8.63 ± 0.13	2.54 ± 0.30	8.99 ± 0.08
NGC2820A	7.69 ± 0.02	8.21 ± 0.02	1.69 ± 0.11	8.37 ± 0.02
NGC2820	0.25 ± 0.07	9.24 ± 0.13	9.46 ± 0.04	9.29 ± 0.05	2.47 ± 0.20	9.72 ± 0.04
NGC2964	0.22 ± 0.08	9.57 ± 0.16	9.82 ± 0.06	9.71 ± 0.03	2.23 ± 0.16	10.10 ± 0.04
NGC2970	7.89 ± 0.02	6.86 ± 0.02	1.17 ± 0.18	7.94 ± 0.02
NGC2976	0.29 ± 0.04	8.32 ± 0.06	8.42 ± 0.05	8.31 ± 0.05	2.91 ± 0.15	8.70 ± 0.03
NGC3031	9.46 ± 0.02	8.76 ± 0.02	2.96 ± 0.15	9.55 ± 0.02
NGC3034	0.48 ± 0.03	10.19 ± 0.05	10.20 ± 0.02	8.46 ± 0.02	1.75 ± 0.09	10.21 ± 0.02
NGC3077	0.30 ± 0.07	8.30 ± 0.11	8.45 ± 0.09	8.18 ± 0.11	2.00 ± 0.10	8.66 ± 0.03
NGC3165	7.86 ± 0.09	8.04 ± 0.05	2.01 ± 0.10	8.30 ± 0.02
NGC3166	0.21 ± 0.04	9.06 ± 0.09	9.60 ± 0.02	8.36 ± 0.02	2.56 ± 0.14	9.63 ± 0.02
NGC3169	10.04 ± 0.06	9.38 ± 0.27	2.71 ± 0.19	10.14 ± 0.03
NGC3185	9.12 ± 0.02	8.81 ± 0.02	2.25 ± 0.11	9.32 ± 0.02
NGC3187	0.21 ± 0.05	8.64 ± 0.11	8.91 ± 0.04	8.86 ± 0.02	2.95 ± 0.15	9.22 ± 0.02
NGC3190	9.73 ± 0.02	8.22 ± 0.03	2.50 ± 0.13	9.74 ± 0.02
NGC3226	8.79 ± 0.02	7.49 ± 0.24	2.26 ± 0.11	8.82 ± 0.02
NGC3227	0.20 ± 0.03	9.32 ± 0.08	9.76 ± 0.04	9.30 ± 0.03	2.26 ± 0.11	9.91 ± 0.02
NGC3395	9.52 ± 0.08	9.65 ± 0.07	2.00 ± 0.10	9.93 ± 0.02
NGC3396	9.52 ± 0.04	9.70 ± 0.02	1.75 ± 0.09	9.96 ± 0.02
NGC3424	9.89 ± 0.02	9.62 ± 0.02	2.00 ± 0.10	10.10 ± 0.02
NGC3430	9.61 ± 0.03	9.67 ± 0.02	2.39 ± 0.12	9.98 ± 0.02
NGC3448	0.40 ± 0.05	9.46 ± 0.07	9.20 ± 0.05	9.36 ± 0.04	2.27 ± 0.11	9.63 ± 0.03
IC694	9.02 ± 0.06	7.54 ± 0.03	1.24 ± 0.19	9.03 ± 0.06
NGC3690	11.47 ± 0.02	11.51 ± 0.03	1.25 ± 0.06	11.83 ± 0.02
NGC3786	0.22 ± 0.08	9.39 ± 0.16	9.75 ± 0.05	9.36 ± 0.03	2.22 ± 0.11	9.92 ± 0.04
NGC3788	9.86 ± 0.02	9.45 ± 0.07	2.29 ± 0.11	10.02 ± 0.02
NGC3799	9.27 ± 0.08	9.26 ± 0.08	2.25 ± 0.11	9.60 ± 0.02
NGC3800	10.36 ± 0.03	10.09 ± 0.02	2.23 ± 0.11	10.57 ± 0.02
IC749	8.61 ± 0.05	8.74 ± 0.04	2.25 ± 0.11	9.02 ± 0.02
IC750	0.33 ± 0.07	9.32 ± 0.11	9.52 ± 0.04	8.88 ± 0.04	2.65 ± 0.26	9.62 ± 0.04
NGC4038	10.61 ± 0.04	10.55 ± 0.04	2.00 ± 0.10	10.91 ± 0.02
NGC4394	9.08 ± 0.03	8.26 ± 0.02	2.59 ± 0.21	9.15 ± 0.02

Note: The full table is available in the online version of this paper. A portion is shown here for guidance regarding its form and content.

Table A12 – *continued* CIGALE-derived parameters for the SIGS sample. Units as Table A10.

Galaxy ID	SFR $\log(M_{\odot}/\text{yr})$	τ_{main} $\log(\text{yr})$	Stellar Age $\log(\text{yr})$	M_{gas} $\log(M_{\odot})$	M_{\star} $\log(M_{\odot})$
NGC275	0.11 ± 0.06	9.51 ± 0.25	9.31 ± 0.09	9.22 ± 0.06	9.67 ± 0.05
NGC470	0.57 ± 0.02	9.00 ± 0.02	9.36 ± 0.02	10.09 ± 0.02	10.53 ± 0.02
NGC474	-0.36 ± 0.02	8.70 ± 0.02	9.48 ± 0.02	10.35 ± 0.02	10.76 ± 0.02
NGC520	0.35 ± 0.15	9.00 ± 0.02	9.58 ± 0.05	10.49 ± 0.04	10.89 ± 0.04
IC196	-0.46 ± 0.02	8.70 ± 0.02	9.48 ± 0.02	10.26 ± 0.02	10.67 ± 0.02
NGC833	-1.16 ± 0.17	8.67 ± 0.10	9.61 ± 0.04	10.42 ± 0.04	10.81 ± 0.04
NGC835	0.65 ± 0.07	8.86 ± 0.15	9.40 ± 0.10	10.57 ± 0.05	11.00 ± 0.04
NGC838	0.99 ± 0.04	9.04 ± 0.37	9.18 ± 0.11	10.14 ± 0.05	10.61 ± 0.04
NGC839	0.99 ± 0.03	9.42 ± 0.25	9.31 ± 0.07	10.12 ± 0.03	10.57 ± 0.03
NGC935	0.62 ± 0.03	8.99 ± 0.05	9.49 ± 0.03	10.53 ± 0.02	10.94 ± 0.02
IC1801	0.29 ± 0.03	9.00 ± 0.02	9.36 ± 0.02	9.81 ± 0.02	10.25 ± 0.02
NGC1241	0.62 ± 0.05	8.91 ± 0.13	9.52 ± 0.13	10.78 ± 0.11	11.18 ± 0.09
NGC1242	-0.21 ± 0.08	8.99 ± 0.05	9.49 ± 0.05	9.67 ± 0.05	10.08 ± 0.04
NGC1253	-0.10 ± 0.23	8.88 ± 0.24	9.38 ± 0.21	9.81 ± 0.16	10.24 ± 0.13
NGC1253A	-0.69 ± 0.02	8.94 ± 0.38	9.16 ± 0.19	8.52 ± 0.09	9.00 ± 0.06
NGC2276	0.91 ± 0.05	9.40 ± 0.26	9.32 ± 0.09	10.06 ± 0.06	10.51 ± 0.05
NGC2444	-1.28 ± 0.09	8.70 ± 0.02	9.61 ± 0.03	10.26 ± 0.03	10.65 ± 0.03
NGC2445	0.76 ± 0.04	9.01 ± 0.33	9.20 ± 0.18	9.97 ± 0.10	10.44 ± 0.07
NGC2633	0.84 ± 0.02	9.68 ± 0.16	9.33 ± 0.06	9.88 ± 0.05	10.34 ± 0.04
NGC2634	-2.23 ± 0.36	8.69 ± 0.07	9.69 ± 0.03	9.94 ± 0.04	10.31 ± 0.03
NGC2719A	-0.08 ± 0.02	9.49 ± 0.36	8.79 ± 0.10	8.32 ± 0.05	8.88 ± 0.03
NGC2719	-0.18 ± 0.05	8.86 ± 0.25	9.12 ± 0.09	8.99 ± 0.04	9.47 ± 0.03
NGC2805	0.22 ± 0.02	8.75 ± 0.25	9.08 ± 0.10	9.41 ± 0.04	9.89 ± 0.03
NGC2814	-0.68 ± 0.06	9.03 ± 0.15	9.36 ± 0.05	8.82 ± 0.04	9.25 ± 0.03
NGC2820A	-1.06 ± 0.02	9.33 ± 0.41	9.02 ± 0.10	7.67 ± 0.06	8.18 ± 0.04
NGC2820	-0.16 ± 0.04	9.02 ± 0.12	9.36 ± 0.03	9.35 ± 0.02	9.79 ± 0.02
NGC2964	0.23 ± 0.02	9.00 ± 0.02	9.36 ± 0.02	9.75 ± 0.02	10.18 ± 0.02
NGC2970	-2.41 ± 0.02	8.70 ± 0.02	9.60 ± 0.02	9.09 ± 0.02	9.48 ± 0.02
NGC2976	-1.13 ± 0.04	8.97 ± 0.08	9.48 ± 0.05	8.77 ± 0.03	9.19 ± 0.02
NGC3031	-0.52 ± 0.02	8.70 ± 0.02	9.48 ± 0.02	10.20 ± 0.02	10.61 ± 0.02
NGC3034	-1.06 ± 0.02	7.70 ± 0.02	8.60 ± 0.02	9.30 ± 0.02	9.87 ± 0.02
NGC3077	-1.14 ± 0.12	8.85 ± 0.17	9.40 ± 0.11	8.80 ± 0.07	9.22 ± 0.06
NGC3165	-1.23 ± 0.05	8.99 ± 0.06	9.49 ± 0.05	8.67 ± 0.04	9.09 ± 0.03
NGC3166	-1.08 ± 0.02	8.70 ± 0.02	9.60 ± 0.02	10.42 ± 0.02	10.81 ± 0.02
NGC3169	-0.07 ± 0.22	8.87 ± 0.15	9.55 ± 0.07	10.37 ± 0.02	10.77 ± 0.02
NGC3185	-0.67 ± 0.02	9.00 ± 0.02	9.61 ± 0.02	9.61 ± 0.02	10.01 ± 0.02
NGC3187	-0.42 ± 0.02	8.78 ± 0.31	9.09 ± 0.13	8.77 ± 0.06	9.26 ± 0.04
NGC3190	-1.22 ± 0.02	8.70 ± 0.02	9.60 ± 0.02	10.28 ± 0.02	10.67 ± 0.02
NGC3226	-1.79 ± 0.24	8.63 ± 0.17	9.60 ± 0.05	9.84 ± 0.05	10.23 ± 0.04
NGC3227	-0.17 ± 0.02	9.00 ± 0.03	9.61 ± 0.03	10.10 ± 0.03	10.49 ± 0.03
NGC3395	0.31 ± 0.02	9.55 ± 0.31	9.07 ± 0.09	9.07 ± 0.05	9.57 ± 0.04
NGC3396	0.24 ± 0.02	9.43 ± 0.37	9.05 ± 0.11	8.98 ± 0.06	9.49 ± 0.04
NGC3424	0.13 ± 0.02	9.00 ± 0.02	9.36 ± 0.02	9.65 ± 0.02	10.09 ± 0.02
NGC3430	0.21 ± 0.02	9.00 ± 0.02	9.36 ± 0.02	9.74 ± 0.02	10.17 ± 0.02
NGC3448	-0.08 ± 0.03	8.75 ± 0.24	9.08 ± 0.09	9.10 ± 0.04	9.59 ± 0.03
IC694	-1.96 ± 0.02	7.70 ± 0.02	8.60 ± 0.02	8.40 ± 0.02	8.97 ± 0.02
NGC3690	2.02 ± 0.03	9.12 ± 0.59	8.41 ± 0.17	9.95 ± 0.18	10.59 ± 0.14
NGC3786	-0.10 ± 0.02	8.99 ± 0.03	9.60 ± 0.03	10.17 ± 0.03	10.57 ± 0.03
NGC3788	-0.01 ± 0.07	8.98 ± 0.07	9.58 ± 0.07	10.20 ± 0.08	10.60 ± 0.07
NGC3799	-0.09 ± 0.02	9.00 ± 0.02	9.36 ± 0.02	9.43 ± 0.02	9.87 ± 0.02
NGC3800	0.64 ± 0.02	9.00 ± 0.02	9.36 ± 0.02	10.16 ± 0.02	10.59 ± 0.02
IC749	-0.70 ± 0.03	8.97 ± 0.08	9.33 ± 0.08	8.78 ± 0.08	9.22 ± 0.07
IC750	-0.61 ± 0.05	8.71 ± 0.08	9.32 ± 0.05	9.33 ± 0.04	9.77 ± 0.04
NGC4038	1.08 ± 0.03	9.23 ± 0.24	9.33 ± 0.16	10.34 ± 0.10	10.79 ± 0.07
NGC4394	-1.02 ± 0.02	8.70 ± 0.02	9.48 ± 0.02	9.69 ± 0.02	10.10 ± 0.02

Note: The full table is available in the online version of this paper. A portion is shown here for guidance regarding its form and content.

Table A13. CIGALE-derived parameters for the LSM sample. Units as Table A10.

Galaxy ID	f_{AGN}	L_{AGN} $\log(L_{\odot})$	Old Att. $\log(L_{\odot})$	Young Att. $\log(L_{\odot})$	Dust α	L_{dust} $\log(L_{\odot})$
NGC0078	10.03 ± 0.02	9.27 ± 0.02	2.00 ± 0.10	10.11 ± 0.02
UM246	0.25 ± 0.09	10.36 ± 0.16	10.48 ± 0.09	10.49 ± 0.07	2.20 ± 0.22	10.82 ± 0.07
2MASXJ01221811+0100262	0.42 ± 0.10	11.27 ± 0.12	11.06 ± 0.06	11.05 ± 0.07	1.75 ± 0.09	11.40 ± 0.06
CGCG087-046	0.51 ± 0.06	11.07 ± 0.06	10.86 ± 0.06	10.54 ± 0.08	2.78 ± 0.20	11.06 ± 0.04
UGC04383	0.22 ± 0.04	9.89 ± 0.11	10.09 ± 0.05	10.11 ± 0.04	2.00 ± 0.10	10.44 ± 0.02
2MASXJ08343370+1720462	0.52 ± 0.06	10.55 ± 0.06	10.34 ± 0.06	9.95 ± 0.09	2.29 ± 0.12	10.51 ± 0.05
2MASXJ08381760+3054533	0.22 ± 0.10	10.03 ± 0.20	10.51 ± 0.04	9.64 ± 0.27	2.12 ± 0.13	10.57 ± 0.05
2MASXJ08434495+3549421	0.49 ± 0.10	10.53 ± 0.10	10.34 ± 0.10	9.98 ± 0.05	1.87 ± 0.15	10.52 ± 0.08
UGC05044	0.50 ± 0.09	10.59 ± 0.08	10.40 ± 0.09	10.05 ± 0.06	2.50 ± 0.32	10.59 ± 0.08
ARP142	0.29 ± 0.05	10.41 ± 0.08	10.65 ± 0.04	10.22 ± 0.02	2.82 ± 0.19	10.80 ± 0.03
CGCG266-026	10.81 ± 0.04	10.44 ± 0.08	2.37 ± 0.13	10.99 ± 0.02
LSBCF567-01	7.63 ± 0.02	8.13 ± 0.02	1.75 ± 0.09	8.30 ± 0.02
2MASXJ10225654+3446467	0.54 ± 0.12	10.51 ± 0.11	10.36 ± 0.11	9.53 ± 0.16	2.48 ± 0.31	10.43 ± 0.11
UGC05644	10.57 ± 0.04	10.21 ± 0.02	2.23 ± 0.11	10.75 ± 0.02
CGCG037-076	10.44 ± 0.05	10.68 ± 0.04	1.26 ± 0.08	10.93 ± 0.03
UGCA219	8.19 ± 0.02	8.70 ± 0.02	1.26 ± 0.06	8.87 ± 0.02
NGC3445	0.24 ± 0.05	9.12 ± 0.10	8.94 ± 0.03	9.46 ± 0.02	2.24 ± 0.11	9.62 ± 0.02
2MASXJ10591815+2432343	0.24 ± 0.04	11.27 ± 0.09	11.47 ± 0.02	11.40 ± 0.02	1.75 ± 0.09	11.78 ± 0.02
VV627	10.63 ± 0.04	10.28 ± 0.02	2.25 ± 0.11	10.82 ± 0.02
IC0700	7.98 ± 0.02	8.41 ± 0.02	1.75 ± 0.09	8.60 ± 0.02
UGC06665	10.45 ± 0.04	10.60 ± 0.03	1.50 ± 0.07	10.88 ± 0.02
UGC07388	0.21 ± 0.08	9.78 ± 0.18	10.23 ± 0.05	9.68 ± 0.08	2.37 ± 0.17	10.35 ± 0.04
NGC4320	0.46 ± 0.14	10.20 ± 0.13	10.03 ± 0.13	9.80 ± 0.10	2.73 ± 0.34	10.26 ± 0.11
UGC07936	0.38 ± 0.08	9.94 ± 0.10	9.74 ± 0.11	9.87 ± 0.06	2.75 ± 0.26	10.15 ± 0.06
MRK0237	0.30 ± 0.06	10.38 ± 0.10	10.31 ± 0.04	10.47 ± 0.04	2.00 ± 0.10	10.74 ± 0.03
UGC08327	0.28 ± 0.07	10.67 ± 0.10	10.81 ± 0.05	10.59 ± 0.11	1.77 ± 0.09	11.04 ± 0.04
UGC08335	11.38 ± 0.05	11.41 ± 0.07	1.40 ± 0.12	11.74 ± 0.06
NGC5100	0.28 ± 0.07	10.63 ± 0.11	10.89 ± 0.05	10.40 ± 0.08	2.30 ± 0.12	11.03 ± 0.04
CGCG017-018	10.60 ± 0.02	10.52 ± 0.02	2.00 ± 0.10	10.89 ± 0.02
NGC5331	0.24 ± 0.13	10.97 ± 0.24	11.25 ± 0.08	10.97 ± 0.09	2.13 ± 0.13	11.46 ± 0.08
UGC09618	11.42 ± 0.09	10.95 ± 0.26	2.25 ± 0.11	11.57 ± 0.02
2MASXJ15015015+2332536	0.33 ± 0.08	10.41 ± 0.12	10.54 ± 0.05	10.16 ± 0.11	2.30 ± 0.15	10.72 ± 0.05
SBS1509+583	10.22 ± 0.04	9.77 ± 0.03	2.25 ± 0.11	10.37 ± 0.02
KUG1553+200	10.76 ± 0.03	10.70 ± 0.03	1.75 ± 0.09	11.07 ± 0.02
KUG1556+326	0.26 ± 0.11	10.23 ± 0.21	10.49 ± 0.06	10.14 ± 0.09	2.28 ± 0.13	10.67 ± 0.05
MRK0881	0.32 ± 0.06	10.35 ± 0.09	10.23 ± 0.05	10.40 ± 0.03	2.00 ± 0.10	10.67 ± 0.03
2MASXJ17045097+3449020	11.19 ± 0.02	11.07 ± 0.02	1.75 ± 0.09	11.47 ± 0.02

Table A13 – *continued* CIGALE-derived parameters for the LSM sample. Units as Table A.

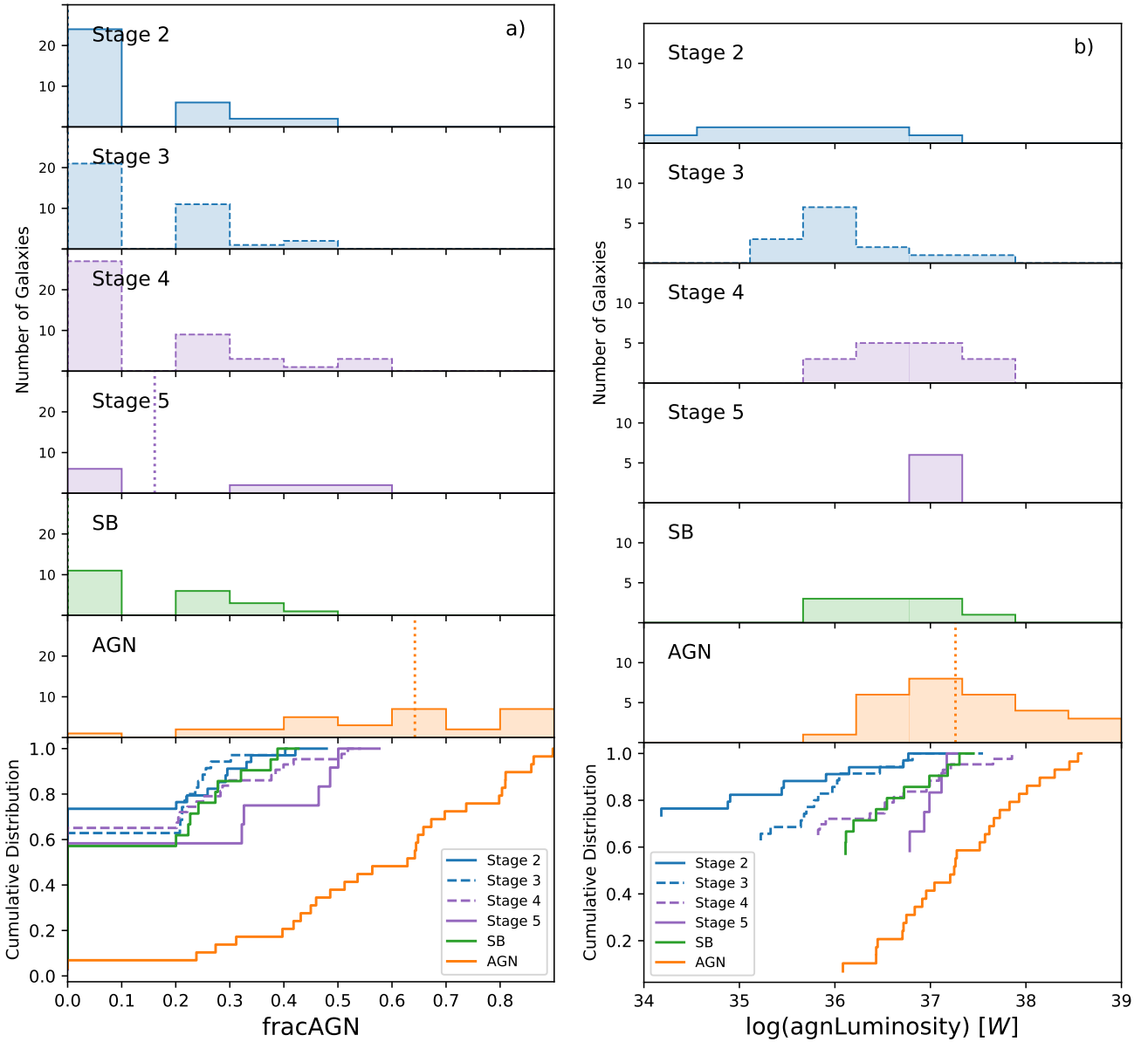
Galaxy ID	SFR $\log(M_{\odot}/yr)$	τ_{main} $\log(yr)$	Stellar Age $\log(yr)$	M_{gas} $\log(M_{\odot})$	M_{\star} $\log(M_{\odot})$
NGC0078	-0.21 ± 0.02	8.70 ± 0.02	9.48 ± 0.02	10.50 ± 0.02	10.91 ± 0.02
UM246	1.03 ± 0.06	9.00 ± 0.20	9.32 ± 0.11	10.47 ± 0.09	10.91 ± 0.08
2MASXJ01221811+0100262	1.58 ± 0.06	9.69 ± 0.21	8.95 ± 0.16	10.12 ± 0.13	10.65 ± 0.10
CGCG087-046	1.07 ± 0.08	8.84 ± 0.15	9.39 ± 0.10	11.00 ± 0.05	11.42 ± 0.04
UGC04383	0.64 ± 0.04	8.70 ± 0.08	9.06 ± 0.04	9.82 ± 0.02	10.31 ± 0.02
2MASXJ08343370+1720462	0.47 ± 0.08	8.91 ± 0.13	9.45 ± 0.09	10.40 ± 0.07	10.82 ± 0.05
2MASXJ08381760+3054533	0.17 ± 0.25	8.77 ± 0.14	9.50 ± 0.05	10.77 ± 0.02	11.17 ± 0.02
2MASXJ08434495+3549421	0.53 ± 0.05	8.92 ± 0.12	9.53 ± 0.12	10.71 ± 0.11	11.11 ± 0.09
UGC05044	0.56 ± 0.05	8.84 ± 0.15	9.45 ± 0.15	10.64 ± 0.12	11.06 ± 0.09
ARP142	0.75 ± 0.02	9.00 ± 0.02	9.61 ± 0.02	11.03 ± 0.02	11.42 ± 0.02
CGCG266-026	0.96 ± 0.07	8.99 ± 0.05	9.47 ± 0.05	10.81 ± 0.07	11.23 ± 0.06
LSBCF567-01	-1.14 ± 0.02	9.64 ± 0.19	9.29 ± 0.06	7.86 ± 0.05	8.32 ± 0.04
2MASXJ10225654+3446467	0.11 ± 0.11	8.70 ± 0.05	9.48 ± 0.02	10.82 ± 0.02	11.23 ± 0.02
UGC05644	0.75 ± 0.02	9.00 ± 0.02	9.61 ± 0.02	11.03 ± 0.02	11.42 ± 0.02
CGCG037-076	1.22 ± 0.03	9.53 ± 0.32	8.57 ± 0.10	9.32 ± 0.09	9.93 ± 0.07
UGCA219	-0.57 ± 0.02	9.10 ± 0.37	8.97 ± 0.07	8.15 ± 0.04	8.66 ± 0.03
NGC3445	0.19 ± 0.02	9.57 ± 0.30	9.14 ± 0.14	9.02 ± 0.10	9.51 ± 0.07
2MASXJ10591815+2432343	1.91 ± 0.02	9.28 ± 0.55	8.72 ± 0.10	10.28 ± 0.04	10.85 ± 0.03
VV627	0.81 ± 0.02	9.00 ± 0.02	9.61 ± 0.02	11.09 ± 0.02	11.49 ± 0.02
IC0700	-0.86 ± 0.02	9.03 ± 0.15	9.20 ± 0.05	8.27 ± 0.02	8.74 ± 0.02
UGC06665	1.13 ± 0.04	9.36 ± 0.44	8.61 ± 0.09	9.35 ± 0.12	9.94 ± 0.10
UGC07388	0.19 ± 0.08	8.81 ± 0.15	9.37 ± 0.09	10.12 ± 0.05	10.54 ± 0.04
NGC4320	0.36 ± 0.08	8.97 ± 0.08	9.57 ± 0.09	10.57 ± 0.07	10.97 ± 0.06
UGC07936	0.60 ± 0.07	9.21 ± 0.23	9.37 ± 0.11	9.97 ± 0.08	10.41 ± 0.07
MRK0237	1.00 ± 0.03	9.64 ± 0.20	9.30 ± 0.07	10.03 ± 0.05	10.49 ± 0.04
UGC08327	1.12 ± 0.10	8.98 ± 0.09	9.36 ± 0.06	10.69 ± 0.06	11.12 ± 0.05
UGC08335	1.92 ± 0.07	9.61 ± 0.29	8.66 ± 0.14	10.11 ± 0.09	10.70 ± 0.07
NGC5100	0.94 ± 0.08	8.89 ± 0.14	9.42 ± 0.09	10.85 ± 0.05	11.28 ± 0.04
CGCG017-018	1.04 ± 0.02	9.00 ± 0.02	9.36 ± 0.02	10.56 ± 0.02	10.99 ± 0.02
NGC5331	1.48 ± 0.09	8.86 ± 0.18	9.21 ± 0.16	10.81 ± 0.11	11.27 ± 0.08
UGC09618	1.45 ± 0.26	8.65 ± 0.43	9.00 ± 0.21	10.75 ± 0.07	11.26 ± 0.04
2MASXJ15015015+2332536	0.70 ± 0.11	8.98 ± 0.07	9.44 ± 0.07	10.48 ± 0.09	10.90 ± 0.08
SBS1509+583	0.29 ± 0.02	9.00 ± 0.02	9.61 ± 0.02	10.57 ± 0.02	10.97 ± 0.02
KUG1553+200	1.23 ± 0.02	9.70 ± 0.21	9.16 ± 0.11	10.06 ± 0.09	10.54 ± 0.07
KUG1556+326	0.66 ± 0.08	8.79 ± 0.15	9.36 ± 0.09	10.60 ± 0.06	11.03 ± 0.04
MRK0881	0.94 ± 0.03	9.63 ± 0.26	9.09 ± 0.10	9.69 ± 0.07	10.19 ± 0.05
2MASXJ17045097+3449020	1.59 ± 0.02	9.65 ± 0.23	9.23 ± 0.10	10.51 ± 0.08	10.99 ± 0.06

Table A14. CIGALE-derived parameters for six AGN galaxies, where a Type 1 AGN ($\psi = 70$) give better χ^2 . Units as Table A10.

Galaxy ID	f_{AGN}	L_{AGN} $\log(L_{\odot})$	Old Att. $\log(L_{\odot})$	Young Att. $\log(L_{\odot})$	Dust α	L_{dust} $\log(L_{\odot})$
Mrk335	0.86 ± 0.04	11.14 ± 0.02	9.88 ± 0.07	8.53 ± 0.90	1.06 ± 0.16	9.90 ± 0.06
Mrk771	0.81 ± 0.04	11.43 ± 0.02	10.18 ± 0.13	9.84 ± 0.23	2.24 ± 0.29	10.37 ± 0.09
2XMMJ141348.3+440014	0.90 ± 0.04	11.96 ± 0.02	10.30 ± 0.18	9.95 ± 0.35	2.33 ± 0.25	10.49 ± 0.04
Mrk1383	0.80 ± 0.04	12.00 ± 0.04	10.52 ± 0.25	10.59 ± 0.20	2.05 ± 0.16	10.89 ± 0.05
ESO141-55	0.74 ± 0.04	11.56 ± 0.02	10.52 ± 0.10	9.55 ± 0.64	2.56 ± 0.21	10.57 ± 0.06
Mrk1513	0.86 ± 0.04	11.87 ± 0.02	10.61 ± 0.11	9.65 ± 0.63	2.13 ± 0.23	10.66 ± 0.07

Table A14 – continued CIGALE-derived parameters for six AGN galaxies, where a Type 1 AGN ($\psi = 70$) give better χ^2 . Units as Table A10.

Galaxy ID	SFR $\log(M_\odot/\text{yr})$	τ_{main} $\log(\text{yr})$	Stellar Age $\log(\text{yr})$	M_{gas} $\log(M_\odot)$	M_\star $\log(M_\odot)$
Mrk335	-0.94 ± 0.91	8.51 ± 0.53	9.58 ± 0.14	10.08 ± 0.17	10.47 ± 0.16
Mrk771	0.51 ± 0.24	8.94 ± 0.22	9.47 ± 0.12	10.47 ± 0.16	10.88 ± 0.14
2XMMJ141348.3+440014	0.56 ± 0.40	9.31 ± 0.52	9.34 ± 0.30	10.27 ± 0.45	10.68 ± 0.41
Mrk1383	1.31 ± 0.21	9.00 ± 0.39	9.24 ± 0.22	10.68 ± 0.19	11.14 ± 0.15
ESO141-55	0.12 ± 0.68	8.60 ± 0.47	9.49 ± 0.21	10.66 ± 0.22	11.06 ± 0.19
Mrk1513	0.18 ± 0.65	8.72 ± 0.67	9.51 ± 0.19	10.68 ± 0.24	11.08 ± 0.22


Figure A5. Histograms (top) for the stages of the SIGS+LSM, AGN and SB samples and the normalized cumulative distributions (bottom) for the AGN fraction (a) and luminosity (b). The colors and lines are identical to Figure 6.

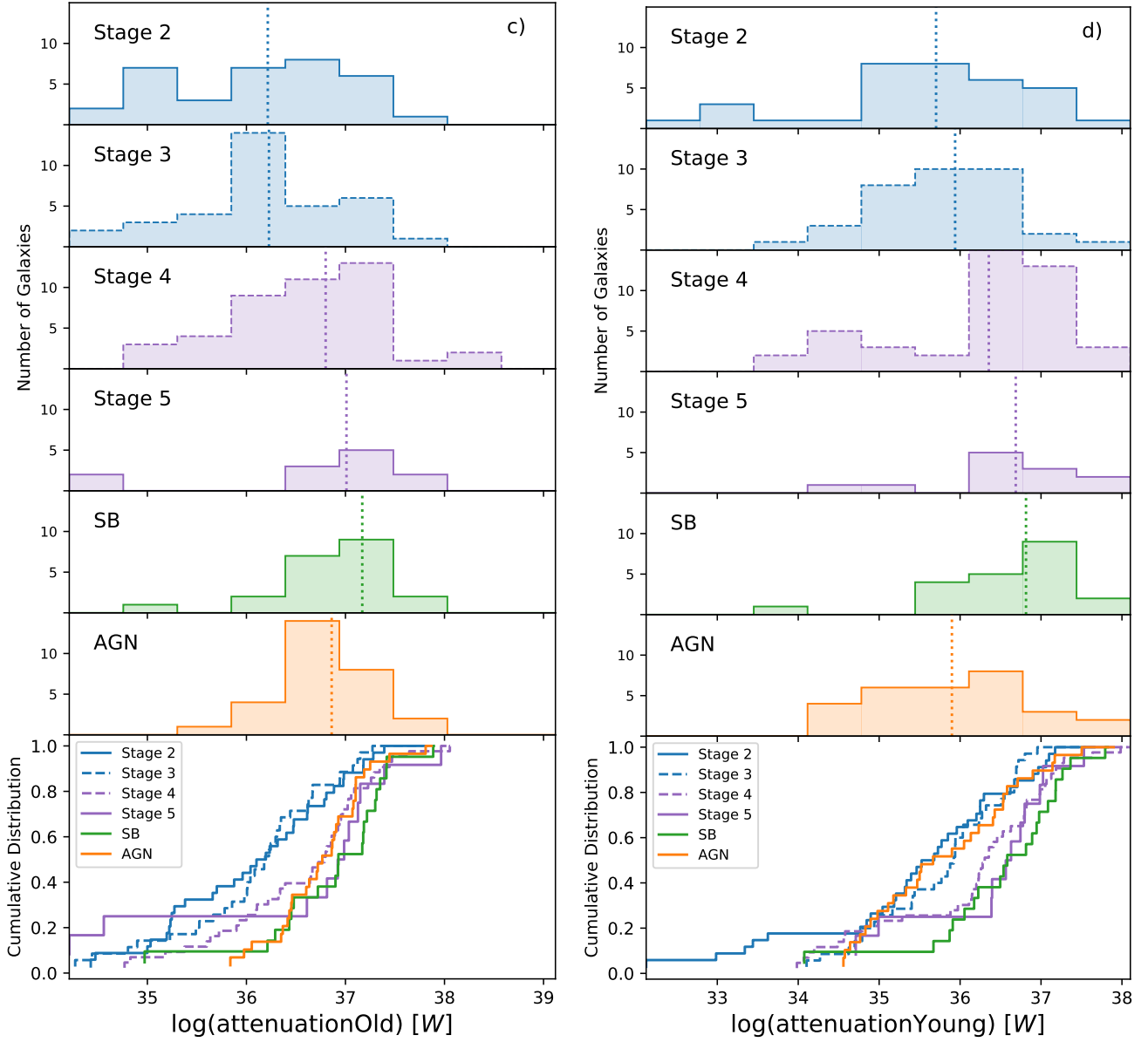


Figure A5 – *continued* Histograms (top) for the stages of the SIGS+LSM, AGN and SB samples and the normalized cumulative distributions (bottom) for the attenuation of old (c) and young stars (d). The colors and lines are identical to Figure 6.

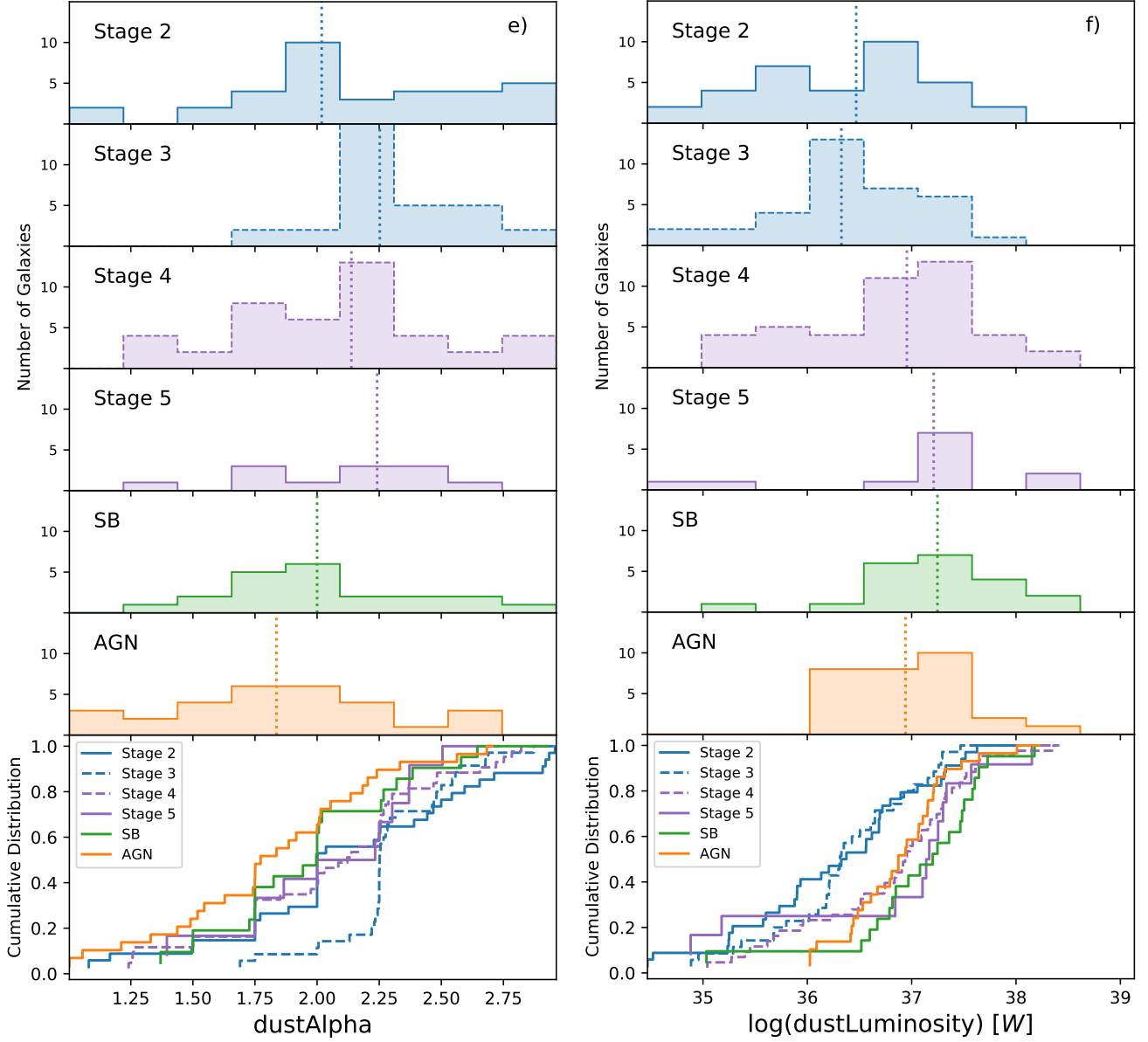


Figure A5 – *continued* Histograms (top) for the stages of the SIGS+LSM, AGN and SB samples and the normalized cumulative distributions (bottom) for the dust parameter α (e) and luminosity (f). The colors and lines are identical to Figure 6.

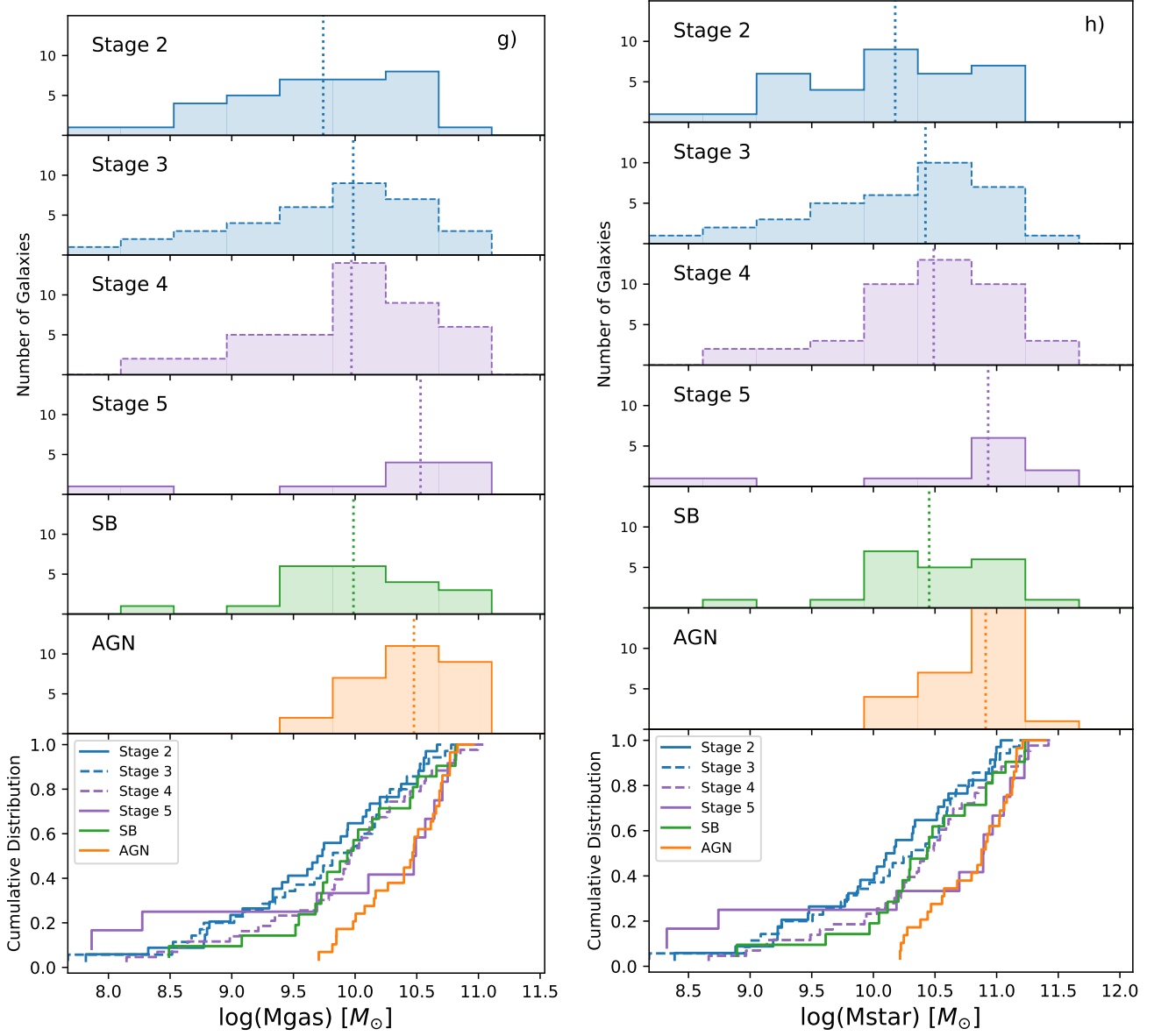


Figure A5 – continued Histograms (top) for the stages of the SIGS+LSM, AGN and SB samples and the normalized cumulative distributions (bottom) for the gas (g) and stellar mass (h). The colors and lines are identical to Figure 6.

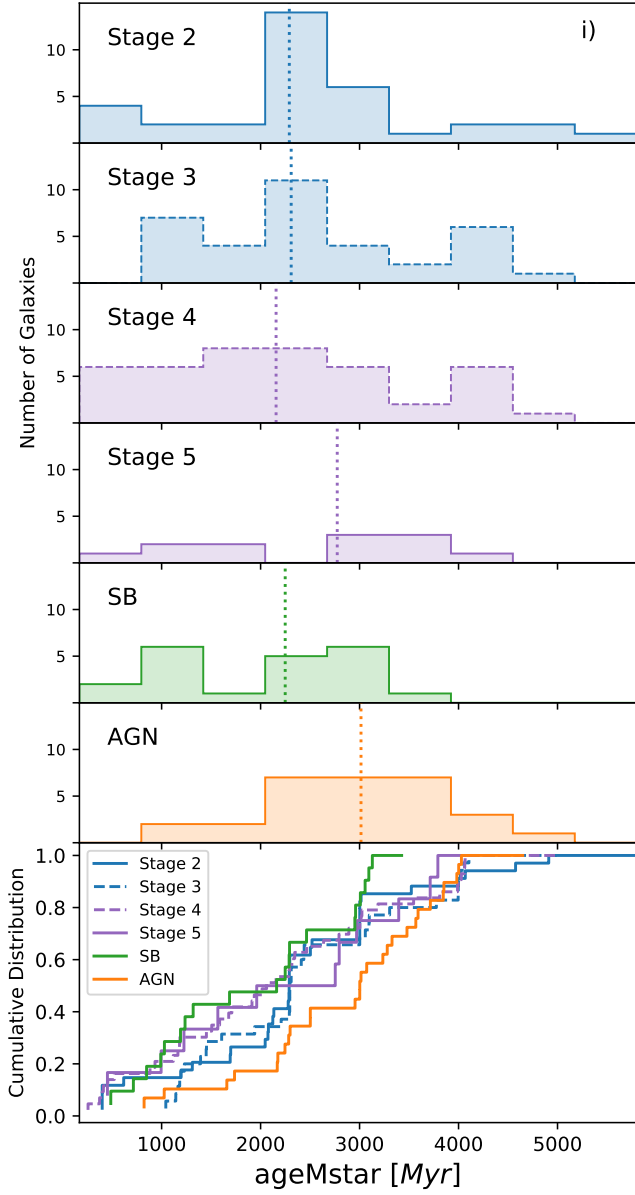


Figure A5 – *continued* Histogram for the stages of the SIGS+LSM, AGN and SB samples and the normalized cumulative distributions (bottom) for weighted age of the stars (i). The colors and lines are identical to Figure 6.